



BRNO UNIVERSITY OF TECHNOLOGY
VYSOKÉ UČENÍ TECHNICKÉ V BRNĚ



FACULTY OF MECHANICAL ENGINEERING
INSTITUTE OF PHYSICAL ENGINEERING

FAKULTA STROJNÍHO INŽENÝRSTVÍ
ÚSTAV FYZIKÁLNÍHO INŽENÝRSTVÍ

VECTORIAL KERR MAGNETOMETRY VEKTOROVÁ KERROVA MAGNETOMETRIE

MASTER'S THESIS
DIPLOMOVÁ PRÁCE

AUTHOR
AUTOR PRÁCE

Bc. LUKÁŠ FLAJŠMAN

SUPERVISOR
VEDOUCÍ PRÁCE

Ing. MICHAL URBÁNEK, Ph.D.

BRNO 2015

Vysoké učení technické v Brně, Fakulta strojního inženýrství

Ústav fyzikálního inženýrství

Akademický rok: 2014/15

ZADÁNÍ DIPLOMOVÉ PRÁCE

student(ka): Bc. Lukáš Flajšman

který/která studuje v **magisterském studijním programu**

obor: **Fyzikální inženýrství a nanotechnologie (3901T043)**

Ředitel ústavu Vám v souladu se zákonem č.111/1998 o vysokých školách a se Studijním a zkušebním řádem VUT v Brně určuje následující téma diplomové práce:

Vektorová Kerrova magnetometrie

v anglickém jazyce:

Vectorial Kerr magnetometry

Stručná charakteristika problematiky úkolu:

S využitím symetrií základních konfigurací využívaných při měření Kerrova jevu navrhnete realizaci měření vektorové magnetometrie.

Navrhnete a sestavte zařízení, které umožní těmto symetriím efektivně využívat a umožní z magneto-optických měření získat všechny tři složky magnetizace.

Cíle diplomové práce:

Proveďte rešeršní studii řešení interakce elektromagnetické vlny s magneto-opticky aktivním prostředím.

Kvalitativně ukažte způsob, kterým lze z magneto-optického měření získat všechny tři složky magnetizace.

Sestavte aparaturu na měření mikro- a nanostruktur pomocí vektorové Kerrovy magnetometrie. Proveďte měření nanostruktur s obecně definovaným směrem vektoru magnetizace.

Seznam odborné literatury:

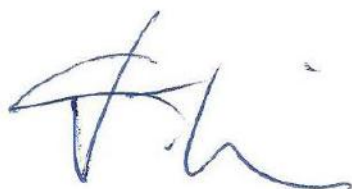
[1] VIŠŇOVSKÝ, Š.: Optics in Magnetic Multilayers and Nanostructures (Optical Science and Engineering). CRC Press 2006. ISBN 0849336864.

[2] DING, H.F., et al.: Experimental method for separating longitudinal and polar Kerr signals. Journal of Magnetism and Magnetic Materials, 212, 2000, ISSN 0304-8853.

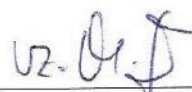
Vedoucí diplomové práce: Ing. Michal Urbánek, Ph.D.

Termín odevzdání diplomové práce je stanoven časovým plánem akademického roku 2014/15.

V Brně, dne 21.11.2014



prof. RNDr. Tomáš Šíkola, CSc.
Ředitel ústavu



doc. Ing. Jaroslav Katolický, Ph.D.
Děkan

Abstrakt

Moderní magnetické materiály a na nich postavená zařízení se v poslední době stávají značně komplexními s vysokými nároky jak na výrobu, tak na charakterizaci jejich vlastností. Z malého výčtu jevů, které jsou schopny charakterizace takových struktur, v práci využíváme tu, jež nese název magneto-optický Kerrův jev. V teoretické části řešíme odezvu elektromagnetické vlny při odrazu od rozhraní materiálu s nenulovou magnetizací. Dále se zabýváme návrhem a konstrukcí zařízení, které je schopno tuto odezvu detekovat. V experimentální části je funkčnost zařízení prokázána na různých magnetických systémech: metastabilních vrstvách železa, pro případ Stonerovy–Wohlfarthovy částice a v neposlední řadě na magnetických vortexech. Navržený rastrovací vektorový Kerrův magnetometer nám umožnil charakterizovat magnetické vzorky s rozlišením 500 nm.

Abstract

Increased complexity of novel magnetic materials in the last decade has placed high demands on the manufacturing process as well as on the characterization. One of the possibilities for characterization of magnetic samples is to exploit the magneto-optical effects. The presented work uses the magneto-optical Kerr effect as a major characterization technique to probe the magnetic properties of samples. We have developed a mathematical model describing the effect of the magnetization on the polarized light and present an apparatus capable of measuring the response given by the light-matter interaction. The experimental results show the performance of the apparatus on the various magnetic systems including meta-stable iron layers, Stoner-Wohlfarth particles and magnetic vortices. The scanning vectorial Kerr magnetometer allowed us to probe the vector of magnetization with diffraction limited resolution below 500 nm.

Klíčová slova

vektorová magnetometrie, Kerrův jev, MOKE, elektromagnetické vlny, magnetické vortexy.

Keywords

vectorial magnetometry, Kerr effect, MOKE, electromagnetic waves, magnetic vortices.

FLAJŠMAN, L. *Vectorial Kerr magnetometry*. Brno: Vysoké učení technické v Brně, Fakulta strojního inženýrství, 2015. 99 s. Vedoucí diplomové práce – Ing. Michal Urbánek, Ph.D.

PROHLÁŠENÍ:

Prohlašuji, že jsem diplomovou práci vypracoval samostatně pod odborným vedením Ing. Michala Urbánka, Ph.D., a že veškeré podklady, ze kterých jsem čerpal, jsou uvedeny v seznamu použité literatury.

Bc. Lukáš Flajšman

ACKNOWLEDGMENT

The list of persons whom I would like to express my gratitude would be impossible to fit on one page dedicated to the acknowledgment. Concerning this work my deeper thanks goes to **Dr. Michal Urbánek**. Due to his outstanding diligence and skillful guidance, he has always found a way to make things possible. I also address this acknowledgement to **Marek Vaňatka**. He has always been around to assist with almost anything. He was also the one to prepare almost all the samples for testing MIRANDA vector Kerr magnetometer. In case of **Igor(PRO)Turčan** I have always appreciated his humor and the way he lifted the spirit in our office. I also thank him for coming up with the implementation of the laser attenuation system to the camera. My gratitude and my sorry also goes to **Viola Křížáková** who has helped me with the sample characterization and that I have sometimes hold her off while always redesigning the whole apparatus. For the proofreading of the text and for accompanying me at my Erasmus stay I would like to thank the Canadian duo: **Cassandra Timmenga** and **Anna-Kay Russell**. Both have shown the patience while correcting the same things repeatedly. Another person who has taught me how to wind-surf and also has improved the quality of the text is **prof. Jiří Spousta**. Finally, I thank **Jana** and **my family** because they have always been supporting me and I also thank them for the understanding they have always shown.

Děkuji.

Bc. Lukáš Flajšman

Part of the work was carried out with the support of Nanofabrication and Nanocharacterization Core Facility of CEITEC – Central European Institute of Technology under CEITEC – open access project, ID number LM2011020, funded by the Ministry of Education, Youth and Sports of the Czech Republic under the activity “Projects of major infrastructures for research, development and innovations”.

CONTENTS

1. <i>Introduction</i>	3
2. <i>Introduction to magneto-optical effects</i>	5
2.1 Application of the magneto-optical Kerr effect	6
2.1.1 MOKE magnetometry	6
2.1.2 MOKE microscopy	7
2.2 Light polarization states in complex notation	9
2.2.1 Monochromatic waves - spatial and time dependence	9
2.2.2 Light polarization - elliptical polarization	10
2.3 Polarizing optical systems - Jones formalism	13
2.3.1 Magneto-optical observables	16
3. <i>Maxwell-equations - Electromagnetic waves in magnetized matter</i>	20
3.1 Permittivity tensor	20
3.1.1 Some conventions connected with the permittivity tensor	24
3.2 Electro-magnetic waves in magnetized matter	25
3.2.1 4×4 matrix formalism	29
3.2.2 Ultra-thin film limit	36
3.2.3 Summary of the theoretical section	36
4. <i>Vectorial Kerr magnetometry</i>	38
4.1 Apparatus for scanning magneto-optical Kerr microscopy	39
4.1.1 Magneto-optical setup - differential intensity detection	39
4.2 Scanning Kerr magnetometer design	42
4.2.1 Mechanical design	45
4.2.2 Scanning Magneto-Optical Kerr modes of operation	51
5. <i>Experimental results and discussion</i>	54
5.1 Analytic samples - Apparatus verification	54
5.1.1 Laser spot and stability of the setup	54
5.2 Sample characterization	56
5.2.1 Scanning-optical microscope	57
5.2.2 Vectorial Kerr magnetometry	58
5.2.3 Scanning vectorial Kerr microscope	67
5.2.4 Scanning vectorial Kerr magnetometer	74

5.2.5	Coercive field mapping mode - CFM	79
5.3	Experimental results - summary	81
6.	<i>Conclusion - Contribution of the thesis</i>	83
	<i>List of abbreviations</i>	96
	<i>Appendix</i>	97
	Appendix A - Permittivity tensor $\vec{\epsilon}_r$	97
	Appendix B - On the Rotation and the Ellipticity	97
	Appendix C - Heating induced nucleation	99

1. INTRODUCTION

Observing, studying and exploiting magnetism has been initiated by observing strange behavior of so called lodestone - (rock rich in Fe_3O_4). Its ability to attract and control remotely only some materials while completely ignoring other ones was puzzling, yet too attractive to be left intact. By shaping the magnetite, or thermomagnetizing iron needles, first compass was invented. In history, applications of magnetism have always been surpassing its theoretical understanding and despite the effort and attention magnetism has received during 20th century, much is left to be solved [1–3].

Nowadays applications of magnetism are found in daily life. The recording industry has for long used the thin-film magnetism for achieving higher data densities. In the last decade, magnetism has initiated a development of novel devices such as MRAMs (Magnetic Random Access Memories). MRAMs are, from the basic concept, designed to be non-volatile and to have a low access time surpassing in many aspects the RAM memories we all have in our computers. Another possible extension to the MRAM memory may be the vortex MRAM with four possible magnetic states in a single memory cell. It highly rises the recording bit density while retaining high speed. The development of such complex structures demands accurate characterization techniques which help to understand the complex processes present in the magnetic structures above the Stoner criterion [1].

The magnetization response in complex magnetic structures to an external magnetic field is often accompanied by non-trivial magnetization processes, where the means to directly probe the magnetization are scarce. It often requires large scale instruments (X-ray magnetic circular dichroism) or the amount of information we gain from the measurement is highly limited (vibrating sample magnetometry). Another technique probing the magnetization is the magneto-optical Kerr effect. Contrary to the X-ray magnetic circular dichroism the Kerr effect does not require large scale facility while as well as X-ray magnetic circular dichroism it directly probes the magnetization with more or less same physical principle. When we compare the magneto-optical Kerr effect to the Vibrating Sample Magnetometry (VSM) the difference is directly evident - with the magneto-optical Kerr effect we can perform time-resolved measurements with high spatial resolution, whereas the VSM probes the mean magnetization in a highly quantitative manner. The goal of this thesis is to use the advantages of the magneto-optical Kerr effect and probe the vector of magnetization with a table-top device.

In Chapter 2, we present a short introduction with special aim for the magneto-optical Kerr effect. The light-polarization states are defined and the explanation how

to use them to probe magnetic behavior is provided.

In Chapter 3, we use the macroscopic field theory to find how the magnetization can influence the reflected light. Rigorous mathematical background is presented to support and justify the experimental findings. In Chapter 4, we show how the magneto-optical Kerr effect can be used to probe individual components of the magnetization vector. We present the experimental setup of the scanning vectorial Kerr magnetometer and we point out the most crucial parts allowing us to probe the vector of magnetization. The experimental results obtained with the designed apparatus are presented in Chapter 5. In the experimental part we try to show the universality and the sensitivity of the magneto-optical Kerr effect to the vector of magnetization. In the text we present various modes of operation of the apparatus with examples of obtained results. We start by analyzing the structures with the magnetization arrangement that can be solved analytically. The major part of the experimental chapter is dedicated to magnetic vortices, where we focus on spatial distribution of the vector of magnetization. We study the magnetization vector field evolution in the external magnetic field. The results on the $8\ \mu\text{m}$ disk have shown a new magnetization structure, experimentally not resolved in the literature yet. The last study presented in the experimental section is concerned with a novel material for the Focused Ion Beam (FIB) direct writing.

2. INTRODUCTION TO MAGNETO-OPTICAL EFFECTS

The presented thesis is throughout all the chapters closely interconnected with the magneto-optical effects from the theoretical as well as from the practical point of view. This chapter serves as an introduction for the reader in the means of theoretical description, quantification and measurement of the magneto-optical effects with the aim for the magneto-optical Kerr effect.

Following the historical development, the first person believed to have observed the magneto-optical effect is Michael Faraday (1791-1867). He discovered in 1845 that the light propagating through a glass rod placed in the magnetic field of an air coil has its polarization plane rotated with respect to the original direction. Faraday, as the brilliant experimentalist he was subsequently able to quantify the measured effect to the form nowadays known as Faradays law [4]. He found out, that the polarization plane rotation is given by a simple formula $\Theta_F = B\nu d$ ¹, where B is a magnitude of an axial magnetic field, ν is known as Verdet constant and d is a length of a glass rod [5]. Other researchers continued to search for the effect of a magnetic field on the light propagation. The effect most relevant to this thesis was discovered in 1877 by reverend John Kerr (1824-1907) [6, 7]. Similarly to Faraday he was able to observe polarization modulation, but contrary to his predecessor, he observed polarization changes after a reflection of the polarized ray from the polished pole of a magnet. After his discovery, he was followed by many others (e.g. [8, 9]). At the beginning it was thought, that relatively weak Kerr effect would not be of much use [10], but as the experimental equipment developed the magneto-optical Kerr effect (MOKE) has become one of the most precise and widely used techniques [11]. It has been shown that the sensitivity of MOKE can compete with best state-of-art SQUID magnetometers, with the sensitivity lower than one single atomic layer of ferromagnetic material [12]. Another superior capability of MOKE is its speed which permits the possibility for time-resolved measurements of magnetization evolution. Time resolution in the femtosecond scale has been shown [13–19]. MOKE can also be depth sensitive [20]. It can provide relatively good lateral resolution down to 0.2 μm [10, 21, 22]. Recently, a novel exotic high-resolution magneto-optical device working on the principle of SNOM (*Scanning near-field optical microscope*) has been presented achieving a resolution below diffraction limit down to 100 nm [23, 24]. From the economical point of view MOKE is one of the cheapest techniques to implement that can probe the magnetization. It also offers the ability to probe samples on large distances or in extreme conditions (UHV, heated

¹ More correct formula would be $\Theta_F = \int_0^d B(x)\nu(x)dx$.

samples, cooled samples, ...). When the ultimate resolution is not the interest we can state that whenever there is a need for a truly *in-situ* observation, MOKE is the right tool.

2.1 Application of the magneto-optical Kerr effect

Since its discovery, magneto-optical Kerr effect has been utilized to many sample characterizing techniques. The following section presents the two most spread applications: magneto-optical magnetometry and magneto-optical microscopy. Examples of magneto-optical measurements obtained by these two forms of Kerr effect measurements will be shown.

2.1.1 MOKE magnetometry

MOKE magnetometry is a widely used technique providing us with the possibility to probe the magnetic state of a sample only by light-matter interaction. For moderate light intensities, MOKE magnetometry is a non-destructive technique that does not require any special sample preparation or experimental conditions. Due to its compactness and relative simplicity MOKE magnetometry has been in the last decade widely used to study magnetic thin films. The first scientists to experimentally prove its value for ultrathin magnetic layers were Moog and Bader in the 1990s [25, 26]. Since then the MOKE magnetometry has been used as a major characterization technique for magnetometry of ultrathin magnetic layers [27]. It has been mentioned previously that MOKE magnetometers can have high a spatial- [10] as well as a time-resolution [13]. In theory, the MOKE technique has the capability to probe the vectorial nature of magnetization². Kerr magnetometers can measure the magnetization cycles in an external magnetic field as shown in Fig. 2.1. Such a device consists only from a light source, 2 polarizers³ and light intensity detector (photodiode) [28].

When the spatial distribution of magnetization is needed, the Kerr magnetometer can be redesigned by adding a focusing lens and a scanning stage or the laser beam scanning system. Such a device can measure 2D maps of the magnetization and thus is called the Scanning Kerr magnetometer (SKEM) (often called the Scanning Kerr microscope). Among the designs of the Scanning Kerr microscopes two main trends are present. They differ in a way the spatial distribution of magnetization is measured. Either the sample is scanned under the laser spot or the sample is fixed and the laser beam is scanned on the sample surface. Since the Kerr effect is strongly dependent on the angle of incidence the scanning with a sample is favorable [13, 14, 21, 29–32]. In contrary to the scanning with a laser beam scanning with a sample provides space invariant imaging where the angle of incidence is constant in the entire field of view.

² We will focus on the vectorial Kerr magnetometry in more detail in chapter 4 since the vectorial Kerr magnetometry is the main goal of this master's thesis.

³ Or even without any polarizer when measuring transversal magnetization.

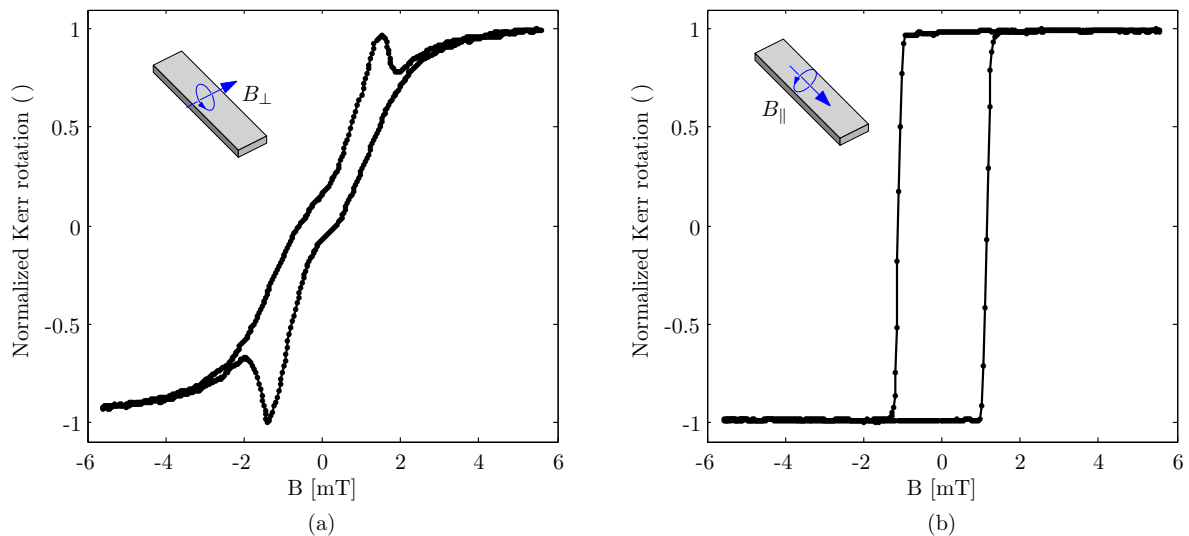


Fig. 2.1: (a) and (b) are hysteresis loops for a rectangular sample with 20 nm of Co (Si substrate). Shaping a sample to the form of a bar will introduce strong so called shape anisotropy [27] created by a strong demagnetizing field in such a sample. This anisotropy will force the magnetization vector to lie (in zero external field) along the longer dimension and when the external field is applied, magnetization will be forced to tilt to the direction of the external magnetic field. Measurements (a) and (b) were performed by rotating the sample while the position of the laser beam and the magnetic field was fixed. When the field was perpendicular to the anisotropy axis we measured a loop as in figure (a). When the field was along the anisotropy axis the loop took a form as in (b). The loop (b) is to be expected as it is typical *easy axis* loop. But loop in (a) with spikes at ≈ 1.36 mT was puzzling. Later we will show that spikes are connected with a nucleation of domains and that in-plane components of magnetization are not the only ones in play (As would be expected in thin sample with only 20 nm of magnetic material.)

On the other hand scanning with a sample can not compete with the imaging rate of galvano-scanning systems with imaging rates in the 100Hz range [33].

Despite the great sensitivity SKEMs tend to be rather complex instruments with high demands on time and operation. When there is a need for a picture of a domain pattern only and the need for quantitative information is not the primary objective full-field magneto-optical Kerr microscopes are favorable. We will briefly present the MOKE microscopy in the next section.

2.1.2 MOKE microscopy

Ever since the magnetic domain patterns were discovered, researchers have been looking for a way to reveal these patterns. The first technique that helped to discover magnetic domains, was presented by Francis Bitter in 1931. He used what we now call Bitter colloids (ferromagnetic microparticles) to reveal the stray field of a polished ferromagnet. He used a classical microscope to observe such patterns [34]. In 1932 he experimented with the external magnetic field to show that, even with low magnetic field, one can completely change the structure of a Bitter pattern [35]. Although the

Bitter technique stimulated the interest in magnetic ordering, the technique itself is slow and really difficult to perform.

It was known that the Kerr effect could, in theory, reveal magnetic patterns too, but such small changes in amplitude (induced by a variation in polarization) were impossible to be observed by the naked eye. MOKE microscopy had to wait for the dawn of digital cameras and digital data processing [36]. One of the pioneers closely involved in magneto-optical Kerr microscopy is Rudolf Schäfer. His work on the observation and characterization of magnetic domains is summarized in the book he co-authored - Magnetic domains [10] and in chapter from the Handbook of magnetism and advanced magnetic materials - Investigation of Domains and Dynamics of Domain Walls by the Magneto-optical Kerr effect [37]. Kerr microscopy works on a simple principle depicted in Fig. 2.2. Polarized light reflected from the sample will be perturbed in the presence of magnetization. Polarization changes can be easily converted with an analyzer to intensity amplitude changes captured e.g. by a digital camera. By the proper relative adjustment of a polarizer/analyzer (Fig. 2.2 (b)) one can get a magneto-optical contrast. As a result, domains with opposite magnetization will have a different brightness. If the hysteresis field cycle is of the interest it is possible to measure the average

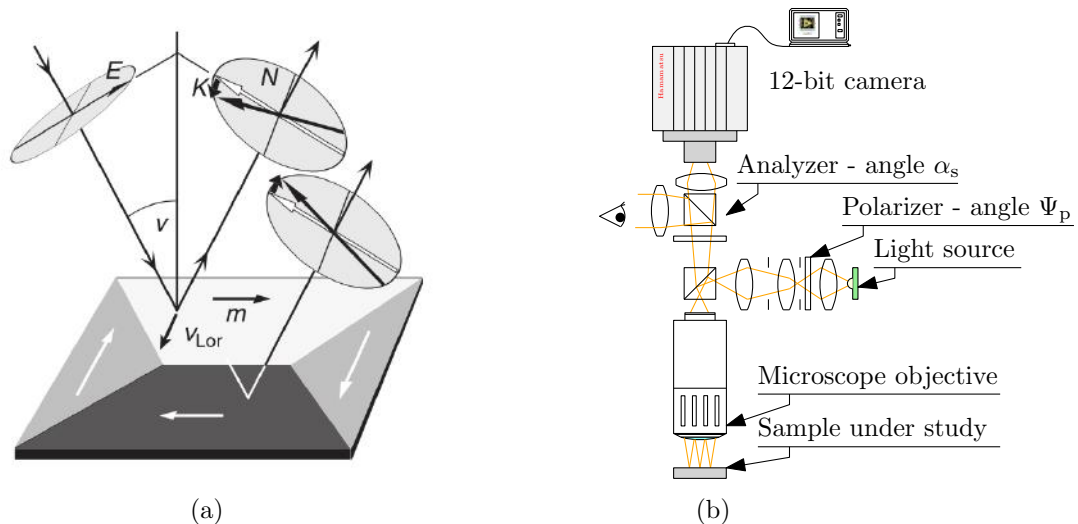


Fig. 2.2: (a) Basic illustration of magneto-optical interaction for in-plane magnetization. (Taken from [10].) (b) Simplified scheme of the magneto-optical Kerr microscope for observing out-of-plane (OOP) magnetization.

grey level of the obtained pictures as a function of the external magnetic field. Such a measurement acquired on the 0.8 nm thin Co layer is in Fig. 2.3. Depending on the relative angle of the polarizer/analyzer ($\Psi_p > \alpha_s$, $\Psi_p < \alpha_s$) domain with a magnetization pointing up will be brighter/darker than domain with the magnetization pointing down. Kerr microscopy is a valuable tool for the characterization of magnetic layers revealing many interesting phenomenons. For example, it has been used to study the switching of magnetic domains under the influence of an external electric field [38, 39], characterizing samples with divergence in the coercive field [40] or it has been combined with magneto-resistive measurements as in [41]. MOKE microscopy has also been used

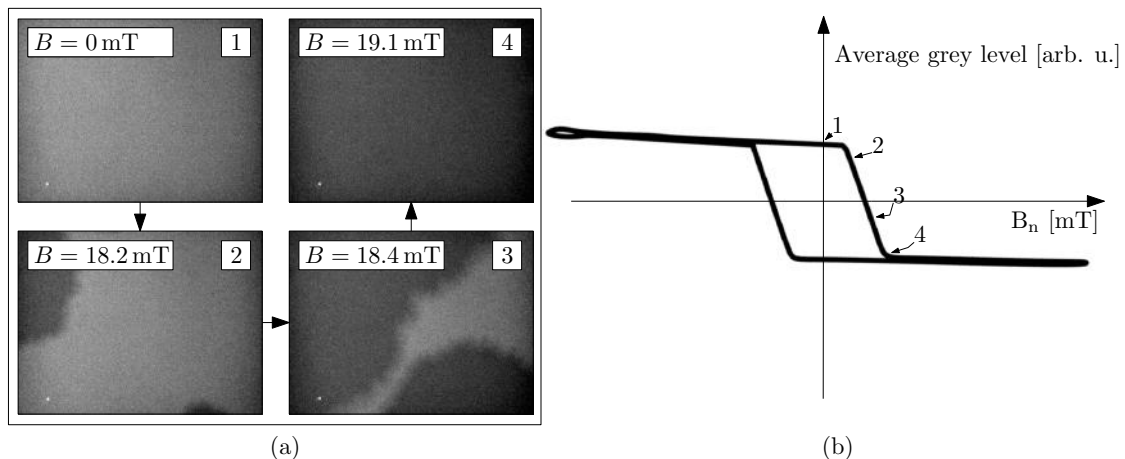


Fig. 2.3: (a) Pictures obtained by the Kerr microscope at the institute Néel, CNRS, France. With a varying magnetic field the cobalt layer is forced to change its magnetization state by switching to the opposite direction. Insets show magnitude of the external magnetic field and the numbers in the upper right corners serve to interconnect measured pictures with the sketch of the measured hysteresis loop in (b). The square-like loop indicates strong out-of-plane anisotropy and also that the magnetization switching is not given by the nucleation of domains but rather by the domain wall propagation process. Pictures on the left are taken for only 0.8 nm of cobalt. Such a sensitivity is possible thanks to a modern analog camera with 12-bit resolution and also the real-time data processing. Full movie of the switching is in the supplementary material `../Movies/CoPerp.avi`.

in a pump-probe technique experiment with a gate-triggered camera or pulsed laser. For a sample with a non-stochastic switching process, nanosecond dynamics can be recorded [42, 43].

2.2 Light polarization states in complex notation

The previous text demonstrated how the magneto-optical Kerr effect is used to probe the magnetic state of a sample without any mention about the origin of this effect. This introductory section will cover some fundamental theoretical aspects one must know when dealing with the theoretical description of the magneto-optical effects. We start with light polarization states and with the mathematical apparatus allowing us to elegantly describe light polarization and its transformations. In the end of this section we show how the effect of a sample is modeled within the presented matrix framework.

2.2.1 Monochromatic waves - spatial and time dependence

The electromagnetic wave (EM wave) is a fundamental consequence of Maxwell's equations. In the presented text we do not rigorously derive the wave equation for the non-magnetic media, since it can be easily found in many textbooks dealing with the classical electrodynamics, e.g. [44, p. 23] or [45, p. 440]. In order to characterize the electromagnetic wave we use two vectors. The electric field \mathbf{E} and the vector of

magnetic induction \mathbf{B} . These two vectors are uniquely interconnected so it is possible to relate \mathbf{E} to \mathbf{B} (and *vice-versa*) by the simple relation derived from Maxwell's equations. This relation can be found for example in Introduction to electrodynamics [46, p. 375, Eq. 9.46].

Since the two vectors describing the electromagnetic field are not unique, we will restrict ourselves to the description of the electric part of the electromagnetic wave. A good model which accurately describes light and its polarization is in the form of monochromatic plane waves. These waves have both spatial and time dependence. The time dependence is given by a frequency ω and the spatial dependence is given by the vector $\mathbf{k}(\omega)$ pointing in the direction of the wave propagation. This vector is complex in general, but in a non-dispersive medium only the real part is non-zero. The mathematical description for time dependence (given by t) and spatial dependence is given by:

$$E_j(\mathbf{r}, t) = E_{j,\max} e^{-i(\omega t - \mathbf{k} \cdot \mathbf{r})}; \quad j = \{x, y, z\}, \quad (2.1)$$

where $E_{j,\max}$ is a complex amplitude and \mathbf{r} is a position vector. The real part represents maximum amplitude of the electric field wave component ($E_x(\mathbf{r}, t)$, $E_y(\mathbf{r}, t)$, $E_z(\mathbf{r}, t)$) and the imaginary part represents a phase retardation of a particular wave component. Real fields are obtained by taking real part of Eq. (2.1) denoted by \Re . Real electric field component might be described, e.g., as

$$E_j(\mathbf{r}, t) = \Re \left(E_{j,\max} e^{-i(\omega t + \mathbf{k} \cdot \mathbf{r})} \right) = \|E_{j,\max}\| \cos(-\omega t + \mathbf{k} \cdot \mathbf{r} + \delta_j); \quad j = \{x, y, z\}, \quad (2.2)$$

with δ_j describing the phase retardation. We will continue to use the complex notation for the sake of simplicity. Another convention known as '*time notation*' will be used throughout this work. This convention defines the sign used before $i\omega$. Before we move further, it is good to note that the vectors \mathbf{D} and \mathbf{H} are named electric displacement and magnetic field, respectively. In general, the relation between all four vectors \mathbf{E} , \mathbf{D} , \mathbf{B} , \mathbf{H} is not trivial, and for the magneto-optically relevant case the description will be given in Chapter 3.

2.2.2 Light polarization - elliptical polarization

When the mathematical description in the form of a monochromatic plane wave is inserted into Maxwell's equations we find that the electromagnetic wave is a transverse wave with a direction of propagation given by \mathbf{k} (for non-absorbing medium) and also that for isotropic medium vectors \mathbf{E} , \mathbf{B} , \mathbf{k} form a right handed coordinate system [44, 46, 47]. This orthogonality gives a rise to light eigenmodes - polarization states. Any electromagnetic wave can be described as a superposition of these states. Arbitrary wave propagating in the direction of \mathbf{k} can be expressed in the s and p basis by the following relation

$$\mathbf{E}(\mathbf{r}, t) = A_s \mathbf{e}_s + A_p \mathbf{e}_p, \quad (2.3)$$

with A_s , A_p being modal amplitudes of s, p waves and \mathbf{e}_s , \mathbf{e}_p are called as modal vectors. Both modal vectors form an orthogonal basis ($\hat{\mathbf{e}}_s \cdot \hat{\mathbf{e}}_p = 0$). In free space the

lack of an absolute coordinate system gives rise to another definition - the p wave has its polarization in the horizontal plane, while the s wave is polarized in the vertical plane. When the sample is in play, the definition of s and p waves is strictly given by the plane of the incidence. The wave given by the s polarization has its electric field vector oscillating perpendicular to the plane of incidence, and p polarization has its electric field vector oscillating parallel to the plane of incidence. Figure 2.4 depicts the definition given in the previous text. The Cartesian coordinate system with orthogonal unit vectors \hat{e}_s , \hat{e}_p is not the only way how to fully describe the polarization state of any light wave. Another orthogonal coordinate system has its unit vectors in the form of left- and right-handed circular polarization (RCP & LCP). The Coordinate system in the form of circular polarizations can be particularly useful in describing circular dichroism [48, 49].

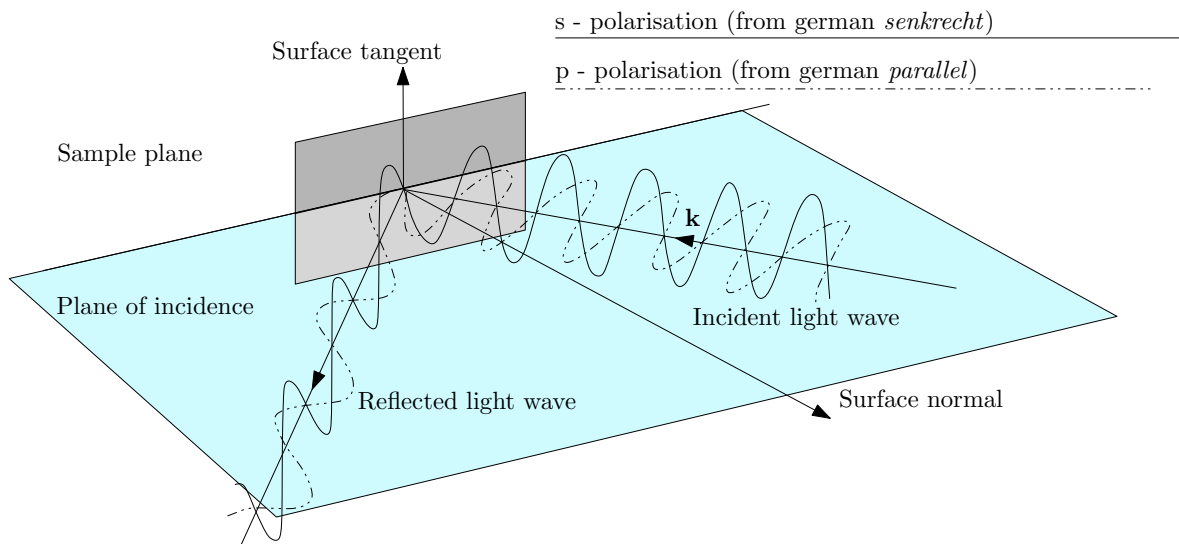


Fig. 2.4: Sketch of a monochromatic plane wave being reflected from a sample. Plane of incidence is given by the sample surface normal and by the \mathbf{k} vector of the incident light. Two cases are distinguished - s polarization with electric field oscillating normal to the plane of incidence and p polarization with a wave having its electric field component oscillating parallel to the plane of incidence.

Figure 2.4 shows the reflection from a sample that is non-absorbing and isotropic. The resulting wave after reflection retains its polarization state and only the amplitude is modulated (according to the Fresnel formulas). In general, this simplification does not apply and with the incident linear polarization, the polarization after reflection is elliptical.

Figure 2.5 shows how (with the help of equation 2.3), the elliptical polarization can be described as a superposition of two linearly polarized waves. The resulting elliptical polarization can be characterized with four parameters (Fig. 2.5 (d)). To fully describe the elliptical polarization, only two parameters are needed [50], hence it is possible to, find the relation between all the ellipsometric observables⁴. The first one denoted as

⁴ When the description is not unique all the parameters has to be interconnected.

θ is called azimuth. It is an oriented angle from the direction of the s polarization. Quantity ϵ is obtained as a ratio between the minor and major axis of the ellipse. ϵ is called ellipticity and is given by $\tan \epsilon = b/a$. The last two parameters are Θ and $\delta_{s,p}$ denoting the ratio of the maximal values of s and p polarized waves (modal amplitudes A_s, A_p) given by $\tan \Theta = A_s/A_p$ and the relative phase difference of s and p waves respectively. Observables $\theta, \epsilon, \Theta, \delta_{s,p}$ are interconnected by the following relations [48].

$$\tan \Theta e^{i\delta_{s,p}} = \frac{A_s}{A_p} e^{i\delta_{s,p}} = \frac{\tan \theta - i \tan \epsilon}{1 + i \tan \theta \tan \epsilon}, \quad (2.4)$$

$$\tan 2\theta = \tan 2\Theta \cos \delta, \quad (2.5)$$

$$\sin 2\epsilon = \sin 2\Theta \sin \delta. \quad (2.6)$$

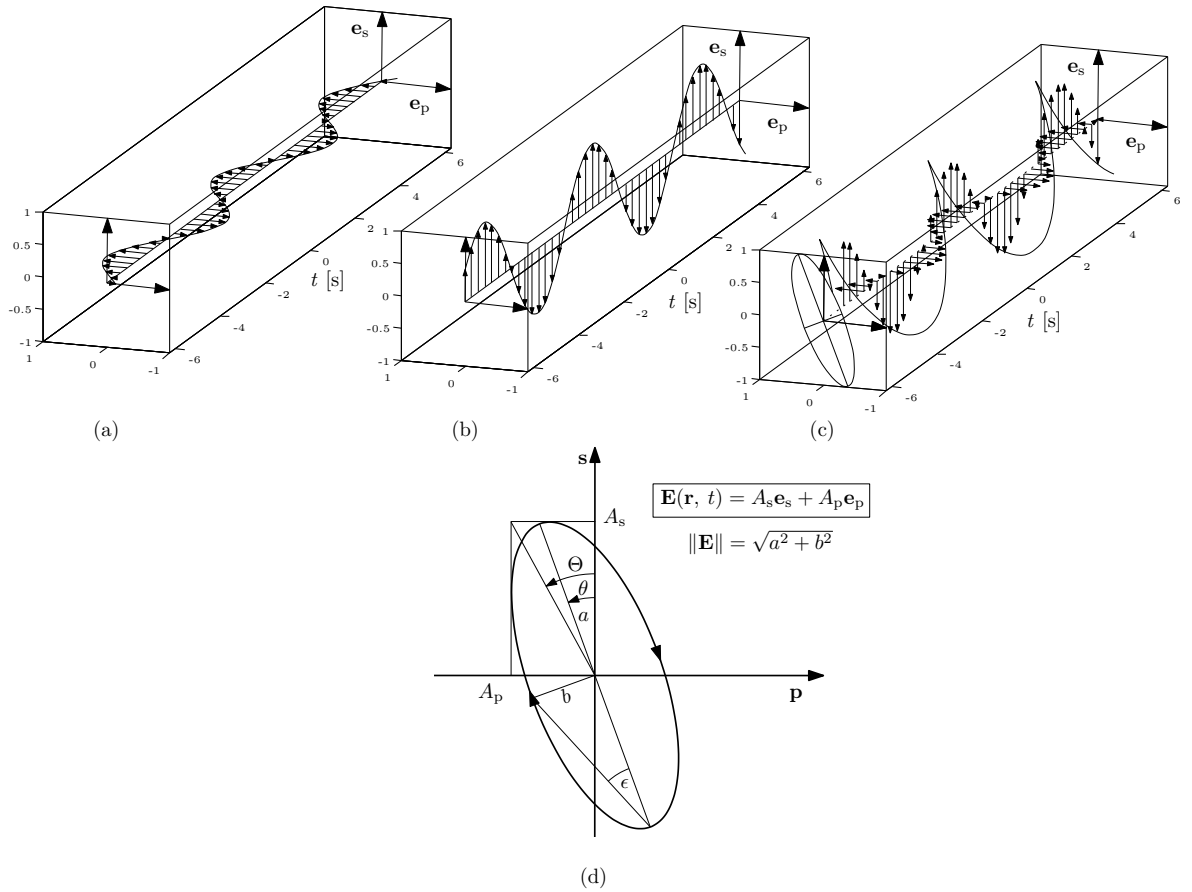


Fig. 2.5: (a)/(b) Time development of p/s polarized beam at $z = 0$ expressed as $\mathbf{E}_p = 0.5 \cos(\omega t)/\mathbf{E}_s = 1 \cos(\omega t + \frac{\pi}{4})$. The resulting wave (c) will have elliptical polarization with $\theta = -0.38$ rad and $\epsilon = 0.3$ rad. (d) shows the projection of the elliptical polarization to the s-p plane. Quantities a and b are the major and minor axes of the ellipse. The rotation of the major axis is given by the rotation parameter θ and the ϵ is called ellipticity. Figure (d) further serves for the sake of deriving relations Eq. (2.5-2.6).

2.3 Polarizing optical systems - Jones formalism

In the previous section the elliptical polarization was introduced. Knowing the theoretical effect of the sample on the light polarization state is valuable, but the measured signal will also reflect the used apparatus. To properly distinguish between the effect of a sample and the effect of the instrumentation, modeling of the signal is necessary. We need to describe the effect of our instrumentation on the polarization state of the sample. The equation (2.2) is sufficient for a proper description of the polarization state and by solving Maxwell's equations for every optical element it is, in theory, possible to trace the polarization variation and finally get only the effect of the sample. But this approach is too cumbersome to provide direct insight to the measuring process.

In this work, we use matrix formalism originally presented by C. Jones in 1941 [51]. His idea, to describe polarization state by generally complex column vector (called Jones vector) and to describe the effect of an optical element by the two-by-two matrix, proved its value in ellipsometry [50] as well as in magneto-optics [48].

In the first step we define a Jones vector of the s- and p-polarized light exploiting the equation Eq. (2.1) -

$$\mathbf{J} = \begin{bmatrix} E_x \\ E_y \end{bmatrix} = e^{-i\omega t} \begin{bmatrix} E_{x,\max} e^{i\delta_x} \\ E_{y,\max} e^{i\delta_y} \end{bmatrix}, \quad (2.7)$$

where the $\mathbf{k} \cdot \mathbf{r}$ has been omitted since there is no spatial variation during the measurement. This equation is equivalent to the equation Eq. (2.3). The only difference is that we defined two orthogonal modal vectors in the form of column vectors. It follows from the electrodynamics of the monochromatic plane wave (or Gaussian beam), that the measured light intensity is given by the time averaged Poynting vector [46, 47], mathematically expressed as $I = \frac{\varepsilon_0 c}{2} |E|^2$. This relation written in the Jones formalism given by Eq. (2.7) will be

$$I = \frac{\varepsilon_0 c}{2} \mathbf{J}^\dagger \cdot \mathbf{J}, \quad (2.8)$$

where \dagger means Hermitian adjoint (complex conjugate) of the vector. Often we are only interested in the polarization state of the light. This can be uniquely described by the normalized form of the equation (2.7). Normalization is done by dividing the Jones vector by its intensity using Eq. (2.8). To simplify our calculations we shall omit the $e^{-i\omega t}$ part since Eq. (2.8) has already been derived with $e^{-i\omega t}$ in mind. The normalized Jones vector might be written as

$$\mathbf{J} = \begin{bmatrix} \cos \Theta \\ \sin \Theta e^{i\delta_{s,p}} \end{bmatrix}, \quad (2.9)$$

where $\delta_{s,p} = \delta_s - \delta_p$ stands for the mutual s- and p-wave phase difference. Purely s- and p-polarized beams will have its Jones vectors given by

$$\mathbf{e}_s = \begin{bmatrix} 1 \\ 0 \end{bmatrix}, \quad \mathbf{e}_p = \begin{bmatrix} 0 \\ 1 \end{bmatrix}. \quad (2.10)$$

It is easy to see, that the condition of orthogonality is satisfied so $\mathbf{e}_s^\dagger \mathbf{e}_p = \mathbf{e}_p^\dagger \mathbf{e}_s = 0$. Unity vectors describing right-handed circular polarization (RCP \odot) and left-handed circular polarization (LCP \ominus) are given by:

$$\mathbf{e}_{\odot} = \frac{1}{\sqrt{2}} \begin{bmatrix} 1 \\ i \end{bmatrix}, \quad \mathbf{e}_{\ominus} = \frac{1}{\sqrt{2}} \begin{bmatrix} 1 \\ -i \end{bmatrix}. \quad (2.11)$$

Conversion from the s and p basis to the circular basis is done via the following transition matrix [48]

$$F_{s,p \rightarrow \odot, \ominus} = \frac{1}{\sqrt{2}} \begin{bmatrix} 1 & 1 \\ -i & i \end{bmatrix}. \quad (2.12)$$

The inverse of the transition matrix gives the conversion from the circular modes to the linear modes. Circular polarization is useful for the theoretical description of the MO effects (Section 3.2) while the s and p basis is used when describing the effect of the sample on the incident polarization (Section 4.1.1).

In order to model the effect of various optical elements on the Jones vector \mathbf{J} we can express the relation between the final Jones vector \mathbf{J}_f and the initial Jones vector \mathbf{J}_i by the two-by-two matrix multiplication

$$\mathbf{J}_f = \hat{\mathbf{J}} \mathbf{J}_i. \quad (2.13)$$

The equation (2.13) is easily extended to n optical elements

$$\mathbf{J}_f = \hat{\mathbf{J}}_n \dots \hat{\mathbf{J}}_3 \hat{\mathbf{J}}_2 \hat{\mathbf{J}}_1 \mathbf{J}_i. \quad (2.14)$$

When tracing the polarization in the apparatus, one has to know the Jones matrices $\hat{\mathbf{J}}$ representing the individual optical elements. Following the classical study texts [49, p. 35] and [52, p. 378] a short summary of optical elements, together with their representing Jones matrices, that are relevant to this thesis, is presented in table 2.1.

To demonstrate the ease of use of the Jones formalism we carry out few basic calculations with selected optical elements from table 2.1. In 2.6 a light beam described by the Jones vector \mathbf{J}_i is being transformed by the optical elements fully described by their Jones matrices (e.g. $\hat{\mathbf{J}}_{\text{QWP}}$). The quantity that is measured is the intensity I on the photo-detector.

From the previous text it is apparent, that by using the Jones formalism for the description of the optical-setup problem with polarization-varying elements is an easy task. However final expressions for the intensity obtained by Eq. (2.8) tend to be rather complex expressions that are difficult to carry out by hand. An analytical software can be used for simplifying the task of obtaining measured intensity as a function of many variables. In our case we used mathematical software Maple 18 available at the BUT.

The Jones formalism, despite its universality, does not cover the depolarization effect. When the depolarization effects are present in the optical setup, Stokes vector formalism should be used [53, 54].

Tab. 2.1: The summary of basic optical elements affecting the polarization state of the light wave. Arbitrary rotation of an optical element can be achieved by applying the proper rotation of coordinate system given by $\hat{\mathbf{J}}_{\text{rot}}$. In the last row the Wollaston prism is shown. It acts as a polarizing beam-splitter separating two orthogonal polarizations. Matrix representation of the prism is given only for the Wollaston prism rotated by $\pi/4$.

	Name of an element	Jones matrix notation	Matrix representation
	Vertical Polarizer	$\hat{\mathbf{J}}_{\text{VP}}$	$\begin{bmatrix} 1 & 0 \\ 0 & 0 \end{bmatrix}$
	Rotation of coordinate system	$\hat{\mathbf{J}}_{\text{rot}}(\alpha)$	$\begin{bmatrix} \cos \alpha & \sin \alpha \\ -\sin \alpha & \cos \alpha \end{bmatrix}$
	General polarizer	$\hat{\mathbf{J}}_{\text{rot}}(-\alpha)\hat{\mathbf{J}}_{\text{VP}}\hat{\mathbf{J}}_{\text{rot}}(\alpha)$	$\begin{bmatrix} \cos^2 \alpha & \cos \alpha \sin \alpha \\ \cos \alpha \sin \alpha & \sin^2 \alpha \end{bmatrix}$
	Quarter-Wave plate (fast axis vertical)	$\hat{\mathbf{J}}_{\text{QWP}}$	$e^{i\frac{\pi}{4}} \begin{bmatrix} 1 & 0 \\ 0 & i \end{bmatrix}$
	Half-Wave plate (fast axis either vertical or horizontal)	$\hat{\mathbf{J}}_{\text{HWP}}$	$\begin{bmatrix} 1 & 0 \\ 0 & -1 \end{bmatrix}$
	Wollaston prism (rotated by $\frac{\pi}{4}$)	$\hat{\mathbf{J}}_{\text{WP}}$	$\begin{bmatrix} 1 & \pm 1 \\ \pm 1 & 1 \end{bmatrix}$

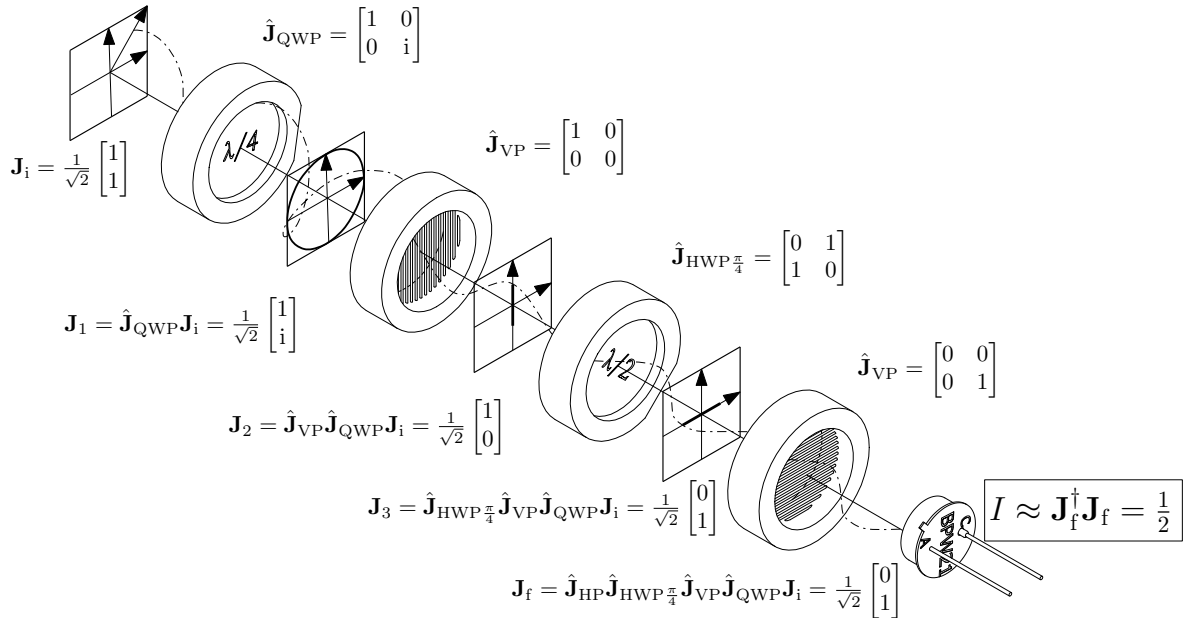


Fig. 2.6: Initially linearly polarized beam \mathbf{J}_i (oriented at $\pi/4$) when passed through the quarter wave plate is transformed to the left-handed circular polarization (\mathbf{J}_1). Vertical polarizer will pass only the vertical component of the electric field (\mathbf{J}_2) which is subsequently transformed to the horizontal polarization (\mathbf{J}_3) by half-wave-plate oriented at angle $\pi/4$ thus the final polarizer has no effect at all (\mathbf{J}_4). Because of the "time averaging" caused by the slowness of the detection we see only the effective value of the intensity $I \approx \mathbf{J}_f^\dagger \cdot \mathbf{J}$.

2.3.1 Magneto-optical observables

This part describes how magneto-optical Kerr effect in different geometries can be easily expressed by the means of the Jones formalism presented in the previous section.

In the Cartesian coordinate system, the effect of the sample can be expressed as a two-by-two matrix of the complex Fresnel reflection/transmission amplitudes (r_{ij}, t_{ij} where $i, j \in \{s, p\}$). Jones matrices for the reflection $\hat{\mathbf{J}}_R^C$ and transmission $\hat{\mathbf{J}}_T^C$ are expressed by⁵ [55]

$$\hat{\mathbf{J}}_R^C = \begin{bmatrix} r_{ss} & r_{sp} \\ r_{ps} & r_{pp} \end{bmatrix}, \quad (2.15)$$

$$\hat{\mathbf{J}}_T^C = \begin{bmatrix} t_{ss} & t_{sp} \\ t_{ps} & t_{pp} \end{bmatrix}. \quad (2.16)$$

Note that the matrices Eq. (2.15) and Eq. (2.16) provide full description of the polarizing effect of a sample. In case of an optically isotropic sample, matrices $\hat{\mathbf{J}}_R^C$ and $\hat{\mathbf{J}}_T^C$ are diagonal, which means there is no interaction between s and p waves. When the medium is magnetized, the optical anisotropy arises and the off-diagonal components become generally non-zero [28, 48, 55]. The selection of the order of the s and p notation in the subscript of the Fresnel reflection (and transmission) amplitudes can be clearly seen from the following equation

$$\mathbf{J}_f = \begin{bmatrix} r_{ss} & r_{sp} \\ r_{ps} & r_{pp} \end{bmatrix} \begin{bmatrix} 1 \\ 0 \end{bmatrix} = \begin{bmatrix} r_{ss} \\ r_{ps} \end{bmatrix}. \quad (2.17)$$

We see that when the matrix $\hat{\mathbf{J}}_R^C$ is multiplied by the vector representing s polarization we get a beam with a non-zero p component. Here the subscript ps means, that the p-polarized component originates in the s-polarized wave.

When measuring magneto-optical Kerr effect, three basic geometries are historically distinguished [10]. These configurations differ in a relative orientation of the plane of incidence (defined by light propagation vector \mathbf{k}) and the magnetization \mathbf{M} (giving a rise to the off-diagonal elements). All the three configurations are depicted in Fig. 2.7. We use some basic symmetries given implicitly in these three configurations in order to restrain the possible values of the matrix elements in $\hat{\mathbf{J}}_R^C$. In the simplest case, we assume so called normal incidence Polar Kerr effect (Figure 2.7 (a) for $\varphi = 0$). For this configuration s and p polarizations has to be undistinguishable thus the form of a Jones matrix of the sample $\hat{\mathbf{J}}_R^C$ has to be invariant in any rotation of the coordinate system around z . With the help of the matrix for rotating the coordinate system $\hat{\mathbf{J}}_{\text{rot}}(\alpha)$ (Tab. 2.1) matrix equation representing mentioned symmetry arguments can be written

$$\hat{\mathbf{J}}_{\text{rot}}(\alpha) \hat{\mathbf{J}}_R^C \hat{\mathbf{J}}_{\text{rot}}(\alpha) = \hat{\mathbf{J}}_R^C. \quad (2.18)$$

Note, that both signs of α are positive. This is a result of the fact, that after reflection coordinate axes are mirrored, thus $\hat{\mathbf{J}}_{\text{rot}}(\alpha) \rightarrow \hat{\mathbf{J}}_{\text{rot}}^{-1}(\alpha) = \hat{\mathbf{J}}_{\text{rot}}(-\alpha)$. From the determinant

⁵ Superscript C stands for Cartesian. Jones matrix of a sample can be easily expressed in other orthogonal coordinate systems as well.

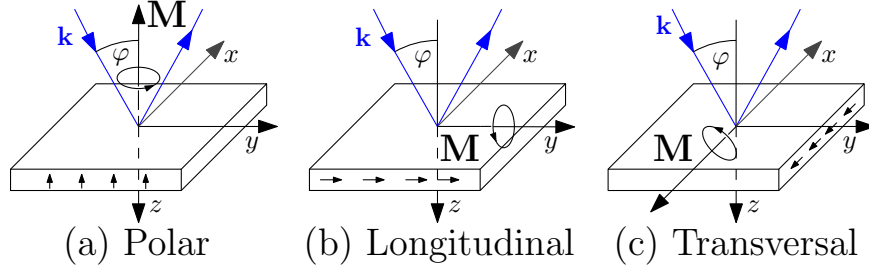


Fig. 2.7: Three basic configurations of MOKE for the angle of incidence φ . In (a) the polar Kerr effect is shown. Vector \mathbf{M} is orthogonal to the sample surface and at the same time \mathbf{M} lies in the plane of incidence. For the longitudinal Kerr effect (b) \mathbf{M} lies in the surface plane and at the same time is lies in the plane of incidence. In the last case (c) the transversal Kerr effect is shown. Here \mathbf{M} lies in the surface plane and is orthogonal to the plane of incidence. The magnetization direction is given by the current loop around the corresponding axis.

of Eq. (2.18) we see, that the system is under-determined, resulting expressions will be parametric in selected variable. A solution is obtained by taking the matrix element [1, 1] and isolating r_{ss}

$$r_{ss} = -\frac{\cos(\theta) r_{sp} - \cos(\theta) r_{ps} + \sin(\theta) r_{pp}}{\sin(\theta)}. \quad (2.19)$$

This expression, when substituted to the equation in the element [1, 2] reads

$$r_{sp} = \cos^2(\theta) r_{ps} + \sin^2(\theta) r_{ps} = r_{ps}, \quad (2.20)$$

with the help of Eq. (2.19) and Eq. (2.20) we can summarize the mutual relations of elements of the Jones matrix to the form

$$r_{ss} = r_{pp}, \quad (2.21)$$

$$r_{pp} = -r_{ss}. \quad (2.22)$$

To study the effect of reversing the magnetization \mathbf{M} on the sample matrix $\hat{\mathbf{J}}_R^C$ we perform a mirror operation by xz plane⁶ described by the matrix [48]

$$\mathbf{J}_{\text{rot}}^{xz} = \begin{bmatrix} 1 & 0 \\ 0 & -1 \end{bmatrix}. \quad (2.23)$$

This mirror operation describes the reversal of the vector \mathbf{M} . Magnetization is in the group of axial vectors, thus can be modeled as a current loop perpendicular to the direction of \mathbf{M} [1]. By changing the sense of a current generating \mathbf{M} , or changing the direction of a passage of the time, the vector \mathbf{M} changes sign [55, 56]. When the matrix $\hat{\mathbf{J}}_R^C$ is mirrored back and forth by the xz axis we obtain

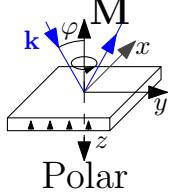
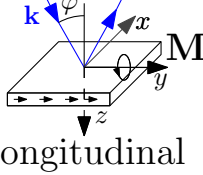
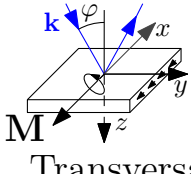
$$(\mathbf{J}_{\text{rot}}^{xz})^{-1} \hat{\mathbf{J}}_R^C \mathbf{J}_{\text{rot}}^{xz} = \begin{bmatrix} r_{ss} & -r_{sp} \\ -r_{ps} & r_{pp} \end{bmatrix}. \quad (2.24)$$

⁶ In this operation x component is left intact while y component changes its sign.

The result shows that the diagonal components are an even function of \mathbf{M} while off-diagonal components are odd in \mathbf{M} .

Analogous analysis as for the Polar Kerr at normal incidence can be performed for other cases of magneto-optical Kerr configurations mentioned in Fig. 2.7. Table 2.2 summarizes the results obtained by exploiting individual symmetries given in all three Kerr effects.

Tab. 2.2: Summary of Jones matrices relevant to all three MOKE configurations. For the normal incidence ($\varphi = 0$) s and p polarizations are indistinguishable and we see that no *in-plane* component of magnetization affects off-diagonal elements. In the general case of $\varphi \neq 0$ and p polarization longitudinal/transversal Kerr effect cause: polarization changes/intensity modulation. The superscript c denotes the constant part in external field. For a purely s polarized beam, there is no effect of transversal magnetization to the signal. Reproduced from [57].

	$\varphi = 0$	$\varphi \neq 0$	
 <p>Polar</p>	$\begin{bmatrix} r_{ss} & r_{ps} \\ r_{ps} & -r_{ss} \end{bmatrix}$	$\begin{bmatrix} r_{ss} & r_{ps} \\ r_{ps} & r_{pp} \end{bmatrix}$	r_{ss}, r_{pp} : independent on M_z even in φ $r_{sp} = r_{ps}$: odd in M_z even in φ
 <p>Longitudinal</p>	$\begin{bmatrix} r_{ss} & 0 \\ 0 & -r_{ss} \end{bmatrix}$	$\begin{bmatrix} r_{ss} & -r_{ps} \\ r_{ps} & r_{pp} \end{bmatrix}$	r_{ss}, r_{pp} : independent on M_y even in φ $r_{sp} = -r_{ps}$: odd in M_y odd in φ
 <p>Transversal</p>	$\begin{bmatrix} r_{ss} & 0 \\ 0 & -r_{ss} \end{bmatrix}$	$\begin{bmatrix} r_{ss} & 0 \\ 0 & r_{pp}^c + r_{pp} \end{bmatrix}$	r_{ss}, r_{pp}^c : independent on M_x even in φ r_{pp} : odd in M_x odd in φ

Now we make a use of the matrix of a sample and we define the magneto-optical observables: quantities that are physically measured in the magneto-optical measurements. We have defined how \mathbf{M} induces off-diagonal elements in Jones matrix of a sample Eq. (2.15). In the next step (Eq. (2.17)) we showed, how off-diagonal elements contribute to inter-mode mixing between s and p waves. In section 3 we show, that off-diagonal elements are at least three orders of magnitude lower than diagonal ones ($r_{ps}/r_{ss} \ll 1$, $r_{sp}/r_{pp} \ll 1$).

Let us rewrite the effect of a sample on s and p polarized beam and divide the

resulting Jones vector by the a corresponding diagonal component

$$\mathbf{J}_{f,s} = \begin{bmatrix} r_{ss} & r_{sp} \\ r_{ps} & r_{pp} \end{bmatrix} \begin{bmatrix} 1 \\ 0 \end{bmatrix} = r_{ss} \begin{bmatrix} 1 \\ r_{ps}/r_{ss} \end{bmatrix}, \quad (2.25)$$

$$\mathbf{J}_{f,p} = \begin{bmatrix} r_{ss} & r_{sp} \\ r_{ps} & r_{pp} \end{bmatrix} \begin{bmatrix} 0 \\ 1 \end{bmatrix} = r_{pp} \begin{bmatrix} r_{sp}/r_{pp} \\ 1 \end{bmatrix}. \quad (2.26)$$

With this form explicitly written it is easy to recognize Eq. (2.6)⁷. When redefined for s polarized incident beam Eq. (2.6) yields

$$\tan \Theta_s e^{i\delta_{s,p}} = \frac{r_{ps}}{r_{ss}} = \frac{\tan \theta_s - i \tan \epsilon_s}{1 + i \tan \theta_s \tan \epsilon_s}. \quad (2.27)$$

As mentioned before, the ratio between off-diagonal and diagonal components is small, so the assumption, that ellipsometric angles θ_s and ϵ_s are very small is justified (see e.g. Figure 2.5 (d)). The small angle approximation allows us to perform Maclaurin expansion of θ_s and ϵ_s in (2.27) leaving only terms linear in θ_s , ϵ_s . With this, small angle approximation (2.27) takes a form

$$\frac{r_{ps}}{r_{ss}} = \theta_s - i\epsilon_s \equiv \Phi_s. \quad (2.28)$$

In the small-angle approximation θ_s and ϵ_s are real parameters often called Kerr rotation (azimuth of the resulting elliptical polarization) and Kerr ellipticity (ellipticity of resulting elliptical polarization). The complex parameter Φ_s is called complex angle of Kerr rotation.

Likewise, we can derive complex angle of Kerr rotation for p polarization -

$$\frac{r_{sp}}{r_{pp}} = \theta_p - i\epsilon_p \equiv \Phi_p. \quad (2.29)$$

In polarization measurements we are often only interested in the polarization changes and the absolute value of amplitude is not of much concern. In those situations Jones matrices of a sample can be normalized with the diagonal element. This element, since it is acting on both s and p rays equally, might be then omitted. Doing so for the matrix representing longitudinal Kerr effect yields

$$\hat{\mathbf{J}}_{\text{Long},s} = \begin{bmatrix} 1 & -\Phi_s \\ \Phi_s & r_{pp}/r_{ss} \end{bmatrix}. \quad (2.30)$$

In the end of this section it is crucial to note, that in the magneto-optical measurement we often have to deal with a mixture of various Kerr effects (described in Tab. 2.2). In the linear approximation relevant to this thesis (thin structures with height $\ll \lambda$ (wavelength of the incident light beam)) it is possible to use the linear combination of Jones matrices of the sample [58] to describe the whole problem.

With the knowledge of the Jones matrix of a sample and other matrices presented in Tab. 2.1 we should be able to model measured MO signals by finding a matrix operator converting known incident Jones vector \mathbf{J}_i to final Jones vector \mathbf{J}_f . One of possible approaches is presented in section 4.1.1.

⁷ Exponential phase retardation is left out since r_{ij} ($i, j \in \{s, p\}$) are complex thus the phase difference is given implicitly.

3. MAXWELL-EQUATIONS - ELECTROMAGNETIC WAVES IN MAGNETIZED MATTER

The purpose of this section is to derive the different refractive indices for the RCP and LCP waves in a magnetized matter and to use them to describe the propagation and reflection of the EM wave in the framework of the macroscopic field theory. The derivation is done following the work of Z. Q. Qiu and S. D. Bader published in 2000 [28]. Similar results might be obtained following the approach summarized by J. Zak in [59–62] or the work done by Š. Višňovský [63–65]. Slightly different approach have been shown by Hunt [58] and You [66]. Historically, the works by Zak and Višňovský use the framework of the 4×4 formalism presented by Yeh [67]. A different approach is illustrated in the book [68] written by M. Mansuripur, where the derivation is based on the Jones matrices and Jones vectors. We have chosen the approach given by Qiu and Bader because of its simplicity while it still yields an accurate results. To derive the formulas describing MO response we must first consider the physical background behind the MO effects. We start with a simple model allowing us to obtain the permittivity tensor of a magnetized sample. The only effect magnetization has on the light reflection is solely given by the change of the permittivity tensor with magnetization [55]. This tensor is then used to derive the wave equation in the magnetized matter. In the end of this section the results of the MO computation will be shown summarizing some interesting properties of MO response.

3.1 *Permittivity tensor*

The introductory section 2.3.1 dealt with the magneto-optical response of a sample without the deeper insight in the physical background of the problem. Before we start with the theoretical description, we first place some relevant restriction on the problem.

- The interband transition contribution to the MO effect does not play a role for the excitation wavelength $\lambda = 632.8 \text{ nm}$ [69].
- In the visible spectra, there is no interaction of the EM wave with the spin of the atom and only the orbital motion is altered¹ [69, 70].
- Only the interaction with the electric part of the EM wave is considered, since the ratio of the electric and magnetic forces acting on a charged particle is given by v/c with v being speed of the particle [69].

¹ This does not fully apply for the heavy Rare Earth elements.

- Magnetic spin can not follow the rapid changes of the magnetic part of the EM wave. The typical reaction times of the spin is in the ps region while the EM wave is in the fs [71, 70].

To describe the magneto-optical response we have to first find the permittivity tensor $\vec{\epsilon}$. Tensor $\vec{\epsilon}$ is a second rank tensor fulfilling the Onsanger relations in a form $\epsilon_{ij}(\mathbf{M}) = \epsilon_{ji}(-\mathbf{M})$ [55, 56]. The information we seek is the general form (non-zero elements) of the permittivity tensor rather than an accurate quantitative prediction of the individual elements. In the end, the values we put in our MO calculations will be obtained from our measurements or we can use the values given in the literature. The general form of $\vec{\epsilon}$ is obtained from the Taylor expansion of $\vec{\epsilon}$ with respect to \mathbf{M} [55, p. 68]. The resulting form exhibits the terms linear and quadratic in \mathbf{M} as well as it shows isotropic (diagonal) terms as well as anisotropic terms (off-diagonal) and its dependence on \mathbf{M} . Same form is obtained when following the approach based on the Drude-Lorentz model [72]. This particular model allows us to obtain the general form of $\vec{\epsilon}$ while retaining the physical clarity and the necessary physical insight.

The basic idea behind the Drude-Lorentz model is that we can treat the electron in an atom as a classical particle feeling internal forces: the linear returning force (Coulombian interaction) and also the "scattering" attenuating force linear in the velocity. From the external forces it is substituted to the Lorentz force in the form

$$\mathbf{F} = e \left(\mathbf{E} + \frac{d\mathbf{r}}{dt} \times \mathbf{B}_e \right), \quad (3.1)$$

where e is the elementary charge² and $\frac{d\mathbf{r}}{dt} = \mathbf{v}$ is the velocity of a particle (\mathbf{r} stands for the displacement of a particle from equilibrium position). Electric intensity \mathbf{E} is the one of the external electromagnetic wave while \mathbf{B}_e is the external magnetic field that is being static compared to the characteristic times of the changes in \mathbf{v} . The above description leads to the two particle system in a vacuum. The first particle is an immobile nucleus and the second one is the electron. The behavior of the electron in solids is discussed later.

In order to derive the Cartesian permittivity tensor we start with the equation of motion of the electron bound to the atom nucleus. Assuming again that the speed of the particle $|\mathbf{v}|$ is much smaller than the phase velocity of the light c and also that the displacement of the electron is much smaller than the wavelength of the incident wave, we can use the so called dipole approximation, and neglect the spatial dependence given by $\mathbf{k} \cdot \mathbf{r}$. The equation of motion of the electron reads [55]

$$m \frac{d^2\mathbf{r}}{dt^2} + m\Gamma \frac{d\mathbf{r}}{dt} + m\omega_0^2 \mathbf{r} - e \frac{d\mathbf{r}}{dt} \times \mathbf{B}_e = e\mathbf{E}, \quad (3.2)$$

with m being the mass of the particle, Γ being the linear viscous damping term and ω_0 stands for the eigenfrequency of the undamped oscillator. We assume \mathbf{B}_e to be homogeneous and time invariant, while $\mathbf{E} = \mathbf{E}_0 e^{-i\omega t}$.

² $e = -1.602 \cdot 10^{-19}$ C.

Before finding the solution of Eq. (3.2) we write down the linear material relations that serve us to convert the amplitudes of the electron motion to the susceptibility tensor $\vec{\chi}_e$ and consequently to the main goal of this section, to the permittivity tensor $\vec{\epsilon}$.

First, we interconnect the electron displacement with the electric polarization \mathbf{P} via

$$\mathbf{P} = ner = \epsilon_0 \vec{\chi}_e \mathbf{E}. \quad (3.3)$$

The electric polarization is defined as an electric dipole density in a material. Quantity n in Eq. (3.3) stand for the charge density in the material. Quite often when treating the response of a material to the external electric field we assume the material to be homogeneous and linear. Then the right side of Eq. (3.3) is valid and the assumption that the electric polarization \mathbf{P} is proportional to \mathbf{E} stands. For the relative permittivity, the connection with $\vec{\chi}_e$ is trivial:

$$\vec{\epsilon} = \vec{\mathbf{1}} + \vec{\chi}_e, \quad (3.4)$$

where the unitary tensor $\vec{\mathbf{1}}$ is defined via the Kronecker delta as $\vec{\mathbf{1}} = \delta_{ij}$. Combining Eq. (3.3) and Eq. (3.4) and writing the resulting form in the individual components we obtain

$$\frac{ner_i}{\epsilon_0} + E_i = \epsilon_{ij} E_j. \quad (3.5)$$

Applying the partial derivation of Eq. (3.5) by E_j yields

$$\epsilon_{ij} = \chi_{ij} + \delta_{ij} = \frac{ne}{\epsilon_0} \frac{\partial r_i}{\partial E_j} + \delta_{ij}. \quad (3.6)$$

With the help of Eq.(3.6) we are able to attribute the resulting electron displacement \mathbf{r} to $\vec{\epsilon}_r$.

In order to solve Eq. (3.2) we write it in individual Cartesian components:

$$\frac{d^2x}{dt^2} + \Gamma \frac{dx}{dt} + \omega_0^2 x + \frac{e}{m} \left(B_y \frac{dz}{dt} - B_z \frac{dy}{dt} \right) = \frac{e}{m} E_{x,0} e^{-i\omega t}, \quad (3.7)$$

$$\frac{d^2y}{dt^2} + \Gamma \frac{dy}{dt} + \omega_0^2 y + \frac{e}{m} \left(B_z \frac{dx}{dt} - B_x \frac{dz}{dt} \right) = \frac{e}{m} E_{y,0} e^{-i\omega t}, \quad (3.8)$$

$$\frac{d^2z}{dt^2} + \Gamma \frac{dz}{dt} + \omega_0^2 z + \frac{e}{m} \left(B_x \frac{dy}{dt} - B_y \frac{dx}{dt} \right) = \frac{e}{m} E_{z,0} e^{-i\omega t}. \quad (3.9)$$

Now we suppose the solution in a form of $\mathbf{r} = \mathbf{r}_0 e^{-i\omega t}$ which we substitute to Eq. (3.7)-(3.9). Obtaining the vector \mathbf{r}_0 from the set of equations (3.7)-(3.9) is straightforward but the involved algebra is not trivial. The solution for the electron displacement is

$$x_0 = \frac{[L^2 - (\frac{\omega e}{m} B_x)^2] E_x - [iL \frac{\omega e}{m} B_z + (\frac{\omega e}{m})^2 B_x B_y] E_y + [iL \frac{\omega e}{m} B_y - (\frac{\omega e}{m})^2 B_x B_z] E_z}{\frac{m}{e} D_0}, \quad (3.10)$$

$$y_0 = \frac{[iL \frac{\omega e}{m} B_z - (\frac{\omega e}{m})^2 B_x B_y] E_x + [L^2 - (\frac{\omega e}{m} B_y)^2] E_y - [iL \frac{\omega e}{m} B_x + (\frac{\omega e}{m})^2 B_y B_z] E_z}{\frac{m}{e} D_0}, \quad (3.11)$$

$$z_0 = \frac{-[iL \frac{\omega e}{m} B_y + (\frac{\omega e}{m})^2 B_x B_z] E_x + [iL \frac{\omega e}{m} B_x - (\frac{\omega e}{m})^2 B_y B_z] E_y + [L^2 - (\frac{\omega e}{m} B_z)^2] E_z}{\frac{m}{e} D_0}. \quad (3.12)$$

Where we used the substitution

$$L = \omega_0^2 - \omega - i\Gamma\omega \quad (3.13)$$

and

$$D_0 = L \left[L^2 - \left(\frac{\omega e}{m} B_x \right)^2 - \left(\frac{\omega e}{m} B_y \right)^2 - \left(\frac{\omega e}{m} B_z \right)^2 \right]. \quad (3.14)$$

The obtained results Eq. (3.10)-(3.12) are in a slight disagreement with the book [55] in a highlighted sign, whereas the resulting susceptibility (will be shown) agrees with the findings of the author. Now with the help of Eq. (3.6) we can calculate the susceptibility tensor carrying out the partial derivatives $\partial x_0/\partial E_i$, $\partial y_0/\partial E_i$, $\partial z_0/\partial E_i$, $i \in \{x, y, z\}$. The individual components of the permittivity tensor $\vec{\epsilon}$ are summarized in the Appendix A [equations (A.1)-(A.9)]. The permittivity tensor obtained from the simple Lorentz model takes the form of

$$\varepsilon_{ij} = \varepsilon_{ij}^0 + \sum_k a_{ijk} B_k + \sum_{kl} a_{ijkl} B_k B_l, \quad (3.15)$$

and we can easily verify that the Onsanger relations in the form $\varepsilon_{ij}(\mathbf{B}_e) = \varepsilon_{ji}(-\mathbf{B}_e)$ are fulfilled. This serves as a good check of the correctness of our results.

Now we split the tensor to the diagonally symmetric $\vec{\epsilon}_S$ and antisymmetric part $\vec{\epsilon}_{AS}$

$$\vec{\epsilon}_S = (\vec{\epsilon}_{ij} + \vec{\epsilon}_{ji})/2 = \frac{ne^2}{m} \begin{bmatrix} \left(\frac{L^2 - (\frac{\omega e}{m})^2 B_x^2}{\varepsilon_0 D_0} \right) + 1 & \frac{-(\frac{\omega e}{m})^2 B_x B_y}{\varepsilon_0 D_0} & \frac{-(\frac{\omega e}{m})^2 B_x B_z}{\varepsilon_0 D_0} \\ \frac{-(\frac{\omega e}{m})^2 B_x B_y}{\varepsilon_0 D_0} & \left(\frac{L^2 - (\frac{\omega e}{m})^2 B_y^2}{\varepsilon_0 D_0} \right) + 1 & \frac{-(\frac{\omega e}{m})^2 B_y B_z}{\varepsilon_0 D_0} \\ \frac{-(\frac{\omega e}{m})^2 B_x B_z}{\varepsilon_0 D_0} & \frac{-(\frac{\omega e}{m})^2 B_y B_z}{\varepsilon_0 D_0} & \left(\frac{L^2 - (\frac{\omega e}{m})^2 B_z^2}{\varepsilon_0 D_0} \right) + 1 \end{bmatrix}, \quad (3.16)$$

$$\vec{\epsilon}_{AS} = (\vec{\epsilon}_{ij} - \vec{\epsilon}_{ji})/2 = \begin{bmatrix} 0 & -\frac{nq^3\omega(iLB_z)}{\varepsilon_0 m^2 D_0} & \frac{nq^3\omega(iLB_y)}{\varepsilon_0 m^2 D_0} \\ \frac{nq^3\omega(iLB_z)}{\varepsilon_0 m^2 D_0} & 0 & \frac{nq^3\omega(iLB_x)}{\varepsilon_0 m^2 D_0} \\ -\frac{nq^3\omega(iLB_y)}{\varepsilon_0 m^2 D_0} & -\frac{nq^3\omega(iLB_x)}{\varepsilon_0 m^2 D_0} & 0 \end{bmatrix}, \quad (3.17)$$

where the linear magneto-optical effects are accounted solely to the antisymmetric part of the tensor $\vec{\epsilon}$ since the symmetric part can always be diagonalized by the proper rotation of the system hence it does not give rise to the magneto-optical observables [5, 28]. The symmetric part of $\vec{\epsilon}$ can be split to the zero field part and to the part dependent on \mathbf{B} , where \mathbf{B} dependent symmetric part $\vec{\epsilon}_S$ is quadratic in \mathbf{B} . The resulting effect on the light reflection affects only the intensity of the reflected light while the polarization state is conserved [73, 74]. This particular effect makes the application of the Transversal Kerr effect difficult (Jones matrix describing the Transversal Kerr effect is in the Table 2.1). In this thesis, despite the fact that the quadratic Kerr effect has been observed in the materials we study [73], we restrict ourselves only to the linear Kerr effect given by the antisymmetric dielectric tensor $\vec{\epsilon}_{AS}$. We study the MO effects by the polarization variation, thus we omit the quadratic part of $\vec{\epsilon}$ in our calculations. The resulting tensor reads

$$\overleftrightarrow{\boldsymbol{\varepsilon}} = \overleftrightarrow{\boldsymbol{\varepsilon}}^S + \overleftrightarrow{\boldsymbol{\varepsilon}}^{\text{AS}} = \frac{nq^2L^2 + \varepsilon_0D_0}{\varepsilon_0mD_0} \mathbf{1} + \begin{bmatrix} 0 & -\frac{nq^3\omega(iLB_z)}{\varepsilon_0m^2D_0} & \frac{nq^3\omega(iLB_y)}{\varepsilon_0m^2D_0} \\ \frac{nq^3\omega(iLB_z)}{\varepsilon_0m^2D_0} & 0 & \frac{nq^3\omega(iLB_x)}{\varepsilon_0m^2D_0} \\ -\frac{nq^3\omega(iLB_y)}{\varepsilon_0m^2D_0} & -\frac{nq^3\omega(iLB_x)}{\varepsilon_0m^2D_0} & 0 \end{bmatrix}. \quad (3.18)$$

To obtain the form of $\overleftrightarrow{\boldsymbol{\varepsilon}}$ often used in literature dealing with the MO response modeling (e.g. [28, 62, 64]) we normalize the off-diagonal elements by the diagonal element

$$Q_i = -\frac{\varepsilon_{ij}}{\varepsilon_{ii}}, \quad i, j \in \{x, y, z\} \quad (3.19)$$

with Q_i being the Magneto-optical Voigt constant [28, 75, 76]. By substituting the Voigt constant to the tensor given by Eq. (3.18) we obtain

$$\overleftrightarrow{\boldsymbol{\varepsilon}} = \varepsilon \begin{bmatrix} 1 & iQ_z & -iQ_y \\ -iQ_z & 1 & iQ_x \\ iQ_y & -iQ_x & 1 \end{bmatrix}, \quad (3.20)$$

where ε is the scalar relative permittivity³. In our model the sample is initially isotropic and could be characterized only by the scalar permittivity ε . When the magnetic field is present the optical anisotropy appears giving a rise to magneto-optical effects.

3.1.1 Some conventions connected with the permittivity tensor

The tensor given by Eq. (3.20) was obtained from a simple model that did not account for the various effects. This section corrects some shortcomings of the Lorentz model. Starting with the scalar permittivity ε , we note that the permittivity is a complex quantity in general [46]. It is connected to the complex index of refraction N by the following relation

$$N^2 = \varepsilon. \quad (3.21)$$

Another complex quantity is the Voigt constant. It will be shown later that the real part of Q_i is affecting the polarization rotation θ and the imaginary part is causing the ellipticity ϵ . By comparing Eq. (3.18) with Eq. (3.20) we see that Q_i is linear in B_i . Whereas the Lorentz model was obtained for the single dipole in a vacuum we intend to use the tensor ε in material. In materials such as metals the assumption of the electron as an oscillator still holds. However we have to use the sum of various oscillators characterizing particular transitions. Also the magnetic field \mathbf{B} used in the model is the magnetic field electron actually feels in the matter. This internal magnetic field is connected to the magnetization \mathbf{M} so the substitution of M_i for B_i is physically reasonable. Tensor of the form from Eq. (3.20) is often used in the literature supposing that $Q_i = Q_0m_i$ where m_i is the normalized component of magnetization vector \mathbf{M} . Supposing that the magnitude of the magnetization is constant, only the direction of the magnetization is changing, we can obtain general form of $\overleftrightarrow{\boldsymbol{\varepsilon}}$ where the desired tensor (according to the magnetization) can be easily found by specifying the spherical

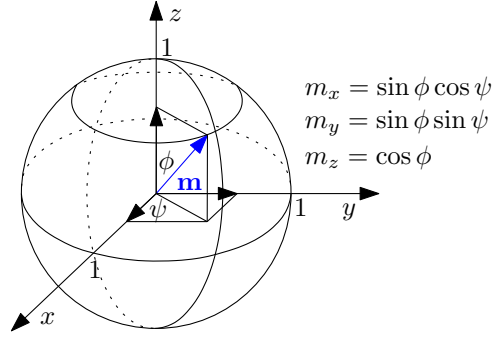


Fig. 3.1: Definition of the spherical angles of the unitary magnetization vector.

angles of the magnetization. Figure 3.1 defines the spherical angles. The Eq. (3.22) represents the general form of the permittivity tensor for the magnetization vector with an arbitrary direction

$$\vec{\varepsilon} = \varepsilon \begin{bmatrix} 1 & iQ_0 \cos \phi & -iQ_0 \sin \phi \sin \psi \\ -iQ_0 \cos \phi & 1 & iQ_0 \sin \phi \cos \psi \\ iQ_0 \sin \phi \sin \psi & -iQ_0 \sin \phi \cos \psi & 1 \end{bmatrix}. \quad (3.22)$$

The last convention presented applies to the anti-symmetric part of the tensor $\vec{\varepsilon}$. According to the authors [77] and [68, p. 130] the vector product operator $[\mathbf{A}\times]$ is equivalent to the following form of matrix multiplication (in a Cartesian basis)

$$[\mathbf{A}\times] \equiv \begin{bmatrix} 0 & -A_z & A_y \\ A_z & 0 & -A_x \\ -A_y & A_x & 0 \end{bmatrix}, \quad (3.23)$$

where we can recognize the anti-symmetric part of the derived tensor with $A_i = -iQ_i$. This particular equivalency allows us to define the so called Voigt vector $\mathbf{Q} = [Q_x, Q_y, Q_z]$.

To summarize this section we have used a simple model that yields the correct form of the antisymmetric linear permittivity tensor shown in Eq. (3.20). The resulting tensor does not show any coupling between the orthogonal bases of the magnetic field (or magnetization) so this form suggests, that with the proper geometrical alignment of the coordinate system we probe only the particular M_i .

3.2 Electro-magnetic waves in magnetized matter

This section deals with the propagation of the EM wave in the anisotropic medium, in which the anisotropy is induced solely by the magnetization. It is shown that the magnetization induces two different refractive indices for the right-handed and left-handed circular polarization states (RCP & LCP). The Jones vectors of the RCP and LCP polarizations form another orthogonal basis (apart from the Cartesian basis shown

³ The absolute permittivity is given by $\varepsilon^{\text{ABS}} = \varepsilon_0 \varepsilon$.

in Eq. (2.10)). We start by revising Maxwell's equations [47]

$$\nabla \cdot \mathbf{E} = \frac{\rho}{\varepsilon_0}, \quad (3.24)$$

$$\nabla \cdot \mathbf{B} = 0, \quad (3.25)$$

$$\nabla \times \mathbf{E} = -\frac{\partial \mathbf{B}}{\partial t}, \quad (3.26)$$

$$\nabla \times \mathbf{B} = \mu_0 \mathbf{j} + \mu_0 \varepsilon_0 \frac{\partial \mathbf{E}}{\partial t}. \quad (3.27)$$

The ρ is electric charge density, μ_0 is a vacuum permeability and \mathbf{j} represents the current density. By introducing the magnetization vector \mathbf{M} and electric polarization \mathbf{P} we can split ρ to the bound charges ρ_b and to the free charges ρ_f and \mathbf{j} can be split to the bound, free and polarizing currents (\mathbf{j}_b , \mathbf{j}_f , \mathbf{j}_p). The bound charges are obtained by applying the divergence operator on \mathbf{P} ($\rho_b = -\nabla \cdot \mathbf{P}$) and the bound currents are obtained by applying the curl operator on the magnetization ($\mathbf{j}_b = \nabla \times \mathbf{M}$). The polarizing currents are obtained from the continuity of the charges $\mathbf{j}_p = \frac{\partial \mathbf{P}}{\partial t}$. The charge density ρ present in the Gauss law Eq. (3.24) is given by the sum of the individual contributions ρ_b and ρ_f . With the definition of the auxiliary fields \mathbf{D} and \mathbf{H} we rewrite Maxwell's equations to the form

$$\nabla \cdot \mathbf{D} = \rho_f, \quad (3.28)$$

$$\nabla \cdot \mathbf{B} = 0, \quad (3.29)$$

$$\nabla \times \mathbf{E} = -\frac{\partial \mathbf{B}}{\partial t}, \quad (3.30)$$

$$\nabla \times \mathbf{H} = \mathbf{j}_f + \frac{\partial \mathbf{D}}{\partial t}. \quad (3.31)$$

To interconnect the auxiliary fields \mathbf{D} and \mathbf{H} with fields \mathbf{E} and \mathbf{B} we will use the material relationships incorporating the electric polarization \mathbf{P} and magnetization \mathbf{M} :

$$\mathbf{D} \equiv \varepsilon_0 \mathbf{E} + \mathbf{P}, \quad (3.32)$$

$$\mathbf{H} \equiv \frac{1}{\mu_0} \mathbf{B} + \mathbf{M}. \quad (3.33)$$

Assuming only small light intensities we suppose the medium to be linear (\mathbf{P} is linear with \mathbf{E} and \mathbf{M} is linear with \mathbf{H}). Consequently the material relations given by Eq. (3.32) and Eq. (3.33) are further simplified to the form

$$\mathbf{D} = \varepsilon_0 \mathbf{E} + \varepsilon_0 \overleftrightarrow{\chi}_e \mathbf{E} = \varepsilon_0 \overleftrightarrow{\varepsilon} \mathbf{E}, \quad (3.34)$$

$$\mathbf{B} = \mu_0 \mathbf{H} + \mu_0 \overleftrightarrow{\chi}_m \mathbf{H} = \mu_0 \overleftrightarrow{\mu} \mathbf{H}. \quad (3.35)$$

Where we used Eq. (3.4) and its equivalent for $\overleftrightarrow{\mu}$. As already mentioned in the beginning of the section 3.1 at the optical frequencies $\overleftrightarrow{\mu} = \overleftrightarrow{\mathbf{1}}$. Now we use the tensor $\overleftrightarrow{\varepsilon}$ given by Eq. (3.20) while expressing the antisymmetric part using the Voigt vector \mathbf{Q} [Eq. (3.23)]. Eq. (3.34) takes a form

$$\mathbf{D} = \varepsilon_0 \varepsilon (\mathbf{E} + \mathbf{iE} \times \mathbf{Q}). \quad (3.36)$$

This is a very important result since it directly proves that for the s-polarized beam the transverse magnetization (characterized by Voigt vector \mathbf{Q}_T) has no effect on the light propagation at all ($\mathbf{Q}_T \parallel \mathbf{E}$).

In the following text we omit free currents and free charges [68]. The plane wave solution given by Eq. (2.1) for \mathbf{E} and \mathbf{B} is the solution to Maxwell's equations when the following equations are satisfied:

$$\mathbf{k} \cdot \mathbf{E}_0 + i\mathbf{k} \cdot (\mathbf{E}_0 \times \mathbf{Q}) = 0, \quad (3.37)$$

$$\mathbf{k} \cdot \mathbf{H}_0 = 0, \quad (3.38)$$

$$\mathbf{k} \times \mathbf{E}_0 = \omega\mu_0\mathbf{H}_0, \quad (3.39)$$

$$\mathbf{k} \times \mathbf{H}_0 = -\omega\varepsilon_0\varepsilon(\mathbf{E}_0 + i\mathbf{E}_0 \times \mathbf{Q}), \quad (3.40)$$

here \mathbf{E}_0 and \mathbf{H}_0 are the amplitude vectors of the electromagnetic wave.

Following the basic properties of the dot and cross products we see that vectors \mathbf{k} , \mathbf{D} , \mathbf{H} (and \mathbf{B}) are mutually perpendicular, while \mathbf{E} lies in a plane perpendicular to \mathbf{H} . Without the presence of magnetization \mathbf{M} ($\mathbf{Q} = \mathbf{0}$) \mathbf{E} , \mathbf{B} and \mathbf{k} form a right handed coordinate system while in the presence of \mathbf{M} ; vector \mathbf{E} has a non-zero component in the direction of \mathbf{k} . Also, only two of the above equations are independent. When Eq. (3.40) is multiplied by the vector \mathbf{k} , equation (3.37) is obtained. The same approach applies to Eq. (3.38) and (3.39). The wave equation is obtained by multiplying Eq. (3.39) by $\mathbf{k} \times$. Then the right side of the equation is replaced using Eq. (3.40)

$$\mathbf{k} \times (\mathbf{k} \times \mathbf{E}_0) = \mathbf{k}(\mathbf{k} \cdot \mathbf{E}_0) - \mathbf{E}_0(\mathbf{k} \cdot \mathbf{k}) = -\omega^2\varepsilon_0\mu_0\varepsilon(\mathbf{E}_0 + i\mathbf{E}_0 \times \mathbf{Q}) \Leftrightarrow \quad (3.41)$$

$$\Leftrightarrow \left(|\mathbf{k}|^2 - \frac{\omega^2\varepsilon}{c^2} \right) \mathbf{E}_0 = \mathbf{k}(\mathbf{k} \cdot \mathbf{E}_0) + \frac{i\omega^2\varepsilon}{c^2} \mathbf{E}_0 \times \mathbf{Q}, \quad (3.42)$$

with $c^2 = 1/(\varepsilon_0\mu_0)$. Without the loss in generality we suppose the light propagation vector \mathbf{k} in the form

$$\mathbf{k} = \begin{bmatrix} 0 \\ 0 \\ k \end{bmatrix}, \quad (3.43)$$

then \mathbf{E}_0 is in the form of s, p and k polarized eigenmodes

$$\mathbf{E}_0 = \begin{bmatrix} E_s \\ E_p \\ E_k \end{bmatrix}. \quad (3.44)$$

Now we split Eq. (3.42) to the orthogonal basis \mathbf{e}_s , \mathbf{e}_p and \mathbf{e}_k . After some algebra we obtain

$$\left(\frac{\omega^2\varepsilon}{c^2} - k^2 \right) E_s = \frac{i\omega^2\varepsilon}{c^2} (\mathbf{Q} \cdot \mathbf{e}_p E_k - \mathbf{Q} \cdot \mathbf{e}_k E_p), \quad (3.45)$$

$$\left(\frac{\omega^2\varepsilon}{c^2} - k^2 \right) E_p = \frac{i\omega^2\varepsilon}{c^2} (\mathbf{Q} \cdot \mathbf{e}_k E_s - \mathbf{Q} \cdot \mathbf{e}_s E_k), \quad (3.46)$$

$$E_k = i(\mathbf{Q} \cdot \mathbf{e}_s E_p - \mathbf{Q} \cdot \mathbf{e}_p E_s). \quad (3.47)$$

The nontrivial solution for the amplitudes E_s , E_p , E_k to the above set of equations is obtained when the determinant of the coefficient matrix is zero. Solving the determinant for 3×3 matrix is problematic, but can be found in the literature [55, 48]. Solving a 3×3 determinant has the advantage of finding the eigenvalues and eigenvectors without any approximation. We make a use of Eq. (3.47) by putting it to Eq. (3.46) and Eq. (3.45) and neglecting terms quadratic in \mathbf{Q} we get an equation of motion for s and p polarization [28]:

$$\left(\frac{\omega^2 \varepsilon}{c^2} - k^2\right) E_s + \frac{i\omega^2 \varepsilon \mathbf{Q} \cdot \mathbf{e}_k}{c^2} E_p = 0, \quad (3.48)$$

$$-\frac{i\omega^2 \varepsilon \mathbf{Q} \cdot \mathbf{e}_k}{c^2} E_s + \left(\frac{\omega^2 \varepsilon}{c^2} - k^2\right) E_p = 0. \quad (3.49)$$

Justification for neglecting the quadratic \mathbf{Q} contribution is that the vector \mathbf{Q} magnitude is generally small compared to the diagonal permittivity values. For the polar Kerr effect no approximation is needed. Equations (3.48) and (3.49) show the intermode coupling induced by the vector \mathbf{Q} . Modes E_s and E_p are phase-shifted by $e^{i\frac{\pi}{2}}$. The minus sign for E_s in the second equation suggests the circular-wave-like solution (see Eq. (2.11)). The nontrivial solution is found for the determinant of the coefficient matrix equal to zero

$$\begin{vmatrix} 1 - \frac{c^2 k^2}{\omega^2 \varepsilon} & -i\mathbf{Q} \cdot \mathbf{e}_k \\ i\mathbf{Q} \cdot \mathbf{e}_k & 1 - \frac{c^2 k^2}{\omega^2 \varepsilon} \end{vmatrix} = 0 \Leftrightarrow \quad (3.50)$$

$$\Leftrightarrow \left(1 - \frac{c^2 k^2}{\omega^2 \varepsilon}\right)^2 = -(i\mathbf{Q} \cdot \mathbf{e}_k)^2 \Leftrightarrow \quad (3.51)$$

$$\Leftrightarrow 1 - \frac{c^2 k^2}{\omega^2 \varepsilon} = \pm \mathbf{Q} \cdot \mathbf{e}_k. \quad (3.52)$$

The resulting equation is not a solution to the general problem but it places some restrictions on the propagation vector \mathbf{k} . The problem we are dealing with is the eigenvalue problem with k_j being the eigenvalue and \mathbf{E}_j are the eigen-vectors. The determinant originally yielded fourth order polynomial in k which shows that generally there are 4 waves propagating in the MO media and that mathematically any other wave is given by the proper linear combination of those four particular waves. Isolating the solution for k , we obtain

$$k^\pm = \pm k_0 \sqrt{1 \mp \mathbf{Q} \cdot \mathbf{e}_k}. \quad (3.53)$$

Here $k_0 = \frac{\omega}{c} \sqrt{\varepsilon}$ is the unperturbed wave vector without the presence of the magnetization. The k^\pm modes differ in sign and are called forward and backward modes [59]. It represents the wave traveling in $+\mathbf{e}_k$ and $-\mathbf{e}_k$ direction. Again assuming \mathbf{Q} to be small, we use the binomial expansion, for the forward mode with which we get

$$k^+ = k_0 \left(1 \mp \frac{1}{2} \mathbf{Q} \cdot \mathbf{e}_k\right). \quad (3.54)$$

The unperturbed wave vector is connected with the index of refraction by $n = \frac{c}{\omega}k$ thus we can express the change in the refractive index for the forward mode as

$$n = \sqrt{\varepsilon} \left(1 \mp \frac{1}{2} \mathbf{Q} \cdot \mathbf{e}_k \right) = n_0 \left(1 \mp \frac{1}{2} \mathbf{Q} \cdot \mathbf{e}_k \right). \quad (3.55)$$

We arrive at result of the utter importance for the scope of this thesis. This result implies that the change in the index of refraction is given by the dot product of the magnetization vector (represented by \mathbf{Q}) and the light propagation vector \mathbf{k} . The linear form (in \mathbf{Q}) of Eq. (3.55) implicitly allows to separate the effect of the individual components of \mathbf{Q} . In the end of this section we present a simple way to separate the effect of individual magnetization components to the measured signal.

When the obtained k_j (Eq. (3.53)) are inserted into the equations of motion (3.45)-(3.47) we arrive to two eigenvectors in form of (to the first power of \mathbf{Q}) right-handed and left-handed circular polarization. The following table 3.1 summarizes the set of eigen-values and eigen-vectors of the problem. Then the arbitrary wave is described as the linear superposition of the four proper modes

$$\mathbf{E} = \sum_{j=1}^4 \mathbf{E}_j e^{-i(\omega t - \mathbf{k}_j \cdot \mathbf{r})}. \quad (3.56)$$

Tab. 3.1: Table presenting the obtained eigenvalues and eigenvectors for the light propagating in the magnetized medium. Wave-numbers k_1 and k_3 are forward traveling modes and k_2 and k_4 are backwards traveling modes. For the wave-numbers k_1 and k_2 the resulting polarization is right-handed and wave-numbers k_3 and k_4 form the left-handed-polarization.

$k_1 = k_0 \left(1 + \frac{1}{2} \mathbf{Q} \cdot \mathbf{e}_k \right)$	\mathbf{e}_G	$\mathbf{E}_1 = \begin{bmatrix} E_s^+ \\ iE_p^+ \\ 0 \end{bmatrix}$
$k_2 = -k_0 \left(1 - \frac{1}{2} \mathbf{Q} \cdot \mathbf{e}_k \right)$	\mathbf{e}_G	$\mathbf{E}_2 = \begin{bmatrix} E_s^+ \\ iE_p^+ \\ 0 \end{bmatrix}$
$k_3 = k_0 \left(1 - \frac{1}{2} \mathbf{Q} \cdot \mathbf{e}_k \right)$	\mathbf{e}_G	$\mathbf{E}_3 = \begin{bmatrix} E_s^- \\ -iE_p^- \\ 0 \end{bmatrix}$
$k_4 = -k_0 \left(1 + \frac{1}{2} \mathbf{Q} \cdot \mathbf{e}_k \right)$	\mathbf{e}_G	$\mathbf{E}_4 = \begin{bmatrix} E_s^- \\ -iE_p^- \\ 0 \end{bmatrix}$

3.2.1 4×4 matrix formalism

Up to now we have shown that in the magnetized matter four proper modes are present. The following text uses the obtained refractive indices and the proper modes to develop

a general approach allowing one to solve the magneto-optic response of almost any layered structure. The derivation is done following the work by Zak [59, 60, 62] whereas the obtained expressions are given in the form resembling article [28]. First in Fig. 3.2 (a) we define the coordinate system. In the next step we define the transfer matrix $\hat{\mathbf{A}}$

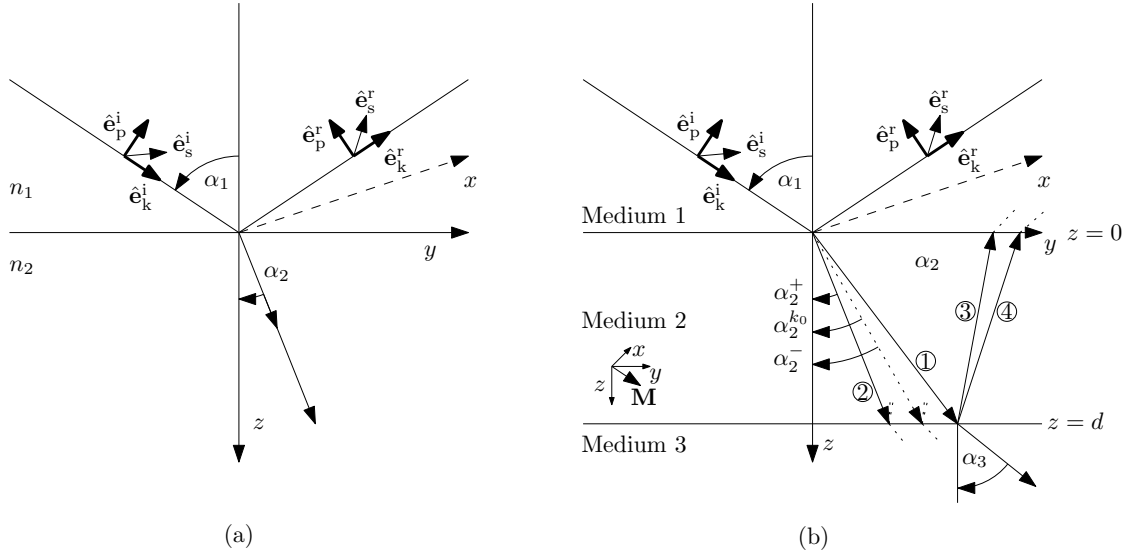


Fig. 3.2: (a) Definition of the coordinate system used in the derivation of the magneto-optical response for two-medium one boundary problem. (b) depicts the propagation of the four proper modes. Angle $\alpha_2^{k_0}$ characterizes non-perturbed wave propagation (for zero magnetization). After [60].

relating incident s and p polarized beams to the tangential components of the electric and magnetic field. It follows from Maxwell's equations that at the boundary between two media the tangential components of vectors \mathbf{E} and \mathbf{H} (in our case even \mathbf{B}) are conserved [47]. With the definition of the boundary-field vector \mathbf{F} and so called P-vector \mathbf{P} , the task is to find the matrix $\hat{\mathbf{A}}$ satisfying the following relation

$$\mathbf{F} = \begin{bmatrix} E_x \\ E_y \\ H_x \\ H_y \end{bmatrix} = \hat{\mathbf{A}} \begin{bmatrix} E_s^i \\ E_p^i \\ E_s^r \\ E_p^r \end{bmatrix}. \quad (3.57)$$

We rewrite the vector \mathbf{E}_0 using equations (3.45)-(3.47) to the unitary vector form

$$\mathbf{E}_0 = E_s \mathbf{e}_s + E_p \mathbf{e}_p + i(\mathbf{Q} \cdot \mathbf{e}_s E_p - \mathbf{Q} \cdot \mathbf{e}_p E_s). \quad (3.58)$$

The Cartesian electric field components E_s and E_p are related to the circular modal amplitudes by

$$E_s = E_s^+ + E_s^- = i(E_p^+ - E_p^-), \quad (3.59)$$

$$E_p = E_p^+ + E_p^-. \quad (3.60)$$

On the medium boundary the resulting field is given by the superposition of the incident and the reflected beam. The relation between s and p wave and the x component of the electric field is trivial, since the s beam is parallel to the x axis. The E_x

component is given by

$$E_x = E_s^i + E_s^r. \quad (3.61)$$

The E_y component is partially given by the E_p component and also by the E_k component. The following relation is derived from the geometrical considerations given by Fig. 3.2

$$\begin{aligned} E_y = & E_p^{i,+} \cos \alpha_2^+ + E_p^{i,-} \cos \alpha_2^- + i \left(\mathbf{Q} \cdot \mathbf{e}_s^i E_p^i - \mathbf{Q} \cdot \mathbf{e}_p^i E_s^i \right) \sin \alpha_2^{k_0} - \\ & - E_p^{r,+} \cos \alpha_2^+ - E_p^{r,-} \cos \alpha_2^- + i \left(\mathbf{Q} \cdot \mathbf{e}_s^r E_p^r - \mathbf{Q} \cdot \mathbf{e}_p^r E_s^r \right) \sin \alpha_2^{k_0}. \end{aligned} \quad (3.62)$$

Here we used the left and right circular modes and its associated angles of refraction shown in Fig. 3.4. The E_z component is derived similarly:

$$\begin{aligned} E_z = & -E_p^{i,+} \sin \alpha_2^+ - E_p^{i,-} \sin \alpha_2^- + i \left(\mathbf{Q} \cdot \mathbf{e}_s^i E_p^i - \mathbf{Q} \cdot \mathbf{e}_p^i E_s^i \right) \cos \alpha_2^{k_0} - \\ & - E_p^{r,+} \sin \alpha_2^+ - E_p^{r,-} \sin \alpha_2^- - i \left(\mathbf{Q} \cdot \mathbf{e}_s^r E_p^r - \mathbf{Q} \cdot \mathbf{e}_p^r E_s^r \right) \cos \alpha_2^{k_0}. \end{aligned} \quad (3.63)$$

At this point we use the derived eigen-values and eigen-vectors from the table 3.1. We also use the fact, that the wave vector component perpendicular to the boundary plane k_\perp is conserved when transferred from *medium 1* to *medium 2*. This is very important consequence of Maxwell's equations applied to the boundary problem. The k_\perp conservation is generally known as the Snell's law [46]:

$$n_0 \sin \alpha_2^{k_0} = n^+ \sin \alpha_2^+ = n^- \sin \alpha_2^- \quad (3.64)$$

with n^+ and n^- being refractive indices for the right and left circular polarization. Using the Snell's law we express $\sin \alpha_2^\pm$ with the non-perturbed angle of refraction $\alpha_2^{k_0}$:

$$\sin \alpha_2^\pm = \frac{n_0}{n^\pm} \sin \alpha_2^{k_0} = \frac{n_0}{n_0 \left(1 \mp \frac{1}{2} \mathbf{Q} \cdot \mathbf{e}_k \right)} \sin \alpha_2^{k_0} \approx \left(1 \pm \frac{1}{2} \mathbf{Q} \cdot \mathbf{e}_k \right) \sin \alpha_2^{k_0}. \quad (3.65)$$

and $\cos \alpha_2^\pm$ is then derived using a trigonometric identity: $\sin^2 \alpha + \cos^2 \alpha = 1$

$$\cos \alpha_2^\pm = \sqrt{1 - \left(\frac{n_0}{n^\pm} \sin \alpha_2^{k_0} \right)^2} \approx \left(1 \mp \frac{1}{2} \mathbf{Q} \cdot \mathbf{e}_k \tan^2 \alpha_2^{k_0} \right) \cos \alpha_2^{k_0}. \quad (3.66)$$

Those approximate expressions when used with the equations (3.59)-(3.60) and inserted into the equation (3.62) give the expression for E_y without circular modes:

$$\begin{aligned} E_y = & \frac{i}{2} \left(-Q_y \tan \alpha_2^{k_0} (1 + \cos^2 \alpha_2^{k_0})^2 + Q_z \sin^2 \alpha_2^{k_0} \right) E_s^i + (\cos \alpha_2^{k_0} + i Q_x \sin \alpha_2^{k_0}) E_p^i + \\ & + \frac{i}{2} \left(Q_y \tan \alpha_2^{k_0} (1 + \cos^2 \alpha_2^{k_0})^2 + Q_z \sin^2 \alpha_2^{k_0} \right) E_s^r + (-\cos \alpha_2^{k_0} + i Q_x \sin \alpha_2^{k_0}) E_p^r. \end{aligned} \quad (3.67)$$

Components H_x and H_y also figuring in the boundary-field vector [Eq. (3.57)] are obtained from Maxwell-Faraday law [Eq. (3.39)]:

$$\mathbf{H} = \frac{1}{\omega \mu_0} \mathbf{k} \times \mathbf{E}, \quad (3.68)$$

then $H_x = \frac{k_y}{\mu_0\omega} E_z - \frac{k_z}{\mu_0\omega} E_y$ which reads

$$H_x = \frac{in_0}{2} (Q_y \sin \alpha_2^{k_0} + Q_z \cos \alpha_2^{k_0}) E_s^i - n_0 E_p^i + \frac{in_0}{2} (Q_y \sin \alpha_2^{k_0} - Q_z \cos \alpha_2^{k_0}) E_s^r - n_0 E_p^r, \quad (3.69)$$

and $H_y = \frac{k_z}{\mu_0\omega} E_x$ which reads:

$$H_y = n_0 \cos \alpha_2^{k_0} E_s^i + \frac{in_0}{2} (Q_y \tan \alpha_2^{k_0} + Q_z) E_p^i - n_0 \cos \alpha_2^{k_0} E_s^r - \frac{in_0}{2} (Q_y \tan \alpha_2^{k_0} - Q_z) E_p^r. \quad (3.70)$$

With the knowledge of relations (3.61), (3.67), (3.69) and (3.70) we can connect E_x , E_y , H_x , H_y to the incident and reflected s and p waves. The transfer matrix $\hat{\mathbf{A}}$ then reads

$$\hat{\mathbf{A}} = \begin{bmatrix} 1 & 0 \\ \frac{i}{2} \left(-Q_y \frac{\beta_y}{\beta_z} (1 + \beta_z^2) + Q_z \beta_y^2 \right) & \beta_z + iQ_x \beta_y \\ \frac{in_0}{2} (Q_y \beta_y + Q_z \beta_z) & -n_0 \\ n_0 \beta_z & \frac{in_0}{2} (Q_y \frac{\beta_y}{\beta_z} + Q_z) \\ 1 & 0 \\ \frac{i}{2} \left(Q_y \frac{\beta_y}{\beta_z} (1 + \beta_z^2) + Q_z \beta_y^2 \right) & -\beta_z + iQ_x \beta_y \\ \frac{in_0}{2} (Q_y \beta_y - Q_z \beta_z) & -n_0 \\ -n_0 \beta_z & -\frac{in_0}{2} (Q_y \frac{\beta_y}{\beta_z} - Q_z) \end{bmatrix}, \quad (3.71)$$

where we used the substitution $\beta_z = \cos \alpha_2^{k_0}$ and $\beta_y = \sin \alpha_2^{k_0}$. The matrix (3.71) is in agreement with the article [28] whereas Zak in his original work describes the magnetization as the unit vector defined by its spherical angles as shown in figure 3.1 [62]. The transfer matrix $\hat{\mathbf{A}}$ effectively describes the boundary conditions for the in-plane components of the electric and magnetic field. It relates the P-vectors in two neighboring layers through following simple relationship

$$\hat{\mathbf{A}}_1 \mathbf{P}_1 = \hat{\mathbf{A}}_2 \mathbf{P}_2. \quad (3.72)$$

For a multilayered system we have to consider also the phase changes of the wave propagating in the magnetized matter. The task is to find the propagation matrix $\hat{\mathbf{D}}$ connecting two \mathbf{P} vectors at both interfaces of the one layer. If we consider the propagation of the wave from $z = 0$ to $z = d$, then the phase change for the x component of the four proper modes is given by:

$$E_x^j(z = 0) = E_x^j(z = d) e^{ik_j \beta_z^j d}, \quad j \in \{1, 2, 3, 4\}. \quad (3.73)$$

With the help of equations (3.59)-(3.61) and also by evaluating the expression $k_j \beta_z^j$ we arrive to the following D-matrix [28]:

$$\hat{\mathbf{D}} = \begin{bmatrix} U \cos \delta_i & U \sin \delta_i & 0 & 0 \\ -U \sin \delta_i & U \cos \delta_i & 0 & 0 \\ 0 & 0 & U^{-1} \cos \delta_r & -U^{-1} \sin \delta_r \\ 0 & 0 & U^{-1} \sin \delta_r & U^{-1} \cos \delta_r \end{bmatrix}, \quad (3.74)$$

with $U = e^{-ikd \cos \alpha_2^{k_0}}$, $\delta_i = \frac{k_0 d}{2}(Q_y \tan \alpha_2^{k_0} + Q_z)$ and $\delta_r = \frac{k_0 d}{2}(Q_y \tan \alpha_2^{k_0} - Q_z)$.

Now we make a use of Eq. (3.72) and we write down the set of linear equations for the magneto-optical coefficients for a two boundary three medium system:

$$\hat{\mathbf{A}}_1 \mathbf{P}_1 = \hat{\mathbf{A}}_2 \mathbf{P}_2(z=0) = \hat{\mathbf{A}}_2 \hat{\mathbf{D}}_2 \mathbf{P}_2(d) = \hat{\mathbf{A}}_2 \hat{\mathbf{D}}_2 \hat{\mathbf{A}}_2^{-1} \hat{\mathbf{A}}_2 \mathbf{P}_2(d) = \hat{\mathbf{A}}_2 \hat{\mathbf{D}}_2 \hat{\mathbf{A}}_2^{-1} \hat{\mathbf{A}}_3 \mathbf{P}_3(d). \quad (3.75)$$

What is impressive about Eq. (3.75) is its universality. It allows the description of the problem where the layer and the substrate is non-magnetic, one of them is magnetic or both are magnetic. The result (3.75) can be easily expanded to recursive expression for N layers

$$\hat{\mathbf{A}}_i \mathbf{P}_i = \prod_{m=1}^N (\hat{\mathbf{A}}_m \mathbf{P}_m \hat{\mathbf{A}}_m^{-1}) \hat{\mathbf{A}}_f \mathbf{P}_f, \quad (3.76)$$

where we further multiply the obtained result by the inverse matrix $\hat{\mathbf{A}}_i^{-1}$ and we define the matrix $\hat{\mathbf{M}}$ directly relating \mathbf{P}_f to \mathbf{P}_i

$$\mathbf{P}_i = \hat{\mathbf{A}}_i^{-1} \prod_{m=1}^N (\hat{\mathbf{A}}_m \mathbf{P}_m \hat{\mathbf{A}}_m^{-1}) \hat{\mathbf{A}}_f \mathbf{P}_f = \hat{\mathbf{M}} \mathbf{P}_f. \quad (3.77)$$

From the matrix $\hat{\mathbf{M}}$ we can directly obtain the Jones matrices given by (2.15) and (2.16). The derivation is straightforward and is shown in e.g. [48, p. 58]. In [28] and [62] they split the resulting $\hat{\mathbf{M}}$ matrix to four sub-matrices as follows

$$\hat{\mathbf{M}} = \begin{bmatrix} \hat{\mathbf{G}} & \hat{\mathbf{H}} \\ \hat{\mathbf{I}} & \hat{\mathbf{J}} \end{bmatrix}, \quad (3.78)$$

and then the Jones matrix describing the transmission is given by

$$\hat{\mathbf{J}}_T^C = \begin{bmatrix} t_{ss} & t_{sp} \\ t_{ps} & t_{pp} \end{bmatrix} = \hat{\mathbf{G}}^{-1}, \quad (3.79)$$

and the Jones matrix describing the reflection is obtained with the following relation

$$\hat{\mathbf{J}}_R^C = \begin{bmatrix} r_{ss} & r_{sp} \\ r_{ps} & r_{pp} \end{bmatrix} = \hat{\mathbf{I}} \hat{\mathbf{G}}^{-1}, \quad (3.80)$$

where the small Kerr angles θ and ϵ are obtained using equations (2.28) and (2.29):

$$\frac{r_{ps}}{r_{ss}} = \theta_s - i\epsilon_s \equiv \Phi_s, \quad (3.81)$$

$$\frac{r_{sp}}{r_{pp}} = \theta_p - i\epsilon_p \equiv \Phi_p. \quad (3.82)$$

We developed a LabView program capable of calculating the magneto-optical response for arbitrary number of layers, where for every layer the user can specify its optical properties as well as the orientation of the magnetization. The correct operation of the program was verified by repeating the MO calculations presented in [62]. Another set of calculations has been carried out for the 30 nm thick layer of Permalloy ($\text{Ni}_{80}\text{Fe}_{20}$)

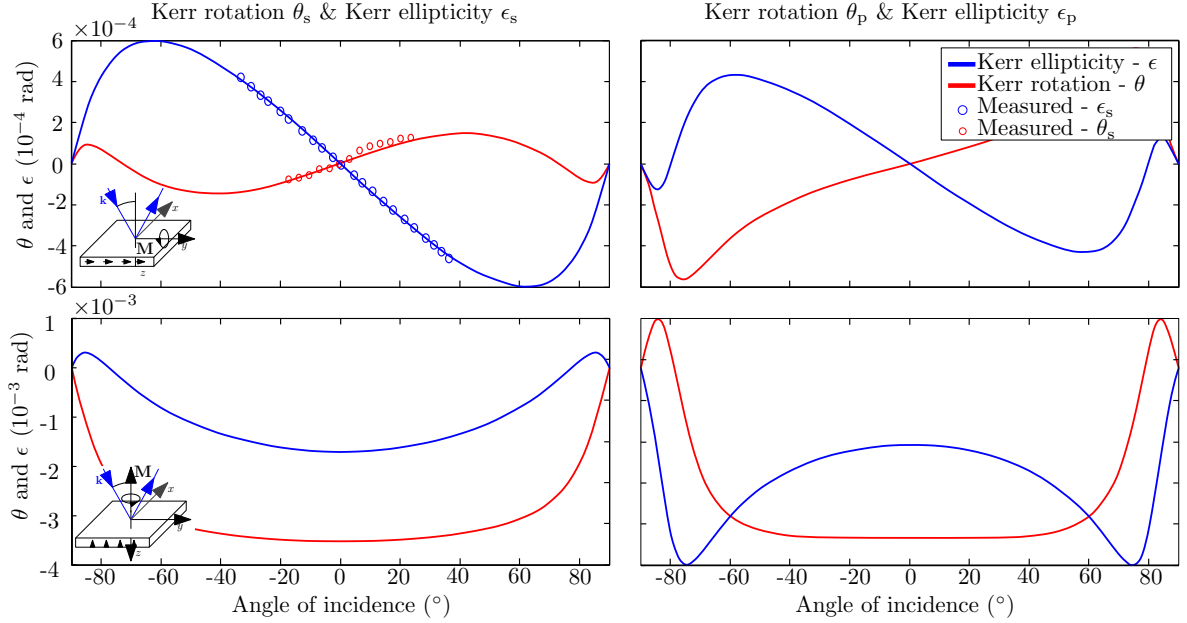


Fig. 3.3: Simulated and measured magneto-optical observables as a function of the angle of incidence for the longitudinal (top) and polar (bottom) magnetization. In the left part, the incident beam is s-polarized and in the right part the beam is p-polarized. For the calculations we used the following optical constants: index of refraction for the substrate $n_{\text{Si}} = 3.678 + 0.005i$, refractive index for the Permalloy $n_{\text{Py}} = 1.915 + 4.0256i$ and the Voigt constant for the upper data $Q_y = 0.00492 - 0.01316i$ and for the lower data $Q_z = 0.00492 - 0.01316i$. It is apparent that the Kerr rotation and the Kerr ellipticity are even (odd) functions of the angle of the incidence in the presence of the polar (longitudinal) magnetization. The measured data has been obtained using the system 4.3 presented in chapter 5.

on Si substrate for the wavelength $\lambda = 633\text{nm}$. Optical constants for Si layer were obtained from the ellipsometric measurements on the instrument Woollam V-VASE. The optical properties of the Permalloy layer were initially taken from M. Veis from the Faculty of mathematics and physics of the Charles University in Prague. Subsequently the original values were slightly varied in order to fit to the measured data. In our model we use the system Si (bulk)/Py (30 nm) where we are omitting the oxide layer at the permalloy boundaries. Hence the presented optical constants for permalloy are effective values and not the absolute ones. The plot of the calculated and measured dependencies of Kerr ellipticity and Kerr rotation as a function of the incident angle is presented in Fig. 3.3. For the longitudinal magnetization it shows vanishing MO quantities for normal incidence as would be expected since the dot product in Eq. (3.55) is equal to zero and there is no difference between the two circular modes. Another important consequence that stems from the dot product in (3.55) is that the MO observables for the longitudinal geometry are odd functions in the angle of incidence. For the same optical properties and the same geometry with the magnetization out-of-plane ($Q_x = Q_y = 0, Q_z \neq 0$) the curves are entirely different. Note that the amplitude of the longitudinal Kerr is an order lower than of the polar Kerr

effect. Where the longitudinal Kerr effect exhibits the odd dependence in the angle of incidence, the polar Kerr effect shows an even dependence. Another important fact arising from the developed formalism is that for the transverse magnetization the MO quantities are non-zero only for the p-polarized beam, as would be expected since the cross product $\mathbf{E} \times \mathbf{Q}$ for the s-polarized beam is equal to zero.

The basic consequence of the two modal refractive indices shown in Eq. (3.55) can be clearly seen from the four graphs 3.3. All four magneto-optical quantities ϵ_s , θ_s , ϵ_p , θ_p are odd/even in the angle of incidence in the presence of the polar/longitudinal magnetization respectively. To show how to phenomenologically separate individual components of \mathbf{Q} let us assume two cases depicted in Fig. 3.4. With the s-polarized

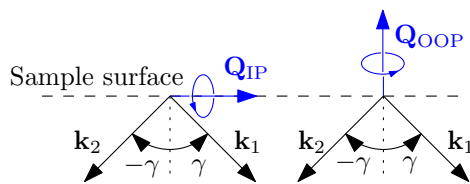


Fig. 3.4: Figure showing the basic properties of the dot product for the in-plane (IP) and out-of-plane (OOP) oriented \mathbf{Q} . When \mathbf{k} vector is mirrored, the dot product $\mathbf{Q} \cdot \mathbf{e}_k$ for the in-plane-magnetization changes sign whereas the dot product for the out-of-plane magnetization is conserved.

beam and by the proper geometrical arrangement of the experiment we are able to separate the effect induced by the out-of-plane (OOP) magnetization and by the in-plane (IP) magnetization simply by exploiting the asymmetry (for IP magnetization) and the symmetry (for OOP magnetization) when mirroring the vector \mathbf{k} by the plane perpendicular to the in-plane magnetization. When measuring the Kerr ellipticity, the superposition of two signals can be described as follows

$$\epsilon_s^{\pm\gamma} = \epsilon_s^P \pm \epsilon_s^L, \quad (3.83)$$

with $\epsilon_s^P, \epsilon_s^L$ being the Kerr ellipticity induced by the polar and longitudinal magnetization. With the knowledge of Eq. 3.83 we can disentangle Polar Kerr ellipticity (ϵ_s^P) and the longitudinal Kerr ellipticity (ϵ_s^L) by the following procedure

$$\epsilon_s^P = \frac{1}{2}(\epsilon_s^{+\gamma} + \epsilon_s^{-\gamma}), \quad (3.84)$$

$$\epsilon_s^L = \frac{1}{2}(\epsilon_s^{+\gamma} - \epsilon_s^{-\gamma}). \quad (3.85)$$

This procedure allows us to obtain two components of the magnetization vector. The missing transverse component is obtained by rotating the \mathbf{k} vector by $\pi/2$ around the sample normal and then by repeating the same procedure. It is important to note that when rotating the \mathbf{k} vector by $\pi/2$ the incident light polarization also has to be changed in order to keep the beam s-polarized. Leaving the incident polarization unchanged would lead to measuring the mix of the longitudinal and transversal magnetization. Thus by performing four consecutive measurements we are able to get complete information on the magnetization where the OOP magnetization is measured redundantly.

The two measurements of OOP component can further serve as an important consistency check.

3.2.2 Ultra-thin film limit

Previous derivation has been carried out without any approximation placed on the thickness of individual layers. Often we deal only with the thin magnetic layers on a non-magnetic substrate. When the optical path length of the magnetic layer is much lower than the wavelength of the incident light, the ultra-thin-limit approximation is valid. Mathematically this condition is written as $2\pi \sum d_m \|n_m\| \ll \lambda$. The derivation of the Jones matrix of a sample in an ultra-thin limit is discussed for example in [60]. The derivation is carried out from the matrix product $\hat{\mathbf{A}}_i^{-1} \prod_{m=1}^N (\hat{\mathbf{A}}_m \mathbf{P}_m \hat{\mathbf{A}}_m^{-1}) \hat{\mathbf{A}}_f$ in an ultra-thin-film-approximation. The reflection components derived from the approach are [28]

$$r_{ss} = \frac{n_i \cos \alpha_i - n_f \cos \alpha_f}{n_i \cos \alpha_i + n_f \cos \alpha_f}, \quad (3.86)$$

$$r_{pp} = \frac{n_f \cos \alpha_i - n_i \cos \alpha_f}{n_f \cos \alpha_i + n_i \cos \alpha_f}, \quad (3.87)$$

$$r_{ps} = -\frac{4\pi}{\lambda} \frac{n_i \cos \alpha_i \left(\cos \alpha_f \sum_m d_m n_m^2 Q_z^m - n_f n_i \sin \alpha_i \sum_m d_m Q_y^m \right)}{(n_i \cos \alpha_i + n_f \cos \alpha_f)(n_f \cos \alpha_i + n_i \cos \alpha_f)}, \quad (3.88)$$

$$r_{sp} = -\frac{4\pi}{\lambda} \frac{n_i \cos \alpha_i \left(\cos \alpha_f \sum_m d_m n_m^2 Q_z^m + n_f n_i \sin \alpha_i \sum_m d_m Q_y^m \right)}{(n_i \cos \alpha_i + n_f \cos \alpha_f)(n_f \cos \alpha_i + n_i \cos \alpha_f)}. \quad (3.89)$$

Where n_i, α_i are the index of refraction and the incident angle in the nonmagnetic medium 1, n_f, α_f are the index of refraction and the incident angle for the substrate and d_m, n_m are the thicknesses of the m -th layer with n_m its refractive index. The α_f is obtained from Snell's law $n_i \sin \alpha_i = n_f \sin \alpha_f$. Equations (3.88) and (3.89) exhibit additivity law for all magnetic layers whereas non-magnetic thin spacers do not contribute to the optical response. Another property that has already been discussed is the odd/even dependence of the magneto-optical response for the longitudinal/polar magnetization. This can be seen from the $\cos \alpha_f$ in front of a polar term and from the $\sin \alpha_i$ in front of a longitudinal term. Also we can see, that the longitudinal Kerr effect is n_m independent and that for the typical medium 1 being air ($n_i = 1$) we see that the magnitude of the polar Kerr effect is $|n_m^2|/|n_f|$ higher than the magnitude of the longitudinal Kerr effect.

3.2.3 Summary of the theoretical section

In summary we used an illustrative Lorentz model to arrive to the diagonally asymmetric form of the permittivity tensor (Eq. (3.20)) in section 3.1. In section 3.2 we

showed that in the magnetized matter any wave can be described as a superposition of four proper-modes having a form of left and right handed circular polarizations. The indices of refraction for the LCP and RCP waves are given by Eq. (3.55). For small values of \mathbf{Q} the difference in the index of refraction is linear in $\mathbf{Q} \cdot \mathbf{e}_k$. The index of refraction and the proper modes are then used in the derivation of the optical response of the three-layer, two-boundary system. The obtained transfer matrix (3.71) transferring an EM wave from one medium to another. The transfer matrix might be used for magnetic as well non-magnetic media. The propagation in the layer is described by the propagation matrix $\hat{\mathbf{D}}$. With the help of those two matrices the result for a three-layer, two-boundary problem can be extended to arbitrary number of layers. The results of the presented formalism corresponds well with the measurement we performed. Fitting the model to our data allowed us to estimate effective optical constants of the Permalloy layer. Comparing the data obtained for the longitudinal and polar magnetization confirmed the result of the analysis of the eigen-modes given by Eq. (3.55). We see that the resulting curves for the longitudinal magnetization are odd in the angle of incidence while for the polar magnetization the dependence is an even in the angle of incidence. This is direct consequence of Eq. (3.55) showing two different refractive indices for the LCP and RCP waves. To phenomenologically show the effect of the different refractive indices for the LCP and RCP wave, we show in the Appendix B (Section 6) how the difference in the refractive indices gives a rise to the rotation of the polarization and also to the ellipticity of the resulting elliptical polarization. First we show the effect of the different real part of the refractive index that is inserted in the left and right circular waves [Eq. (A.11)]. With the help of trigonometric identities we obtained a result (A.14) showing that the rotation of the polarization is linear in the difference between two modal refractive indices n^+ and n^- . Consequently we performed a similar calculation where we assumed different indices of absorption (imaginary part of the complex refractive index) for the LCP and RCP waves. The result attributed the ellipticity of the resulting polarization to the difference in the indices of absorption (Eq. (A.19)). This result is within a good accuracy also seen when we take into account Eq. (3.55) and equations (3.88), (3.89). It shows that the imaginary part of vector \mathbf{Q} induces the Kerr ellipticity and that the Kerr rotation stems from the real part of \mathbf{Q} . The knowledge of the origin of the Kerr rotation and the Kerr ellipticity helps to track the origin of unwanted effects and to actually get rid of them.

4. VECTORIAL KERR MAGNETOMETRY

Understanding the of the magnetization processes in complex magnetic structures has been targeted by many authors ever since the domain structure was observed [34, 35]. Since the first investigated systems did not have any of its dimension below few microns, the first observed patterns have been too complex to be described analytically [78, 79] and the experimental methods back then did not offer experimentalists with much information. In the last decades, the growing interest in magnetic nanostructures with nontrivial magnetic ordering: high density data recording, magnetic logical elements and magnetic RAM, has stimulated an interest in knowing vector response of the magnetization vector to the external magnetic field in a static and dynamic regime.

Even though the Kerr effect has the capability to measure the whole vector of magnetization as was outlined in the previous section, in order to do so, we need to deterministically change the propagation vector \mathbf{k} of the incident light. Such a property of the optical setup is often hard to accomplish. The Kerr angles are small and the requirements on the stability of the optical setup causes the Kerr magnetometers to be designed as rigid as possible. Thus they often provide the information on the magnetization under the fixed angle which (as shown in Chapter 3) generally results in the measurement of the mix of the Kerr effects. This makes the data interpretation hard to carry out and it can even be misleading. Knowing the vectorial information or even to know the evolution of the vector of magnetization in the external magnetic field strongly contributes to the characterization of the switching processes and might reveal some interesting phenomena.

The measurement of the vector of magnetization has been targeted by many authors during the years [22, 80–92]. One possibility is to use goniometric setup with variable angle of incidence often used in the ellipsometry, but in this way only two components (longitudinal and polar components) of the magnetization may be measured. To measure the transverse component, the sample needs to be rotated together with the magnetic field source which is inconvenient and often hard to carry out. Additionally it causes systematic errors again leading to the problematic data interpretation. In 1990 Florczak et al. managed to separate two in-plane components by rotating the analyzer and exploiting the fact, that the transversal Kerr effect affects only the intensity of the light, not polarization [80]. Many other interesting approaches appeared, but most of them require either rotation of a sample/magnet [88, 90, 91, 93], other variation in optical arrangements [22, 85, 87] or the methods are not viable for probing magnetism at nanoscale [82, 83].

In this work, we present a scanning Kerr magnetometer setup that is able to probe

the whole magnetization vector with diffraction limited resolution down to $\Delta = 500$ nm. In the process of recovering the all components of \mathbf{M} we need four separate measurements, where no rotation of optics, sample or magnet is needed. In addition, the scanning capability of the setup allows mapping the magnetization in whole 4π space. The possibility to separate the individual components of magnetization vector comes directly from the results derived in chapter 3. Our approach exploits the basic property of the dot product in Eq. (3.55). The approach is originally based on the work by Ding et al. In his work from 2000 [86] he used the basic symmetries of the polar and the longitudinal Kerr effect to probe two components of magnetization and in 2001 [87] he extended his approach to probe the whole magnetization vector. In his experiments he used the method presented in the equations (3.83)-(3.85).

In our work we use a similar approach whenever the IP and OOP effects are present at the same time. However, in majority of samples we study only the in-plane components of magnetization that prevails¹. Without the presence of out-of-plane magnetization only two measurements are necessary to fully characterize the in-plane magnetization vector. This still requires great variability in the optical part of the Kerr magnetometer while maintaining the stability of the signal.

4.1 Apparatus for scanning magneto-optical Kerr microscopy

In the rest of this chapter the optical and mechanical design and the electronics of our newly developed scanning Kerr magnetometer called MIRANDA.

We start with the quantification of measured signal by the means of the Jones formalism (introduction in section 2.3). We use the matrix of the sample (see (2.25)) and other optical components (see Tab. 2.1) to attribute a complex angle of Kerr rotation Φ_s to a measured sum and differential intensity on the matched pair of photodiodes. Afterwards the schematic of the Kerr magnetometer is presented followed by the details on individual sub-systems (e.g. detector).

4.1.1 Magneto-optical setup - differential intensity detection

Herein we present an optical model of the optical setup described by the means of the Jones formalism. We show how the magneto-optical observables can be derived in a very simple way in the form suitable for the actual measurement.

The effect of the sample for various relative orientations of \mathbf{M} and \mathbf{k} has been presented in Tab. 2.2. All the derivations are carried out for the s polarized beam. For the s-polarized beam the sign of the off diagonal coefficients for the polar and the longitudinal Kerr effects is the same (see $\varphi \neq 0$ case in Tab. 2.2), so the results obtained for the s polarized beam and the matrix describing the polar Kerr effect will also be applicable to the longitudinal case.

¹ The domain walls for ultra-thin layers are often out-of-plane, but they are far below the resolution limit of our Kerr magnetometer.

We start with the optical scheme presented in Fig. 4.1. Here an, originally s

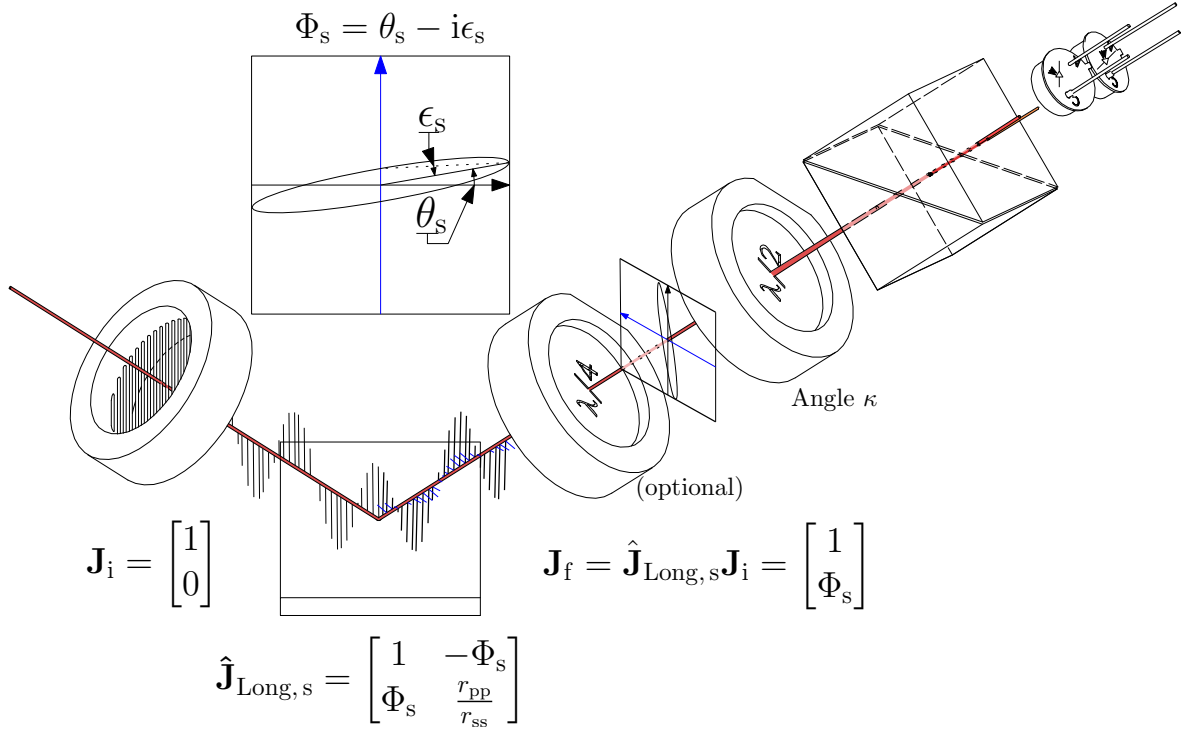


Fig. 4.1: Schematic of the reflection of the s polarized wave on the sample with longitudinal magnetization. The anisotropic sample introduces p polarized component to the originally s polarized wave. This altered wave then passes the quarter wave plate (fast axis in s direction) which basically converts the real part of the complex Kerr rotation Φ_s to the imaginary part and vice versa. The Half Wave Plate rotated by the angle κ serves as a simple mode coupler, allowing us to deterministically cancel those (constant) polarization effects that are not caused by the magneto-optical response of the sample. Last optical element is the Wollaston prism set at 45° . With the angle of the HWP $\kappa = 0$ and for the isotropic sample ($\Phi_s = 0$) it will separate the incident wave into two equivalent waves. With non-vanishing Φ_s the intensity difference of those two waves is linear in θ_s (or in ϵ_s when the QWP is used).

polarized wave is reflected by the sample, which introduces a non-zero p component of the reflected electric field. After reflection, the altered wave passes through the quarter-wave-plate (QWP, optional). This phase retarder is used as a switch between measuring Kerr rotation (no QWP) and Kerr ellipticity (with QWP). The following element, half-wave-plate (HWP) serves purely as an s-p intensity converter which allows us to balance some constant polarization effects of the apparatus. Contrary to the fixed angle of QWP, HWP is rotated by angle κ . After the wave is transmitted through the HWP it continues to the Wollaston prism rotated by 45° . This prism serves as a polarizing beam-splitter effectively separating s and p polarized beams. The Wollaston prism is rotated at angle 45° thus for the isotropic sample the measured intensities for s and p polarized waves are the same. To start with the theoretical description let us

write down the model of the presented optical scheme in Fig. 4.1.

$$\begin{aligned} \mathbf{J}_{\pm} &= \hat{\mathbf{J}}_{\text{W}} \hat{\mathbf{J}}_{\text{HWP}}(\kappa) \hat{\mathbf{J}}_{\text{QWP}} \hat{\mathbf{J}}_{\text{Long},s} \mathbf{J}_s \\ &= \begin{bmatrix} 1 & \pm 1 \\ \pm 1 & 1 \end{bmatrix} \begin{bmatrix} 1 & 2\kappa \\ 2\kappa & -1 \end{bmatrix} \begin{bmatrix} 1 & 0 \\ 0 & i^p \end{bmatrix} \begin{bmatrix} 1 & -\Phi_s \\ \Phi_s & \frac{r_{pp}}{r_{ss}} \end{bmatrix} \begin{bmatrix} 1 \\ 0 \end{bmatrix}. \end{aligned} \quad (4.1)$$

The second matrix stands for the HWP rotated by the angle κ . This form was obtained by the general rotation (Tab. 2.1) considering only small angles κ . The following matrix represents the quarter-wave-plate. Optionality of using the QWP is given by the superscript p . By choosing p to be 1 (or 0) we can easily model if the QWP is used (or not). Going through the basic algebra we can expand Eq. (4.1) to the form of a single final vector \mathbf{J}_{\pm}

$$\mathbf{J}_{\pm} = \begin{bmatrix} 1 \pm 2\kappa + (2\kappa \mp 1)i^p \Phi_s \\ \pm 1 + 2\kappa + (\pm 2\kappa - 1)i^p \Phi_s \end{bmatrix}. \quad (4.2)$$

Now we have to get the intensity of both + and - beams via Eq. (2.8) where we omit the constant in front of the expression. After few algebraic steps we obtain

$$I_{\pm} = \mathbf{J}_{\pm}^{\dagger} \mathbf{J}_{\pm} = 8 \left[\overline{\Phi}_s \left(\kappa \mp \frac{1}{2} \right) (-i)^p \pm \kappa + \frac{1}{2} \right] \left[\Phi_s \left(\kappa \mp \frac{1}{2} \right) i^p \pm \kappa + \frac{1}{2} \right]. \quad (4.3)$$

This equation still does not give much insight to the problem. In order to get a simple expression allowing us to quantify the Kerr rotation θ_s or Kerr ellipticity ϵ_s let us do the difference I_{diff} and sum I_{sum} of the two resulting intensities given by Eq. (4.3). At this point, we use the important definition from Eq. (2.28). Instead of writing Φ_s we use the Kerr rotation and Kerr ellipticity written as $\Phi_s = \theta_s - i\epsilon_s$.

We start with the case when we do not use the quarter-wave-plate in our setup ($p = 0$). Then I_{diff} divided by I_{sum} yields

$$\frac{I_{\text{diff}}}{I_{\text{sum}}} = \frac{2(4\kappa^2\theta_s - 2\kappa\theta_s^2 - 2\kappa\epsilon_s^2 + 2\kappa - \theta_s)}{(4\kappa^2 + 1)(\theta_s^2 + \epsilon_s^2 + 1)}. \quad (4.4)$$

Similar result might be obtained for $p = 1$

$$\frac{I_{\text{diff}}}{I_{\text{sum}}} = \frac{2(4\kappa^2\epsilon_s - 2\kappa\theta_s^2 - 2\kappa\epsilon_s^2 + 2\kappa - \epsilon_s)}{(4\kappa^2 + 1)(\theta_s^2 + \epsilon_s^2 + 1)}. \quad (4.5)$$

In the last step we use the small angle approximation, hence neglect all the non-linear terms in Eq. (4.4) and Eq. (4.5). In doing so we obtain

$$p = 0 \rightarrow -\frac{I_{\text{diff}}}{2I_{\text{sum}}} = \theta_s - 2\kappa, \quad p = 1 \rightarrow -\frac{I_{\text{diff}}}{2I_{\text{sum}}} = \epsilon_s - 2\kappa. \quad (4.6)$$

This result is used throughout the entire work. It allows us to quantify the Kerr rotation (or the ellipticity) only with the knowledge of the sum and differential signal on the pair of photodiodes. Angle κ of the HWP is used to cancel the (constant) polarization effects that might occur in the optical setup (e.g. strained optics [52]) or the HWP can be used to cancel some effects caused by the relative misalignment (or rotation)

of the optical elements. The use of the Wollaston prism and the pair of photodiodes allows us to easily quantify the Kerr rotation and the Kerr ellipticity. This approach outperforms other methods used for measuring the magneto-optical Kerr effect in the simplicity, speed and ease of quantification of the measured signals. Short summary of other approaches for measurement of MO effects is given in [48].

4.2 Scanning Kerr magnetometer design

One of the main parts of the work on this thesis is designing, installation and testing of a MIRANDA scanning vectorial Kerr magnetometer at IPE BUT. The process of a design of the Kerr magnetometer combines the experience with the Kerr magnetometer design we already had with the solutions found in the relevant literature. In the previous work, [94] we designed and tested μ -Kerr magnetometer with the laser spot $\approx 2 \mu\text{m}$. We successfully measured a hysteresis loop from a single $1 \mu\text{m}$ disk (radius 500 nm , thickness 30 nm), but despite the effort, the successful measurement has never been repeated. The analysis of the setup performance revealed the detector to be the most problematic part. Employment of the method presented in section 4.1.1 requires the two separated s and p beams to be equal in the intensity. The original design of the detector was done by Uhlíř [95] and the detector did not allow to compensate the relative movement of optical elements and the sample. This gave a rise to the optical misalignment of the two beams with respect to the photodiodes often leading to the dis-interpretation of the unbalanced intensity and also to the enormous noise level. In the former approach the focusing element was an aspheric lens ($f' = 50 \text{ mm}$) and the collecting element was a converging lens with the same focal length. This combinations proved to be very hard to align especially for the samples with curved surface.

In the current design we use a microscope objective where the incident laser beam is deterministically deviated from the optical axis of the objective. This deviation creates an in-plane component of \mathbf{k} thus it allows to also probe the in-plane components of magnetization ($\Phi_s \propto \mathbf{k} \cdot \mathbf{M}$). In the linear regime the increase of in-plane component of vector \mathbf{k} increases also the in-plane signal. The maximum angle of incidence is given by the Numerical Aperture (NA) of the used objective

$$NA = n_e \sin \alpha_1 \rightarrow \alpha_1 = \sin^{-1} \left(\frac{NA}{n_e} \right), \quad (4.7)$$

where n_e is the index of refraction of the environment between the objective and a sample and α_1 is the incidence angle. For $n_e = 1$, the numeric aperture directly gives the magnitude of the dot product $\frac{\mathbf{k}}{|\mathbf{k}|} \cdot \frac{\mathbf{M}_{\text{IP}}}{|\mathbf{M}_{\text{IP}}|}$ that corresponds with the magnitude of the Kerr rotation/ellipticity induced by the in-plane magnetization. This behavior can be also clearly seen from the calculated curves in Fig. 3.3.

Inducing the in-plane component of \mathbf{k} requires the entrance aperture of the objective to be only partially illuminated. If the entrance aperture is fully illuminated, the symmetry of the illumination leads to zero integral in-plane signal. We use a 15 mW

He-Ne laser (LASOS HNL150L-EC) with the wavelength $\lambda = 632.8 \text{ nm}$. According to the data-sheet the $1/e^2$ waist is $w_0 = 0.68 \text{ mm}$ and the beam divergence is 1.2 mrad . It follows from the Gaussian optics that for a free space propagation of 30 cm such a small beam divergence does not affect the beam diameter present at the entrance aperture of the objective [68]. A small beam waist in combination with the diameter of the entrance aperture (1.4 mm), ensures that we are able to effectively break the illumination symmetry without losing intensity by cropping the beam on the objective entrance aperture. The figure 4.2 shows how the deviation of the laser beam at the entrance aperture tilts the laser beam in the sample plane. In the picture we combined a schematic sketch with actual pictures of the tilted beam to clearly demonstrate the mentioned effect.

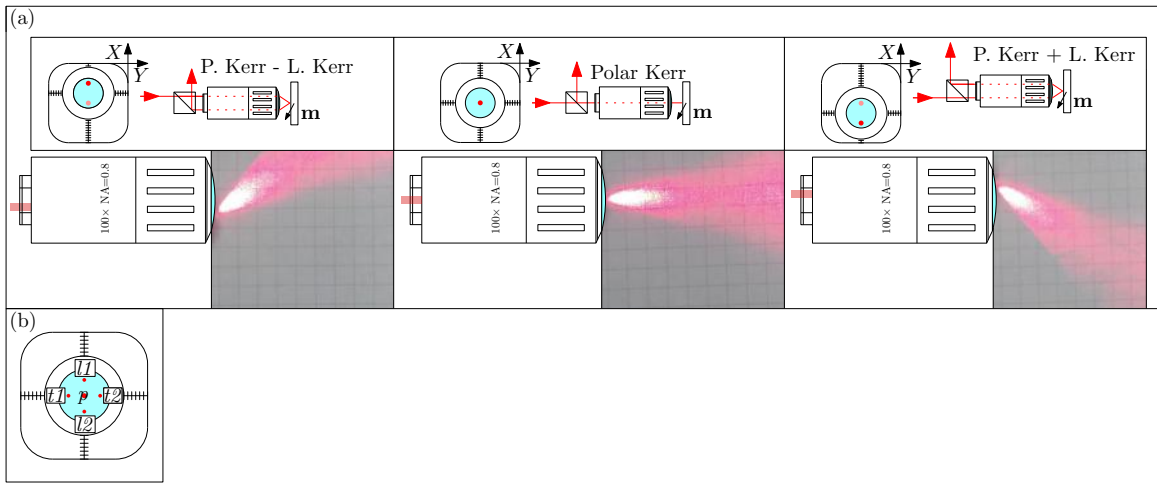


Fig. 4.2: Picture (a) schematically shows how the beam displacement in the entrance aperture affects the declination angle of the resulting beam. From the insets above actual photos we see what magnetization components would be in the shown configuration detected. The maximum angle for used objective is from Eq. (4.7) equal to 53° . In (b) we define the incident laser positions where l and t stands for the detected longitudinal and transversal magnetization respectively. Position p defines the axially symmetric illumination thus it only probes the OOP component.

Indisputable asset of employing the microscope objective is that for an aberration corrected PLAN objective the optical resolution is given solely by the diffraction limit:

$$\Delta = 0.61 \frac{\lambda}{NA}, \quad (4.8)$$

here Δ is a distance of two objects on which they can be clearly distinguished. For the microscope objectives we use with $NA = 0.8$ and $NA = 0.95$ the resolution limit gives $\Delta = 483 \text{ nm}$ and $\Delta = 406 \text{ nm}$ respectively. In a measurement the magneto-optical response of the objects much smaller than the optical resolution can be detected, however for the quantification of the Kerr angles with Eq. (4.6) we have to take into account that whereas the differential intensity is induced solely by the magnetic particle the sum intensity is given also by the surrounding substrate. Correcting for this effect would require the knowledge of the spot spatial intensity distribution and

also the values of the reflectivity for both the substrate and the magnetic particle [94]. In results presented in chapter 5 we distinguish whether the data are corrected or not. If not mentioned no correction has been made.

We showed how the laser beam placement on the input aperture affects the angle of the laser beam leaving the objective. The mechanism allowing to accurately vary the declination angle is shown in the picture 4.3 together with the measurement of the resulting laser beam angle α as a function of the relative position X of the incident laser beam and the objective.

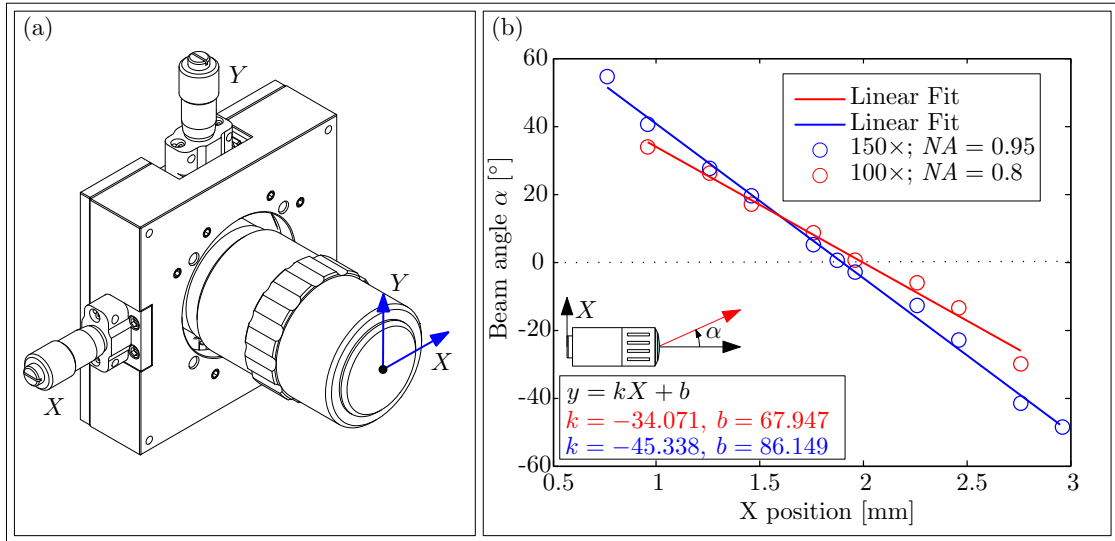


Fig. 4.3: (a) CAD model of microscope objective mounted in a 2D translation stage is shown. With the stage the objective can be repeatably positioned with the precision of approx. $5\mu\text{m}$. (b) Graph of the beam angle obtained from the measurements shown in Fig. 4.2. From the repeated measurements we estimate the maximal error of measuring the beam angle to be 1.5° which does not explain the difference in measured data for $\alpha = 0$. From the measurement we estimated the maximum angle for 100 \times objective to be 50° (from $NA = 0.8$ we get 53°). For the 150 \times we measured 71° (from $NA = 0.95$ we get 71.8°).

We use a 2D translation optical mount with precision $(5 \pm 2.5)\mu\text{m}$ which gives the incident angle setting precision $0^\circ 0' 0.61''$ for the 100 \times objective and $0^\circ 0' 0.82''$ for the 150 \times objective. Despite the great repeatability of the angle setting we found that the 2D translation stage has a non-negligible cross talk between x and y axes that does not show any deterministic behavior. The cross-talk magnitude can be neglected when measuring two in-plane components but when separating a small out-of-plane signal from large in-plane signal the X , Y setting must be precalibrated on known structures.

The used 2D translation stage allows $\pm 2.5\text{mm}$ movement in both directions hence it allows to position the laser beam in a whole entrance aperture with or without the cropping the laser beam. The solution of using a translation post to vary the beam angle is precise (for IP structures), deterministic and can be easily automatized since the micrometer drives can be interchanged with servo motors, i.e. full control from the computer is possible. Selecting the probed magnetization direction easily from the

computer is a particular advantage not found in other setups [22, 85, 90].

We schematically show how we are able, by breaking the symmetry of the illumination, to probe all the magnetization components with a fairly simple mechanism. In figure 4.4 a simplified optical and electronics scheme is shown giving an idea what lies behind the results presented in chapter 5. The whole setup involves a lot of PC-HardWare-PC communication. In the setup we control the sample-stage drivers, camera, DAQ card, wave-form generator, optical detector and also the teslameter. Whole system can be programmed highly automatic to probe the various properties of the samples. The whole setup is controlled by the software developed especially for our scanning Kerr magnetometer in the LabView interface. Up to now 170 programs and subroutines have been developed to fully exploit the possibilities of our Kerr setup. In the presented thesis the developed software description is left out but we would like to stress that the software development was and still is one of major time-consuming mechanisms behind the work on the development of the Kerr setup.

The scheme 4.4 can be divided to the optical part and to the supporting electronics while the mechanics involved were not stressed out. In the following section we show, with some details, selected components from the mechanical and the electronics part. Details on the majority of optical elements can be found in the appendix of the previous work done on the Kerr development [94].

4.2.1 Mechanical design

The whole setup has been designed mainly with the optical and optomechanical components from Thorlabs, Inc. combined with parts fabricated in the mechanical workshop at IPE BUT. The Cage system by Thorlabs allows the whole setup to be built and maintained in one easy-to-use framework. The basic idea behind the Thorlabs Cage system is decreasing the optical degrees of freedom to a minimum, hence it makes axial optical alignment much easier than with free-standing post-mounted optical components. For the Kerr magnetometry where the magneto-optical response is small, the alignment and the stability of the setup is crucial. The optical elements in cage-system are mounted on the passively damped posts which proved to be stable enough for long-time (tens of minutes) measurements. The design of the Kerr magnetometer was initially done in the 3D software Autodesk Inventor allowing us to model the whole setup with its movements and stresses so in this way we actively avoided many problems and unexpected obstacles in the construction process. The rendered picture of the setup is shown in Fig. 4.5. The mechanical design consist of three individual parts: the illumination part, the sample stage and the detector. The damped posts holding the whole system are positioned with respect to the weight load and also to the dynamic properties of the optical table. We performed reference vibration measurements of the loaded optical table to further improve the stability of the setup. The home-made optical table is mounted on the four air-damped active-leveling vibration isolating supports that proved to be one of the key elements in the mechanical stability.

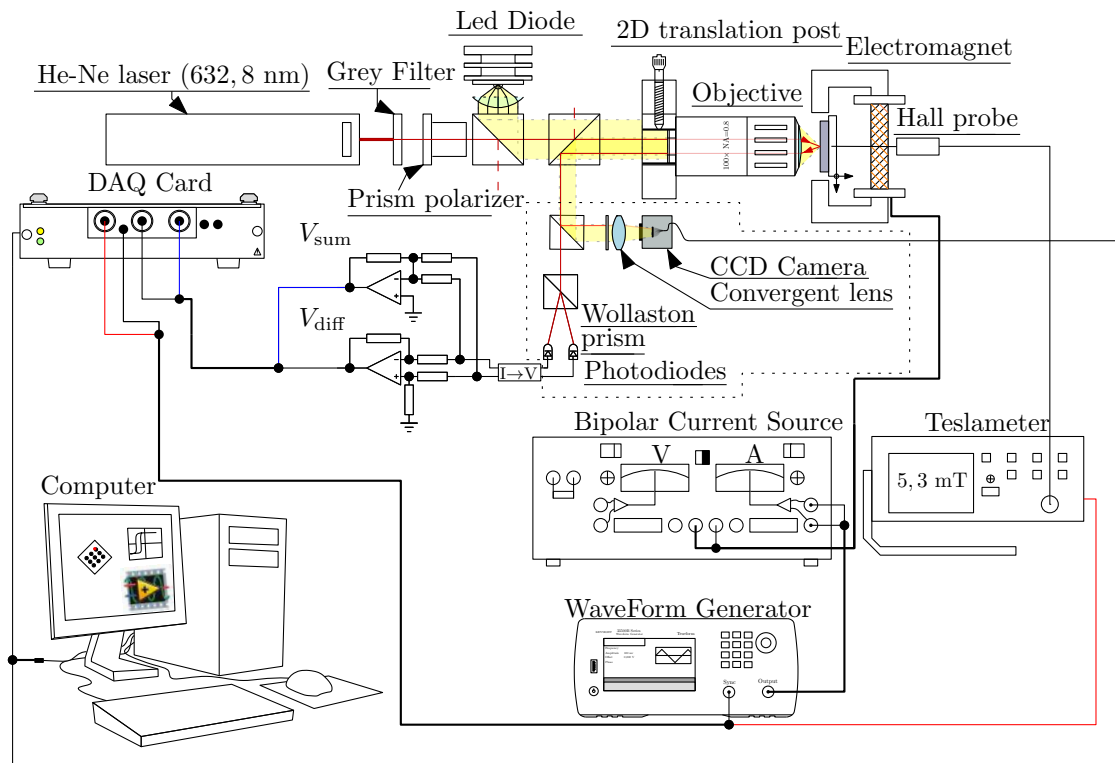


Fig. 4.4: The figure showing the optical beam path and the electronics used in the experiment. Starting with the optical part: Laser has its original polarization plane at 45° thus it allows the p/s polarization to be easily altered. The laser beam power (≈ 15 mW) is attenuated to 1% of its optical power by an absorbing filters. Then the laser beam polarization is selected by a prism polarizer. The white light for the imaging is added on the non-polarizing beam-splitter with 3:7 transmission/reflection ratio. After passing the second beam-splitter (again 3:7) it passes through the microscope objective and reflects on the sample mounted on the x, y, z piezo stage. Reflected beam goes to the detector (delimited by the dotted line) and in the detector the laser beam goes through the last beam-splitter (9:1) allowing a real-time observation by the web-camera. The major part of the intensity is passed to the Wollaston prism separating the s and p polarized beams onto the matched pair of photodiodes. The current from photodiodes is converted via the trans-impedance amplifiers to voltage and then the other amplifier provides the sum and the difference of the two input voltages. The difference is amplified and both signals are sent to the ADC DAQ card. When measuring the hysteresis cycles, the card acquisition is synchronized with the wave-form generator hence it allows the employment of some basic demodulation techniques. The magnetic field is induced by an electromagnet driven by a voltage to current converter Kepco BOP. The actual magnetic field is measured by the Hall probe and the signal is amplified and sent to ADC converted by the teslameter F.W. Bell 6010.

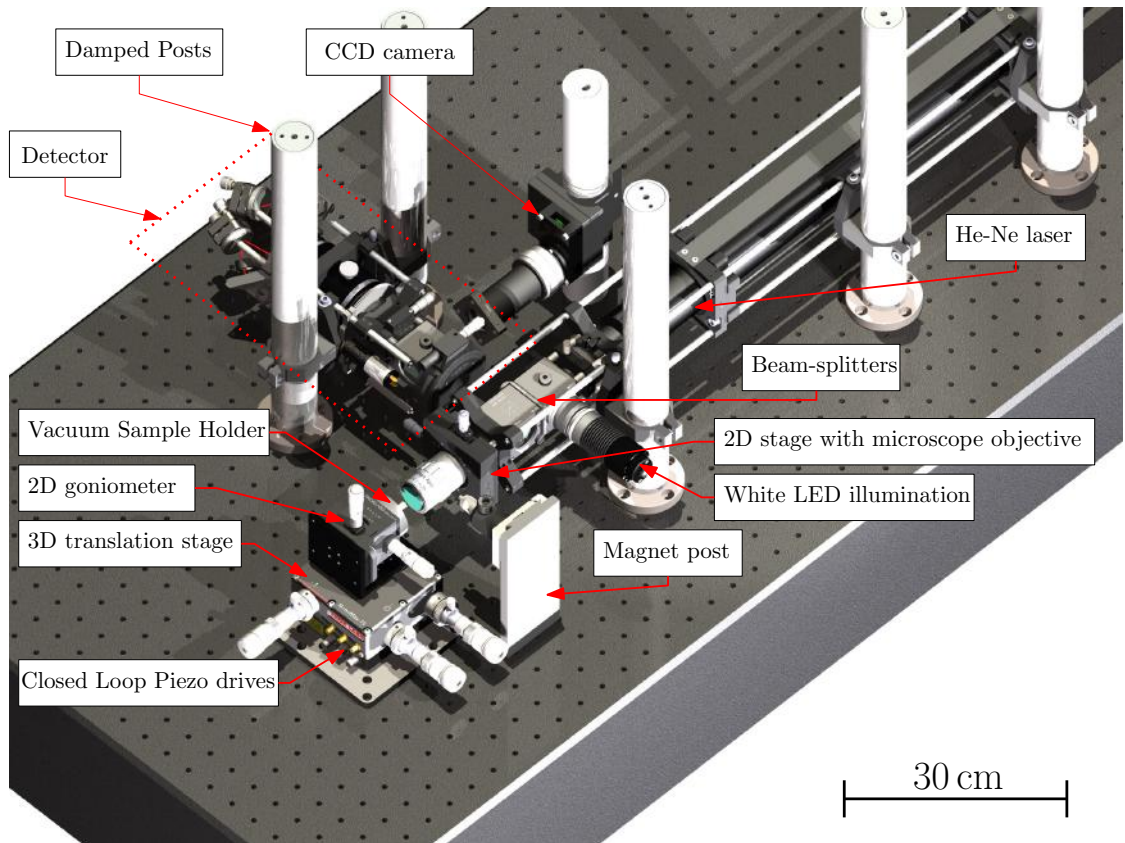


Fig. 4.5: 3D model of the experimental setup. The illumination part consist of the He-Ne laser, beam-splitters, white LED and the microscope objective mounted in the 2D stage. The sample stage consists of the 2D goniometer and a vacuum sample holder. In the vicinity of the sample stage is a magnet post allowing a coarse adjustment of an electromagnet. The detector is stabilized by the pair of damped posts. The details about the detector are given in a section dedicated to the detector description. As a part of the detector system the CCD camera is implemented in the setup allowing live observation of the sample.

The sample is mounted by a home-made vacuum system on the 3D translation stage (MAX301/M) with 5 mm translation in all three axis. Additionally, the system incorporates closed loop piezo-electric actuators with $20\mu\text{m}$ translation range. The stage can be driven in both closed loop and open loop regime. For every piezo actuator we have a pair of controllers. They consist from a strain-gauge reader providing the position feedback with nm precision and the piezo driver supplying the voltage to the actuator. The two controllers are connected by the analog feedback lines enabling the strain-gauge reader to provide a feedback voltage to the piezo controller thus it allows what is known as a closed loop operation. This closed loop operation cancels the hysteresis effect of the piezo actuators on the other hand it lowers the speed performance of the actuator. In the open loop regime scanning at tens of Hertz is possible in contrast to the closed loop regime, where the highest frequency we achieved was 0.3 Hz. The closed loop regime uses the strain-gauge feedback sensors allowing a nanometer resolution to be achieved. The position settling in the closed-loop regime has a time-exponential character with time constant $\tau \approx 250$ ms. The performance can be further adjusted by selecting the PID (Proportional-Integral-Derivative) constants. The strain-gauge reader has a proportional ($0 - 20\mu\text{m} \rightarrow 0 - 5\text{V}$) voltage output working up to 10 kHz that can be used as a precise position monitor. The strain-reader-PC communication is also used but the communication bandwidth of approx. 4 Hz is insufficient for the scanning so the position-voltage proportional output is monitored by the AD converter. The scanning is implemented as shown in the diagram 4.6. The

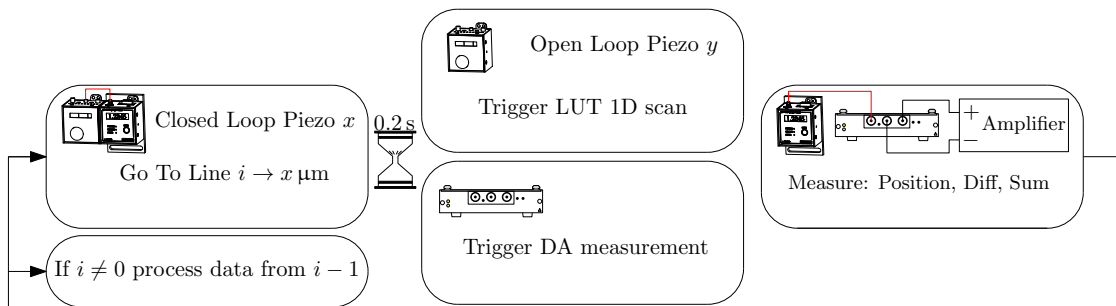


Fig. 4.6: Flow diagram showing the implemented scanning in the x, y directions. One piezo-strain-gauge pair in the closed loop and the other in the open loop regime. The choice of scanning direction affects the resulting image for the samples with topography. The effect of the scanning direction will be discussed in the experimental chapter.

piezo driver in the open loop² regime allows a 512 value LUT (look up table) waveform to be uploaded to its memory and triggered by a computer. The combination of a LUT waveform, proportional strain-gauge reader output and one piezo in a closed loop regime we were able to achieve scanning frequencies up to 10 Hz. For regular operation we limited the scanning frequency to 1.9 Hz in order to avoid operation close to the resonance of the piezo stage.

² In a closed loop (even if possible) the LUT waveforms exhibits various faults and problems.

After the reflection on the sample the light beam passes to the detector unit. A new detector has been developed after having a serious noise problems with the former solution. The mechanical design, together with the electronics involved is shown in Fig. 4.7. The optical scheme is the the same as in the theoretical model from Fig. 4.1. The

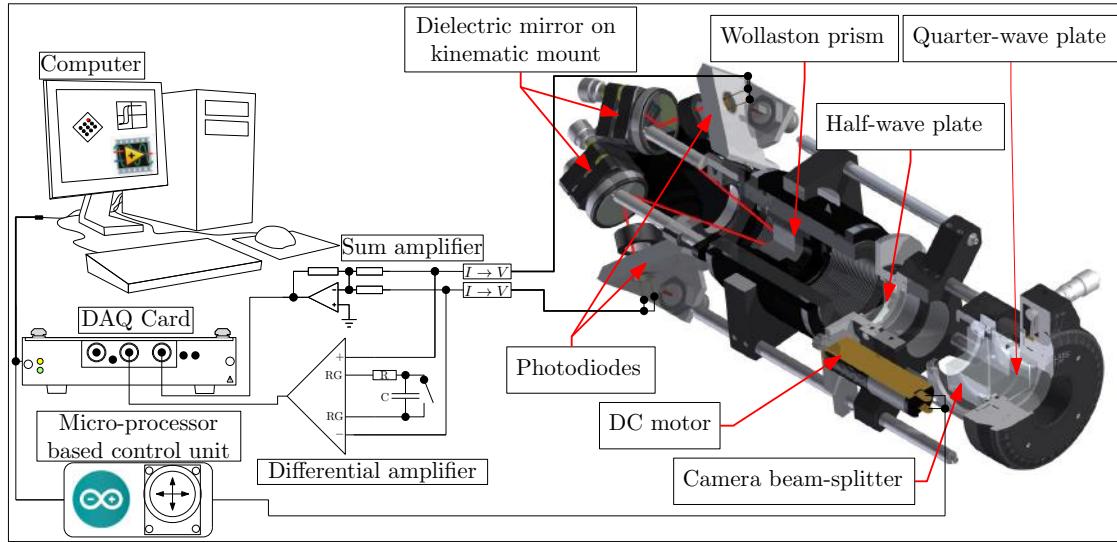


Fig. 4.7: A connection diagram together with a 3D model of the detector. The optical scheme is the same as in Fig. 4.1. The signal from the photodiodes is converted by a selectable-gain trans-impedance amplifiers to voltage. Home-made amplifier uses one operational-amplifier and one instrumentation-amplifier to obtain the sum signal and the differential signal, respectively. The instrumentation amplifier allows to amplify only the frequency components of signal that are relevant to the measurement. Both signals are measured by DAQ 16-bit card.

light beam passes through the removable quarter-wave plate, then it passes through the beam-splitting cube and subsequently it goes through the half-wave plate mounted in the rotational optical mount. The rotation is controlled by a home-made rotational mount driven by a DC motor. The rotation and the speed of rotation is controlled either manually by a joystick or it is controlled from a computer. When controlled by the computer it can automatically rotate the QWP to minimize the average differential intensity. The amplifier incorporates an electronic circuit giving a sum and also the differential voltage of the two signals. The unique and fairly simple design of the differential amplifier is based on the instrumentation amplifier THAT1510. The gain of the amplifier is tuned by the feedback resistor interconnecting two RG ports. The resistor value-gain dependence follows [96]:

$$A_V = 1 + \frac{10 \text{ k}\Omega}{R_G}. \quad (4.9)$$

Here A_V is a amplification gain and R_G is a feedback impedance. For the RC element in series the impedance is given by

$$R_G = R + \frac{1}{2\pi i f_i C}. \quad (4.10)$$

With f_i being the frequency of the i -th harmonics of the measured signal. Combining the equations (4.9) and (4.10) we see the different gain for the individual components of the Fourier series representing the measured signal. For DC signal R_G diverges resulting in the unity gain. By tuning the RC constant of the circuit we can amplify the AC signal with the selectable gain 10/100/1000/10000 while leaving the DC signal unamplified. The capacitor is used only for the hysteresis curve measurements where the expected signal is at the excitation frequency and its higher harmonics. When measuring at $f_0 = 42.231$ Hz with gain $A_V = 100$ and capacitor 22 mF the phase distortion of the first harmonics is 0.097° and the amplitude distortion is approx. 10^{-6} . The capacitor in the circuit thus does not alter the signal of the interest, but the slowly varying DC offset is effectively canceled with time constant of 2.2 s. The selection of the exciting frequency is not random. It is selected on the basis of measuring the differential signal V_{diff} on a magnetic layer and performing a FFT (Fast-Fourier-transform) analysis of the obtained signal. The frequency $f_0 = 42.231$ Hz and its harmonics has the lowest spectral noise power hence the measurement with this particular fundamental frequency has the lowest noise contribution. The noise level is further effectively lowered by averaging the signal in time or over whole hysteresis cycles. Averaging the signal over the complete external fields cycle can be used only when the evolution of the magnetization in the external field cycle is non-stochastic i.e. it does not display randomness. Another method of significantly decreasing the noise level while removing the DC drift is with the use of demodulation techniques.

In the magneto-optical measurements one of the most common technique is the lock-in demodulation of the signal modulated by elasto-optic modulation [97], Pockel's cell [31] or by the Faraday's effect [48]. These techniques allow to quantify the Kerr rotation/ellipticity in static magnetic field. For such a system a full hysteresis cycle is obtained at the rate approx. 1 Hz [21]. For hysteresis curve measurement we use a different approach. We suppose the MO signal to be excited only by the external magnetic field (at frequency f_0). In the quasi-static regime the magneto-optical response is then expected only at the fundamental carrying frequency f_0 and its higher harmonics. This strict presumption is justified if we compare the characteristic time of the change of the external magnetic field approx. ms with the specific times of the magnetization dynamics which are in the approx. ns-ps range [98]. Thus for every external magnetic field step the magnetization has a long time to settle to the energetically most suitable state.

To separate the magneto-optical response from the other contributions to the signal (e.g. mechanical vibrations, etc.) we use the process schematically shown in Fig. 4.8. For every measured magnetic field cycle (full cycle or its half-integer multiples) we perform a FFT analysis of the magnetic field cycle (measured by the Hall probe) and after binarization of the amplitude spectra we obtain so-called the FFT excitation mask. Simultaneously with the magnetic field we also measure the differential voltage V_{diff} which is directly proportional to the Kerr rotation or ellipticity (that is proportional to magnetization). Performing the FFT analysis on V_{diff} we get the frequency spectra of

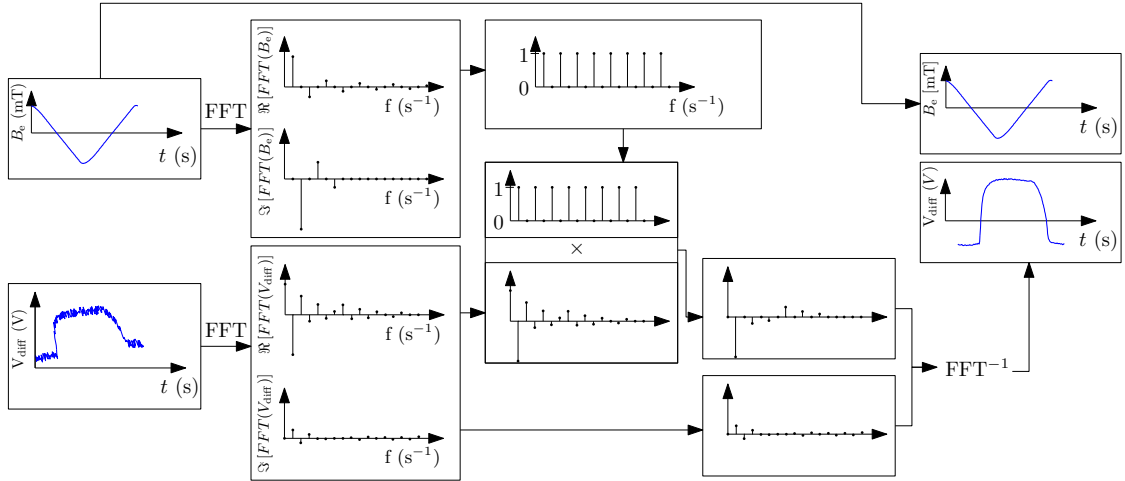


Fig. 4.8: Flow diagram showing the FFT analysis of the distorted differential voltage. The differential voltage has been taken from the measurement and we artificially added a DC offset, small slope and 10% noise voltage. The FFT transformations for the magnetic field cycle and the artificially altered differential voltage are not only schematic but depicts the real FFT analysis for the presented waveforms. In the end the differential voltage curve does not show any unprecedented behavior.

the measured signal. Multiplying the $\Re(\text{FFT}[V_{\text{diff}}])$ amplitude spectra with the FFT excitation mask we omit all the frequencies that do not come from the magneto-optical response of the sample. The $V_{\text{diff}}^{\text{FFT}^{-1}}$ signal is then obtained by performing an inverse FFT transformation.

This demodulation of the signal significantly improves the performance of the setup. It allows to record the single loop measurements without any averaging or data smoothing in a very good quality. When using a FFT filtering one has to be careful not to alter the hysteresis loop. In the real experiment it is a good manner to turn off the FFT filter and check, whether the data obtained with and without FFT filtering are equivalent. The FFT filter thus only serves to enable a higher acquisition rates because it effectively lowers the need to average the measured data.

4.2.2 Scanning Magneto-Optical Kerr modes of operation

The functionality of the developed apparatus depends on the selected mode of operation:

- **Vectorial Kerr magnetometer**

It is historically the first application of the magneto-optical Kerr effect [25]. It allows to characterize the switching process of magnetization in the external magnetic field cycle. In our implementation we position the laser spot on the magnetic-structure and we measure the magneto-optical response in the external magnetic field cycle (at $f_0 = 42.231$ Hz). In this mode the FFT filtering presented in the previous text can be effectively used to lower the need to average to data.

- **Scanning vectorial Kerr microscope**

In this mode we measure the Kerr rotation or ellipticity as a function of the position of the sample under the laser spot. With 20 μm of travel we are able to probe the vector of magnetization with the resolution approx. 500 nm. The line-scanning rates are 1.9 Hz at maximum so the acquisition of the 512 \times 512 image takes approximately 6 minutes. The implementation of the scanning Kerr microscope mode has already been shown in Fig. 4.6. The external magnetic field during a scan is a static and can be changed in-between the two scans.

- **Scanning vectorial Kerr magnetometer**

This particular mode is strictly dedicated to the non-stochastic magnetization processes in probed samples. If the magnetization behavior in a magnetic field cycle is deterministic we create a scanning grid (with a variable resolution) where for every point of the grid we measure a hysteresis loop. Both piezo-controllers are in the Closed loop regime. Loops can be averaged to increase the signal-to-noise ratio. When the software has averaged a desired number of loops it moves to the next point of the scanning grid. This mode saves for every point of the grid the hysteresis loop to the text file, the hysteresis loop image preview and the camera snapshot where the loop was taken. In the post-processing process we combine the loops measured for the different \mathbf{k} projections (different measured components of \mathbf{M}) to get the vector of magnetization for each individual grid point. The time needed for the vector map strongly depends on the desired average rates. For 50 averages the picture with 441 pixels takes approximately 45 minutes.

- **Scanning coercive field mapping mode**

This mode of operation is an extension of the scanning Kerr magnetometry mode. We use an external magnetic field oscillating at $f_0 \approx 100$ Hz. The magnitude of the field is set to saturate the sample. Instead of averaging the hysteresis loops at one position we scan the sample at 0.5 Hz while measuring the single hysteresis loops. From the measurement we save: the magnetic field for which the signal undegoes $- \rightarrow +$ change i.e. coercive field, the sum voltage i.e. reflectivity and the AC value of the Kerr ellipticity i.e. the magnitude of magnetization. The resulting image shows the spatial distribution of the coercive fields, reflectivity and magnetization with high resolution. The same information might be obtained from the Scanning vectorial Kerr magnetometer mode but the acquisition times in the scanning coercive field mapping mode are at least 10 \times lower.

In summary this chapter has presented basic concepts behind the apparatus designed and used in this thesis. In the beginning we used the Jones formalism to quantify the Kerr rotation or the Kerr ellipticity from the measured differential V_{diff} and sum V_{sum} voltages. We discussed also the cases where more than one magnetization component is present in the measurement. We also showed a procedure [Eqs. (3.84)-(3.85)] allowing to separate the MO signals originating in the different components of

the magnetization vector \mathbf{M} . The probing of different components of magnetization requires very flexible optical apparatus. We presented a very simple way how to deterministically and rigidly vary the incident angle in a cone-like space with an apex angle 60° . We also describe the mechanical design of the apparatus. We placed more detail on the possibilities and limitations of the setup. In the end of this chapter we showed various modes of operation that has been developed in order to satisfy various needs we had during the sample characterization process.

5. EXPERIMENTAL RESULTS AND DISCUSSION

Up to now we theoretically showed how the magneto-optical Kerr effect can be sensitive to individual components of magnetization and we presented some details on the setup that has been developed especially for the vectorial magnetometry purposes. This chapter brings a summary of selected examples of measurements showing the capabilities of the the presented setup. We show e.g. an optical resolution of the apparatus, measurements done on the Stoner-Wohlfarth particle and we also adress the currently hot-topic in magnetism - the magnetic vortices.

5.1 *Analytic samples - Apparatus verification*

The logical step is to first verify the functionality of the setup on the structures with an known behavior or where we can easily use the analytic modeling to describe domain structure or hysteresis loop shape. Before we start with the actual sample characterization, we dedicate short section to the characterization of the optical resolution and the stability of the setup.

5.1.1 *Laser spot and stability of the setup*

The resolution of the setup is one of the most targeted issues in the design of the Kerr magnetometers. The Eq. (4.8) places a very strict condition on the resolution limit of the optical microscope. It shows that the highest resolution is for the highest NA . Numeric aperture can be increased by using an oil-immersion objective ($n \sim 1.4$) and/or by using a high NA objective. To fully exploit the possibilities of high NA objective the whole entrance aperture has to be illuminated. Doing so would lead to complete suppression of the in-plane signal which is highly undesirable. Ergo in order to measure also the in-plane components of magnetization we have to lower the resolution. In the following text we analyze the optical resolution of the setup for the axially symmetric and tilted illumination. To quantify the spot size we perform so called knife-edge analysis. The laser spot is scanned over the sample with step-like optical properties. When we suppose the spot in the focal plane to have a Gaussian intensity profile then the optical response is govered by the convolution of the step-like profile with the Gaussian intensity profile [99]:

$$I = I_0 \int_{-\infty}^{\infty} e^{\frac{-2y^2}{w_y^2}} dy \int_x^{\infty} e^{\frac{-2(x'-x_0)^2}{w_x^2}} dx', \quad (5.1)$$

with w_y , w_x being the Gaussian beam waists in y , x direction respectively, giving the $1/e^2$ intensity curve. Parameter x_0 shifts the Gaussian beam with respect to the step profile and x marks the edge position. Solution of the integral is in the form of error function

$$I = \frac{I_0}{2} \left(1 \pm \text{Erf} \left(\frac{\sqrt{2}(x - x_0)}{w_x} \right) \right). \quad (5.2)$$

Fitting the obtained data gives the beam waist (in the direction of the edge scan) and the position of the step. Same procedure can be performed for the y direction thus we would get both: w_x and w_y . Presented approach hence allows the characterize the Gaussian beam with an elliptical waist. The basic presumption, that the beam is Gaussian, is not absolutely clear when the illumination is tilted by breaking the illumination symmetry. We performed an analysis targeting this matter where we present the results of the analysis in Fig. 5.1. From Fig. 5.1 (a) we see that the laser

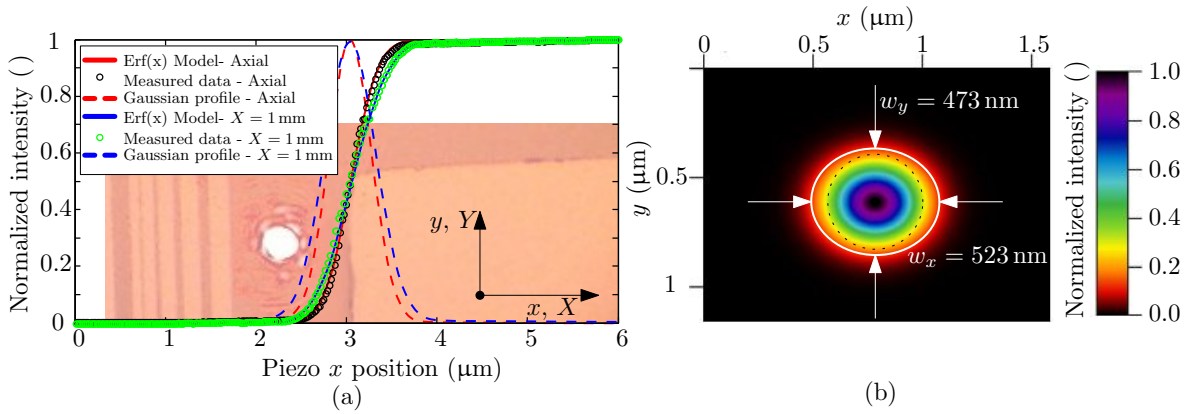


Fig. 5.1: (a) Measured intensity profiles while scanning over the step-like profile. The step profile was created by e-beam lithography and is shown in the background. We measured the intensity profiles for the spot created by the 150x objective for both the axially symmetric case and for beam tilted by shifting the objective in X by 1 mm. The angle of incidence corresponding with $X = 0.75$ mm is from Fig. 4.3 approx. 50° . The measured data has been fitted by Eq. (5.2) and from the obtained parameters we calculated the Gaussian spot intensity profile. The resulting waist for axially symmetric case is $w_x = 468$ nm and for the $X = 0.75$ mm case the waist is $w_x = 523$ nm. (b) The measurement of the step profile in both x and y direction. Obtained $1/e^2$ spot is given by the white ellipse. The theoretical diffraction limit $\Delta = 406$ nm is given by the dotted curve.

spot is larger for the angle of incidence 52° . The difference in the resolution for the axially symmetric and the tilted illumination is 55 nm only. This result doesn't fully agree with the geometrical interpretation of a axially symmetric light beam impinging on the sample surface. From the geometrical considerations the spot projection on the surface should be ellipse with the main major axis a given by $a = w_0 / \cos \alpha$, where w_0 is the waist of the free propagating beam and α is the angle of incidence. For the angle of incidence $\alpha = 52^\circ$ the parameter $a = 736$ nm which strongly disagrees with the measured value $a = 523$ nm. This disagreement suggests that the resulting beam leaving

the objective is not axially symmetric. Even for the axially asymmetric case, the fitting curves strongly agree with the measured data. This suggests that the beam in the waist can still be treated as a Gaussian beam. The only difference between the axially symmetric case and the tilted illumination are slightly different waist parameters w .

Another issue which we targeted in the characterization is the mechanical stability of the apparatus. We again performed the knife-edge measurement. When the knife-edge measurement was complete, we returned the laser spot to the position $x = 1.2 \mu\text{m}$ of the highest first derivative of the intensity curve. The spot position is then fixed for approx. 10 minutes. The highest slope of the curve assures the highest possible sensitivity. The measurement is presented by Fig. 5.2. Projecting the maximum

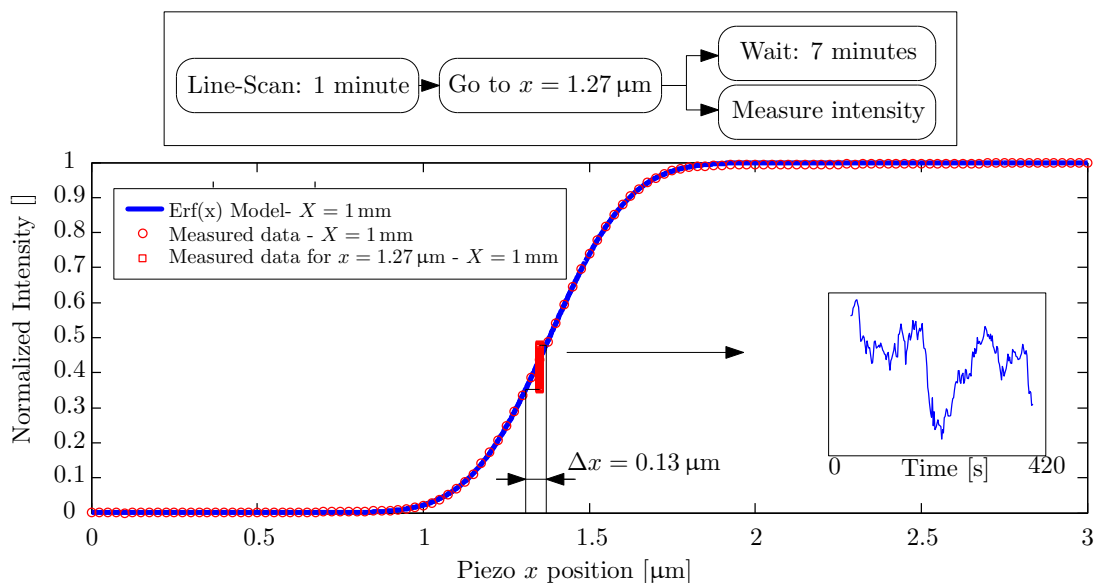


Fig. 5.2: Schematic sketch with experimental results showing the stability measurement of our experimental setup. We performed knife-edge measurement on the same structure as in Fig. 5.1 but after finishing the intensity curve measurement spot was fixed (both piezo controllers in closed loop regime) at the position with the highest slope. By measuring the intensity for 7 minutes we consequently take the highest and lowest measured value and by projecting them onto the intensity curve we get the maximum position drift $\Delta x = 130 \text{ nm}$. The inset shows time evolution of the intensity/position.

and minimum intensity to the intensity curve we obtain a worst-case-scenario position uncertainty. In the case presented in Fig. 5.2 the maximum position uncertainty $\Delta x = 130 \text{ nm}$ which is approximately $5\times$ lower than the measured resolution. From the inset of Fig. 5.2 we see that there is no clear time dependence of the position uncertainty hence it does not distort the scanned image but it can add some noise when measuring structures with dimensions comparable to the laser beam spot diameter.

5.2 Sample characterization

The following text presents the modes of operation we developed, based on the specific demands of the various types of magnetic samples.

5.2.1 Scanning-optical microscope

In the end of the previous chapter we gave a short list of modes of operation with basic definition. One of them was scanning vectorial Kerr microscope. This mode uses both piezo-actuators to scan a sample in $20\ \mu\text{m}$ range while it measures the differential and sum voltage. The maps of measured sum voltage corresponds with the reflectivity of the sample or with its scattering properties. In the following text, we often use the term: reflectivity map despite the fact that the measured data are not given in the values of the real reflectivity. We still show the measured values since in the future it can be easily recalculated to the real Fresnel reflectivity $R \in (0 - 1)$. The reflectivity maps can serve as a valuable tool when locating the structures that are below the optical resolution. Such structures are often not visible in the optical microscope camera due to its small bit resolution and lower intensity of illumination. The sensitivity of the scanning optical microscope (SOM) allows to detect the particle below the diffraction limit. In Fig. 5.3 we show the optical scanning measurements we performed on a $20\ \text{nm}$ thin Permalloy structures on Si. The smallest structure were as small as $100\ \text{nm}$. With

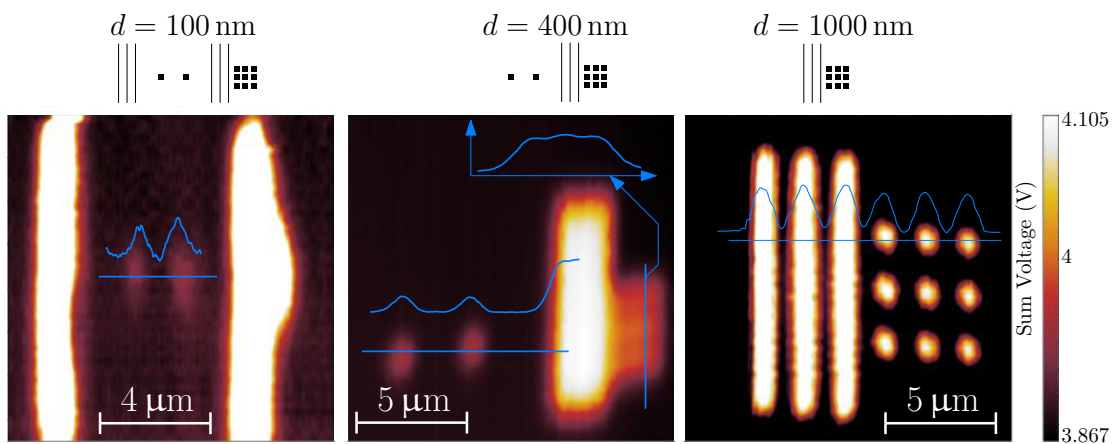


Fig. 5.3: Imaging performance of the optical scanning microscope for structures with varied geometry. The schematic sketch of the measured structures is always shown above the intensity map. The width/spacing of the structures is given by the parameter d being 100, 400, 1000 nm respectively. The insets show the measured line profiles for selected structures. In the left picture for $d = 100\ \text{nm}$ one can not distinguish among the individual lines and structures. The $100\ \text{nm}$ squares in the central part are clearly resolved. For $d = 400\ \text{nm}$ we start to see the drop in the intensity between the individual structures on the right and for $d = 1000\ \text{nm}$ the intensity in between the structures goes to the substrate value. The signal from individual structures can be detected without any cross-talk.

the 16-bit converter and the laser illumination the sensitivity of the setup allows to detect objects as small as $100\ \text{nm}$ and the high signal-noise ratio suggests that even smaller structures could be resolved. Nevertheless the great sensitivity, the intensity response map will always be given by the convolution of the laser beam width with the structures, so even though we can find the structures we can not say anything about their precise position with the uncertainty of approx. $\approx 500\ \text{nm}$. In experiment, when

measuring the hysteresis loops, we often have to precisely position the spot on the probed structure. Misplacement of the spot leads to higher noise-levels. The precise alignment can be done again by measuring the sum intensity signal while slowly scanning over the structure. The microscope control program allows to show the intensity curve as a function of the position in the hysteresis measurement mode hence we can easily find the maximum of the sum intensity where also the differential intensity is maximized.

Using the high bit-resolution of the sum signal greatly improves and simplifies the measurements of hysteresis curves. Next chapter presents the selected hysteresis curve measurements of the macro-structures as well as measurements for the structures with dimensions at or below the diffraction limit.

5.2.2 *Vectorial Kerr magnetometry*

Knowing the vectorial information of the magnetization processes vastly simplifies the data interpretation. In this section we present a short list of measurements we performed in the Kerr magnetometry mode.

Cobalt layer - sample rotation

The introductory text 2 in the MOKE magnetometry section 2.1.1 presented a measurement of the cobalt sample given by Fig. 2.1. In case (a) the measurement was performed in the hard axis and it shows clear peaks at $B = \pm 1.36$ mT. The magnitude of the Kerr rotation is for $B = -1.36$ mT even higher than the value of the Kerr rotation in saturation which suggests that the polar Kerr effect is also present. This measurement has been done on the old system that allowed the sample to be rotated together with the magnet. Measurements for sample rotation of 0° and of 180° are shown in Fig. 5.4 To understand the origin of the peaks we sum the first two curves together to get the symmetric curve. The resulting hysteresis curve has vanishing value in the saturation while having a non-zero contribution in the zero magnetic field. This fact, together with the higher Kerr rotation in the peaks than in the saturation strongly suggests the existence of OOP magnetization. The two peaks are symmetric and always present when going from the saturation to zero field. To find the switching process of the structures we consider three mechanisms: magnetization switching by domain wall propagation, magnetization switching by dense nucleation of domains or coherent rotation of magnetization [10]. The wall propagation process would possess an out-of-plane magnetization arising from the Bloch wall. The width of the domain wall would be in the range of nanometers [100]. If we take into account the fact that the polar Kerr effect is approximately ten times stronger it would still be below the resolution. In addition even if it could be detected such a small width of the domain wall together with the high domain wall velocity would not result in broad peak as in Fig. 5.4 but rather to sharp features in the magnetization curve [101]. The last argument is the shape of the measured curves itself. The domain wall propagation switching process mostly results in the square loops as in Fig. 2.1 (b). From the remaining two processes

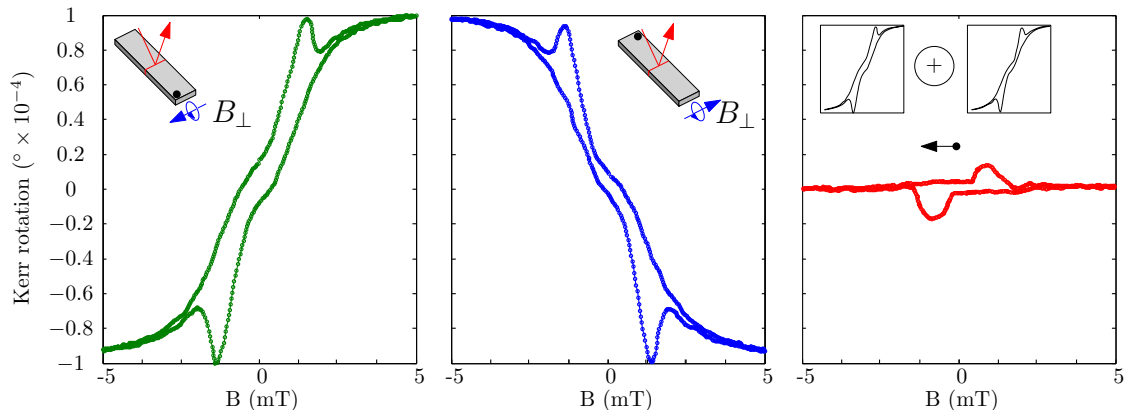


Fig. 5.4: The plot of three hysteresis curves for a bar-like sample of Co (20 nm) on Si substrate. The sample was rotated together with the magnetic field with respect to the incident laser beam. The first two curves were measured and the third one is obtained using Eq. (3.84). It gives the symmetric part of the two hysteresis curves. If the alignment of the setup is done properly it should account to the the polar magnetization curve. The arrow in the right graph points in the magnetic field evolution direction. The peaks clearly seen in both curves are also present in the symmetric loop. It suggests that in the hard axis the magnetization reversing process is not given by the magnetization rotation process but rather by the dense nucleation of domains with OOP domain walls.

only domain nucleation process can account for the shape of the curves and also for the OOP component. The coherent rotation would force the magnetization to stay in-plane since the demagnetizing energy to get the whole magnetization out-of-plane would be enormous. To get the originally in-plane layer to out-of-plane configuration the field needed is in the order of Tesla¹ which gives the clear information about the energetic demands on the out-of-plane configuration. After eliminating the improbable processes only the nucleation process remains. When increasing the external field the magnetization is forced to the hard-axis and the demagnetizing field in the sample might forces the sample to demagnetize itself to lower its energy. The shape of the first two loops could be accounted to increasing the domain size by connecting smaller domains to larger structures. The peaks would then be accounted to the gradual creation of dense domain structure with out-of-plane domain walls. The arguments for our findings of the rather feeble character so in conclusion we suggest that the origin of the out-of-plane peaks comes from the nucleation of the domains. Finding the origin of the peaks with much higher certainty would require deeper analysis of the problem.

Stoner-Wohlfarth macro-spin model

In the 1948 Edmund Stoner and Peter Wohlfarth published a theoretical paper [102] introducing a very simple model that can account for the hysteresis effect of some simple magnetic systems, where the exchange energy as well as the magnitude of the magnetization is constant. The model comes from intuitive energy considerations and it gives an energy dependence of the system on the angle of magnetization with respect

¹ We have the experimental experience with such systems from the Institut Néel, Grenoble, France. The sample were measured by the Hall magnetometry.

to the easy-axis of the sample and the external magnetic field [1, 103]

$$\frac{E}{V} = K \sin^2 \theta - M_s B_e \cos(\theta - \Theta). \quad (5.3)$$

Where E/V is the volume energy, K is the effective anisotropy constant, M_s is the saturation magnetization, θ is the angle between the magnetization and the easy axis of the sample and Θ is the angle between the external magnetic field and the easy axis. The basic presumption of the model, that the coercive field is equal to the anisotropy field would be fulfilled only for the very small particles. Despite the fact that our sample is far beyond this basic presumption the Stoner-Wohlfarth model still gives reasonable results. It cannot predict the coercive field but it gives very good results for the magnetization tilting. To model the behavior the equation (5.3) is often written in a form

$$\frac{E}{V} = B_A \sin^2 \theta - 2B_e \cos(\theta - \Theta), \quad (5.4)$$

where B_A is called the anisotropy field that equals to the coercive field for $\Theta = 0$. The anisotropy field does not incorporate only the magneto-crystalline anisotropy energy but also the shape-anisotropy given by the demagnetization energy. Finding a minima in the energy landscape gives the angle of magnetization for each of the external magnetic field value. We performed a measurements of the Permalloy sample patterned by the e-beam lithography where the Permalloy bar ($10 \mu\text{m} \times 3 \mu\text{m} \times 30\text{nm}$, w,h,t) was measured in the field perpendicular to its longer axis. The results are shown in figure 5.5. The magnetizing process in Fig. 5.5(c) at first glance might be a little puzzling but it can be simply described as follows: when going from saturation the magnetization tends to align itself along the longer dimension of the bar. In the zero field the magnetization is almost completely aligned along the longer dimension of the bar. When going to negative field at some point the perpendicular magnetic field B_{\parallel} forces the magnetization to switch abruptly to the opposite direction. The B_{\perp} then aligns the magnetization almost fully to the direction of the hard-axis. The data in Fig. 5.5 are fitted manually by changing the angle Θ so that the saturation values fits the data and we tuned $B_A = 13.2\text{mT}$ to fit the curve profile. From the fitted curve we see that not only the magnetization tilting is well described also the coercive fields fits the measured data. This shows that the Permalloy bar behaves like a single macro-spin thus the Stoner-Wohlfarth model predicts its behavior with reasonable accuracy.

The Stoner-Wohlfarth model is often overstretched to the systems where it is not applicable. The systems we measured, despite the accurate prediction, can hardly be considered to be “very small” particle as was assumed in the original paper. Nevertheless the model was used to address for the various problems in the magnetism. It has been used e.g. to predict AMR curves while rotating the magnetic field [104], to predict time-resolved measurements [105], to explain the diffraction-MOKE measurements [106] and to help with the characterization of the various anisotropies [91].

Magnetic Vortices

Magnetic vortices are curling magnetization structures which can be found in various

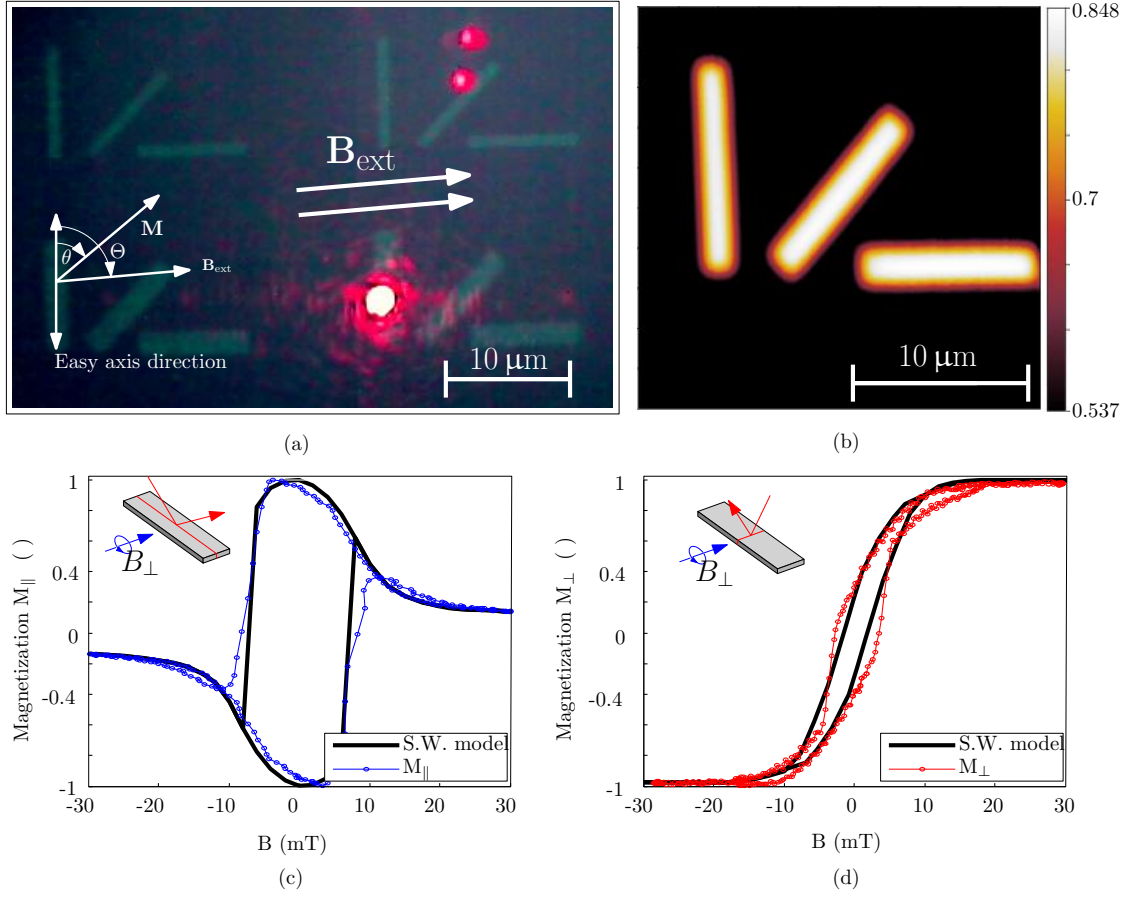


Fig. 5.5: (a) shows the image of a sample from the webcam in system. The sample is 30 nm Permalloy on Si and the measured structure is 10 μm long, 3 μm wide. The laser spot position marks the measured structure and the arrows above the structure schematically show the tilted field. In the left part of picture (a) we schematically show the coordinate system used in the modeling by Eq. (5.4). In (b) we show a SOM image of the structures. In (c) the hysteresis measurement of the easy axis magnetization with magnetic field almost perpendicular to the easy axis. (d) shows the measurement perpendicular to the easy axis. Fitted data for (c) and (d) were obtained for $\Theta = 4.2^\circ$ and $B_A = 13.2 \text{ mT}$.

thin polygons (e.g. Landau patterns) [107] and disks where the interplay between the exchange energy and the dipolar energy prefers the closed magnetization pattern [108]. The enormous increase in the exchange energy of the central spins is compensated by reorienting them partially out-of-plane. The magnetic vortex is a valuable model system with interesting dynamical properties and the promising applications in the data recording, where the four degenerate states gives a rise to not only binary but quaternary bit memory unit [109]. The proposed vortex memory has a non-volatile character. Even with the quaternary memory unit vortex states cease to exist below some threshold dimension so it can not compete with the modern hard-drives. But the speed of the switching and also the four degenerated states promises a RAM memory that would not lose its state when switched off. Apart the recording, the vortices has also been applied as a transistor unit [110] and they have also find its way to

bio-application [111].

The simulation and the sketch of the magnetic vortex is in Fig. 5.6. The vortex

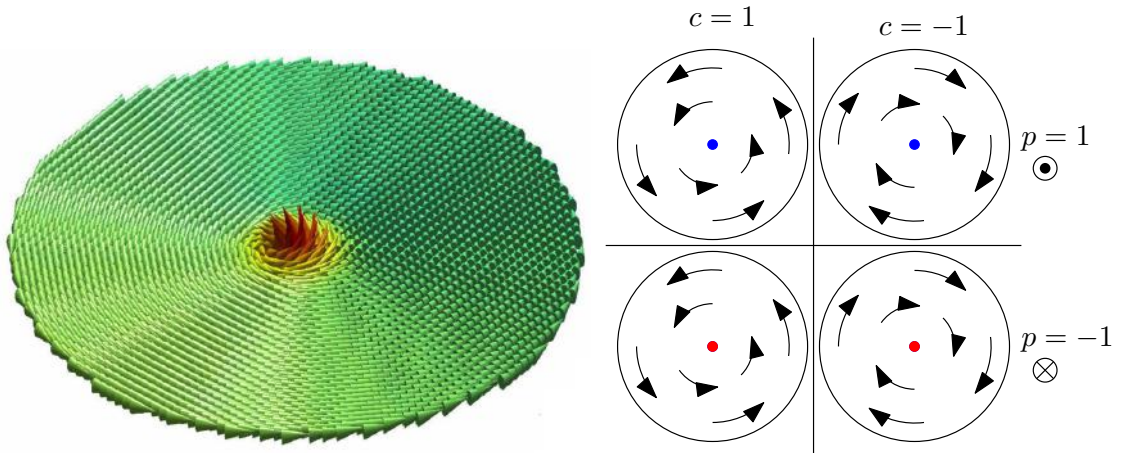


Fig. 5.6: The left picture shows the OOMMF [113] simulation of a Permalloy disk. In the middle, the out-of-plane magnetization forms a so called vortex core. On the right four possible degenerated states are schematically shown. Individual vortex can be characterized by the set of two parameters - circulation c and polarity p . Simulation courtesy of Dr. Urbánek.

state is the minimum energy state for magnetic disks with radii ranging from approx. 100 nm to couple of micron. Smaller structures (below 100 nm) form a single domain state, whereas large structures tend to form multi-domain states [112].

The vortices have been studied by the MFM [114, 115] or by the anisotropic magneto-resistance technique [116]. The response of the magnetic vortex to the external magnetic field has been targeted by the previous work [94]. In the presented thesis we also show the selected results on the magnetic vortices, since the magnetic vortices are a subject of the intense research here at BUT [117, 118].

The magnetic vortices has been theoretically studied by Usov and Peschany [119]. Using a variational principle they were able to get the analytical formulas describing the magnetic vortex. The vortex behavior and stability in the external magnetic field has been targeted by Guslienko [120–122].

When the magnetic field is present, the vortex core is displaced to a distance from the disk center in the direction perpendicular to the field. For small displacements, the magnetization response to the field is linear with the magnetic field and can be modeled by the rigid vortex model (RVM). From the RVM model the initial susceptibility is given by [123]

$$\chi_M^0 = \frac{2\pi}{\beta[\ln(8/\beta) - 1/2]}, \quad (5.5)$$

with $\beta = L/R$ is the geometric factor given by the disk thickness L and the radius R . From the susceptibility we can find the reduced vortex core displacement as

$$s = \frac{l}{R} = \chi_M^0 \frac{B}{\mu_0 M_s}. \quad (5.6)$$

This equation allows us to find the magnetic field, for which the vortex has reached the boundary of the disk ($s = 1$):

$$B_{\text{an}} = \frac{\mu_0 M_s}{\chi_M^0}. \quad (5.7)$$

At the beginning we performed a measurement of magnetic vortices on the patterned 20nm layer of Cobalt; Fig. 5.7. The smallest disk has diameter of 500 nm and the largest

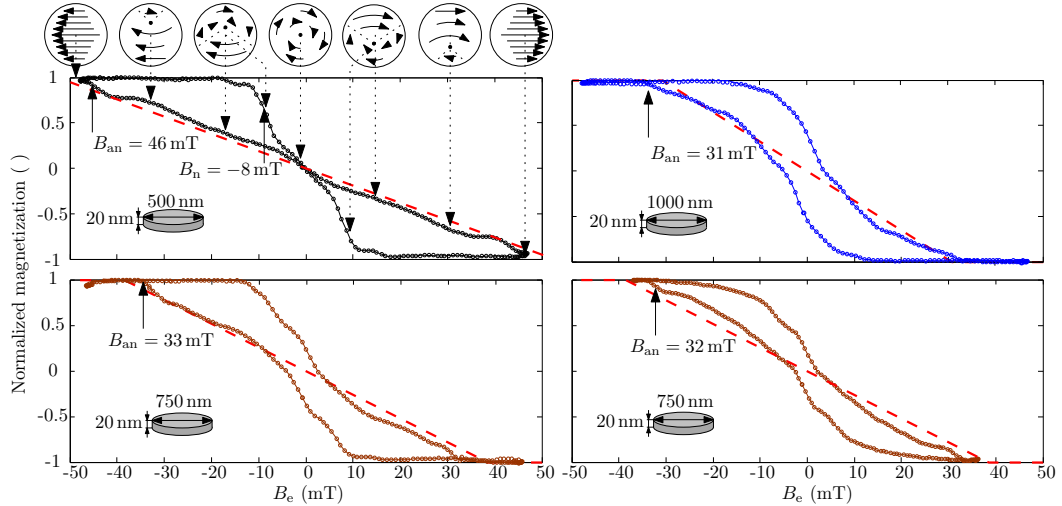


Fig. 5.7: Picture showing four measurements on the cobalt vortices. We measured the longitudinal magnetization along the external magnetic field direction. In the top left part the schematic magnetization structures are shown where the arrows connects the individual sketches with the measured data. For each measurement we calculated the RVM model based on Eq. (5.7) (dashed red curve). We measured the longitudinal magnetization where the transverse magnetization would, from the symmetry of the problem, lead to zero signal.

is 1000 nm wide. For the smallest disk we can recognize the core displacement in a linear part of the magnetization curve. When the external magnetic field is increase to the value of $B_{\text{an}} = -46 \text{ mT}$ the vortex core is quickly expelled and we see a jump in the hysteresis curve and the disk is saturated. When the magnetic field reaches the field $B_n = -8 \text{ mT}$ the vortex core is nucleated and quickly settles to the equilibrium position. For comparison we plotted also the rigid vortex model line that reasonably predicts the susceptibility but the estimation of the annihilation field does not fit the experimental data. The 750 nm and 1000 nm wide disks does not show the vortex displacement because of the negative nucleation field [124]. When going from saturation the core does not simply nucleate but the disk goes through a transition states with more complex spin structures [122, 125, 126]. We will show one example of such a structure in the experimental chapter 5. Note that for the largest 1000 nm disk the RVM underestimates the annihilation field wheres for the other cases the model predicts large annihilation fields. Another peculiarity is the difference between two 750 nm disks. It will probably be cause by a defect from the lithographic process. The shape of the hysteresis loops

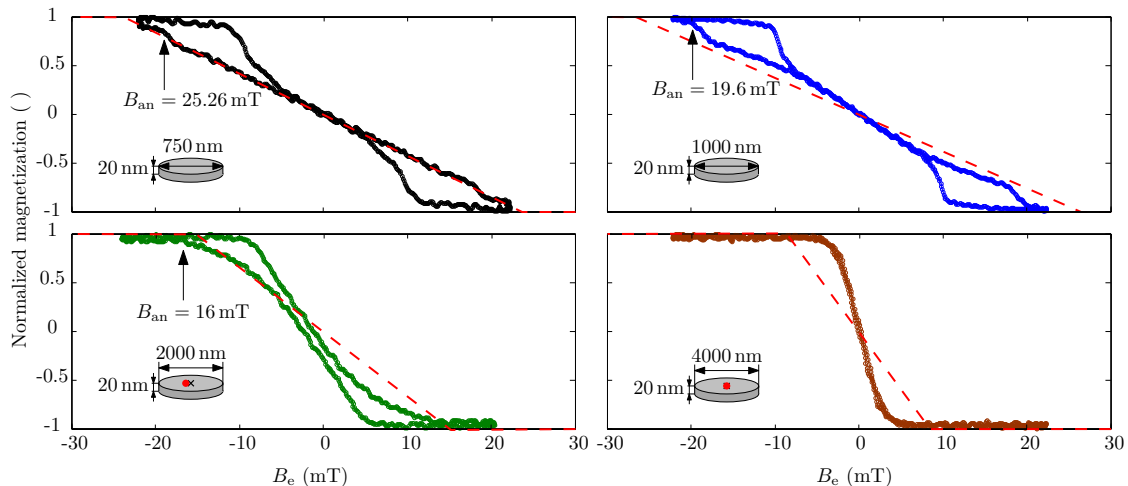


Fig. 5.8: Measurement of hysteresis loops of permalloy vortices. Again the longitudinal magnetization is measured. Disks with diameters of 750 nm and 1000 nm clearly resemble the Co 500 nm disk given by Fig. 5.7. The lack of anisotropy supports the vortex magnetization state at zero field even in the largest disks. The RVM model is shown red-dashed line. We see that for both 750 nm and 1000 nm disks the model reasonably describes the susceptibility, where for 1000 nm disk the non-linearity in susceptibility starts to be apparent. For larger disks (2000 nm, 4000 nm) we show how the effect of the finite probe completely changes the measured signal. In the insets we show the position where we placed the laser spot and measured the MO response.

in case of larger disks is also given by the fact that the vortex states are favorable in the limit of zero anisotropy energy [127]. In case of cobalt disks the anisotropy energy contribution is significant and the vortex states are less favourable than e.g. in the Permalloy. The zero anisotropy energy is often supposed for the Permalloy while for the cobalt it cannot be simply neglected. For the smaller disk the effect of the dipolar and exchange energy would be higher compared to the effect of anisotropy contribution. This favors the vortex states in smaller disks whereas in larger disk the vortex nucleation goes through the more complex transitions. Last thing we would like to point out is the vanishing annihilation amplitude for the 1000 nm disk. It is caused by the finite dimension of the probe - the laser beam. With the spot of approx. 500 nm the laser beam has to be defocused or a different objective with higher aberrations has to be used in order to get the information on the magnetization from the whole disk. The 1000 nm was measured with slightly defocused illumination.

Another set of measurement was performed on the permalloy disks. Low anisotropy helps in the process of stabilizing the vortex states during all phases of the magnetic field cycle. The measured disks 750 nm and 1000 nm have both the vortex-like hysteresis loops with well developed features: the vortex annihilation, the vortex core nucleation and the vortex core displacement. In the small field regime the displacement of the core is clearly linear in the field for the 750 nm disk. For the 1000 nm wide disk the initial susceptibility exhibits slightly non-linear behavior. The non-linearity of the core-displacement is the subject of on-going discussing since it strongly affects the

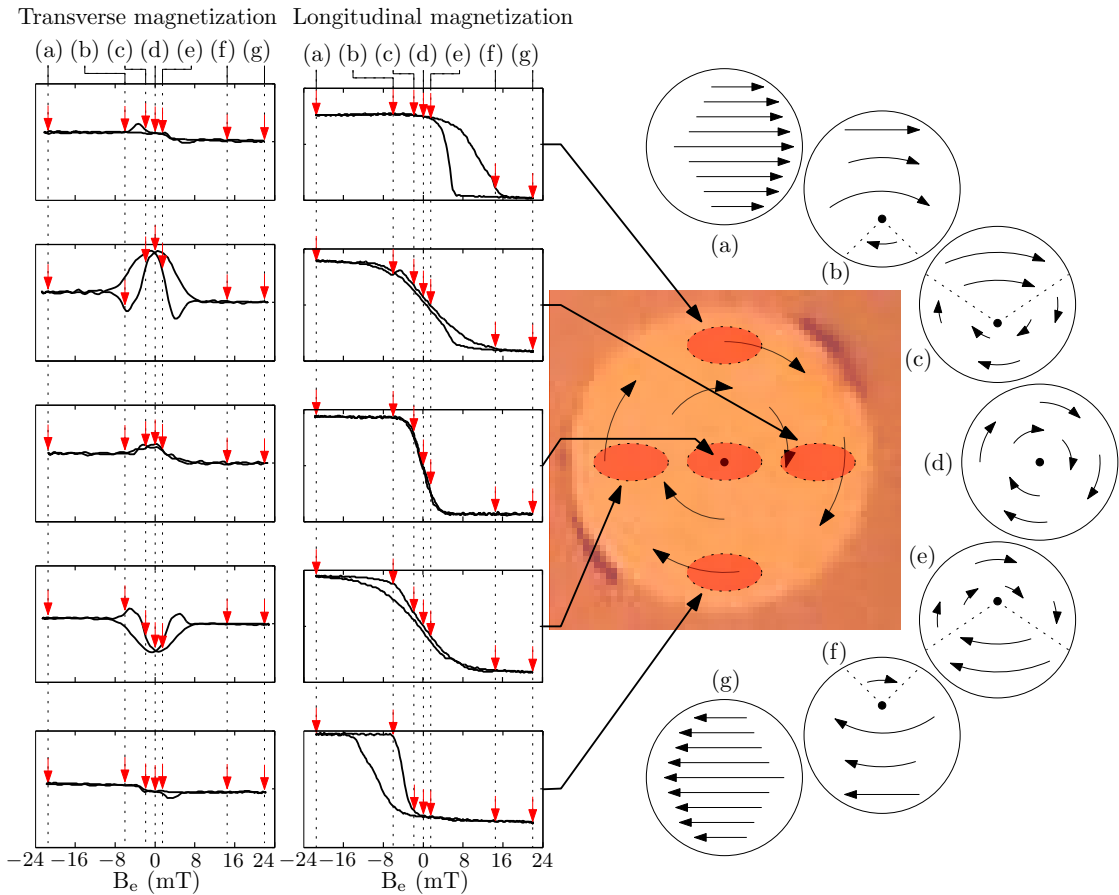


Fig. 5.9: Picture of the 4 μm permalloy disk (thickness 20 nm). On the picture we mark the positions where the individual hysteresis loops were measured. The arrows show the magnetization direction that has been deduced from the measured data. The sketches on the right schematically depicts the state of magnetization for different external magnetic fields. We measured both, the longitudinal and transverse magnetization shown in the left and right panel respectively. Red arrows on hysteresis loops mark the position of the individual sketches with mag. configuration.

dynamic properties of the vortices [117, 118, 128, 129]. For larger disks the defocusing of the laser is insufficient and the hysteresis loop might be obtained by using a different optics or by averaging more individual loops for various laser spot positions. In Fig. 5.7 we show the vanishing annihilation amplitude for 1000 nm disk where this effect is even more evident for the disks presented in Fig. 5.8 for 2000 nm, 4000 nm disk. In the 2000 nm disk we were able, by defocusing the laser to glimpse the annihilation whereas for the 4000 nm disk we were not able to see the annihilation. To evincibly prove that the measured structure is a vortex we measured a longitudinal minor loop which showed the linear $M(B_e)$ behavior. We also performed 10 measurements in total on the different positions with respect to the center of the disk. The measurements are shown in Fig. 5.9. Starting with the center position, the longitudinal loop is symmetric and has zero remanence. The linearity comes from the vortex displacement where the transition to the saturation is rather gradual than abrupt. The gradual transition is given by the convolution of the magnetization with the size of the laser

spot. With the spot $\rightarrow 0$ nm the central curve would have step profile. The transverse magnetization is almost zero with small peak and non-vanishing value in saturation. The zero value result from measuring the integral magnetization which is, for the transverse case, always zero on the vortex core path. The small peak comes from the slight misalignment of the magnetic field and the incident light beam. The top and the bottom longitudinal curves captures the annihilation and the nucleation of the vortex core. From the theoretical curves and also from the calibration on other permalloy structures we are able to attribute the sense of magnetization to the sign of the measured Kerr ellipticity, thus we can determine the sense of circulation of the vortex in the absolute coordinate system connected with the apparatus. For the case shown in figure 5.9 the circulation is $c = -1$ with respect to the axis of the sample holder. The transverse curves, as expected, are almost zero again with some minor features coming from slight non-orthogonality of the system. From the loops we estimate the misalignment to be 3° . The left curves and the right curves show, that for the transverse loops the zero-field value has opposite value for the left and right laser position a little puzzling is the existence of negative magnetization close to the nucleation field. This suggest that the vortex core does not simply nucleate at the boundary but the magnetization undergoes some more complex transition state. The longitudinal measurements show almost linear behavior with slight hysteresis. Both the left and the right curves show a dip in magnetization connected with the nucleation of the vortex. This again suggests a more complex behavior than depicted by the sketches (a)-(g).

From the curves measured at the different positions of the disk we were able to determine the vortex circulation. We need only one curve to estimate the circulation. It can be either the longitudinal curve for the top or bottom position or the transversal magnetization curve for the left or right position. From the symmetry of the problem when going from the saturation the energy of both circulations ($c = +1$ and $c = -1$) has to be equal. The observed circulation after annihilation and consequent nucleation should be random. However this applies only to a perfectly circular disk without defects, which is often not the case in the experiment. It has been shown previously that the circulation might be fixed by using the tapered disks [117, 130], circular voids [131] or by placing the disk to the close proximity of the other disk [132]. Fabricating the asymmetry seems to be simple whereas the same can not be said about fabrication of a perfect disk where the vortex nucleates with a random circulation. This task is addressed by my colleague Marek Vaňatka [116]. For a disk large enough the magneto-optical Kerr effect can be used to determine the circulation of the disk as shown in Fig. 5.9. The presented disk where the measurements of hysteresis loops was done did not show any random behavior. For a smaller disk $3\ \mu\text{m}$ wide and $20\ \text{nm}$ thick the randomness of the circulation nucleation was higher as shown in Fig. 5.10. Analyzing the data we arrive to the ratio between the + and - circulation to be equal to 75:25.

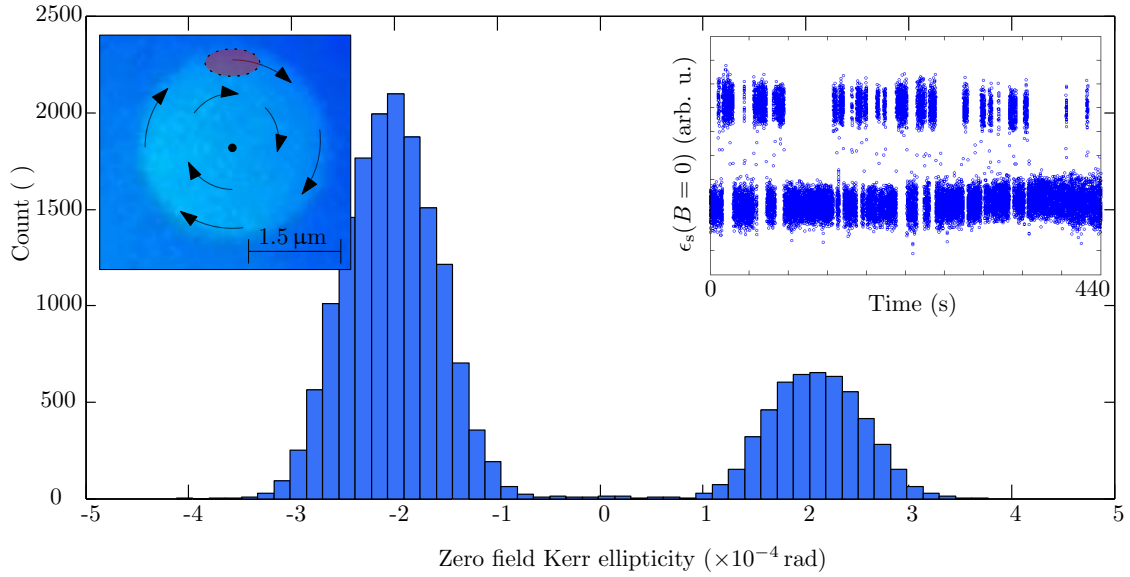


Fig. 5.10: Histogram showing the randomness of the circulation nucleation in the $3\ \mu\text{m}$ wide and $20\ \text{nm}$ thick disk. It was measured by placing a laser spot on top of the disk and measuring the longitudinal Kerr rotation. The value of the Kerr ellipticity in the zero magnetic field was recorded from measured single loops at frequency $f_0 = 42.231\ \text{Hz}$, 22000 loops were measured and processed in total. The left inset shows the measured disk with marked laser spot position and right inset shows the time development of the circulation. It is apparent that the circulation development in time is in the packets hence the application for random number generation is disputable.

5.2.3 Scanning vectorial Kerr microscope

The Scanning vectorial Kerr microscopy mode is another mode from the list given in section 4.2.2. It allows to measure the spatial distribution of magnetization with the diffraction limited resolution approx. $500\ \text{nm}$. We are able to get the vector distribution of magnetization in the $20\ \mu\text{m}$ range with the scanning rate $1.9\ \text{Hz}$. When measuring magnetization maps, as well as in the hysteresis loop measurement we have to assure that there is no significant heating of the sample. In the setup we use a grey filter to lower the intensity to $0.15\ \text{mW}$ which is still sufficient for scanning purposes. We calculated the local rise in a temperature according to [31] to be approx. 8° . It would seem that there should be no effect at all but when we measured the hysteresis loops with different incident powers of the laser we observed a difference in coercive fields of the permalloy layer (see appendix C, Fig. B.1). In order not to disturb the magnetization state we use $0.15\ \text{mW}$. Higher powers would lead to higher signal but it might affect especially the small structures.

In the measurements we first saturate the sample and we tune the half-wave plate (Figs. 4.1 and 4.7) to zero the measured differential signal. In Fig. 5.11 we show a 4 measurements of the domain pattern in $5\ \mu\text{m}$ Permalloy element (thickness $30\ \text{nm}$). Measured domain patterns clearly show the capability of the scanning Kerr microscope. The signal to noise ratio is high enough to distinguish between various orientations of

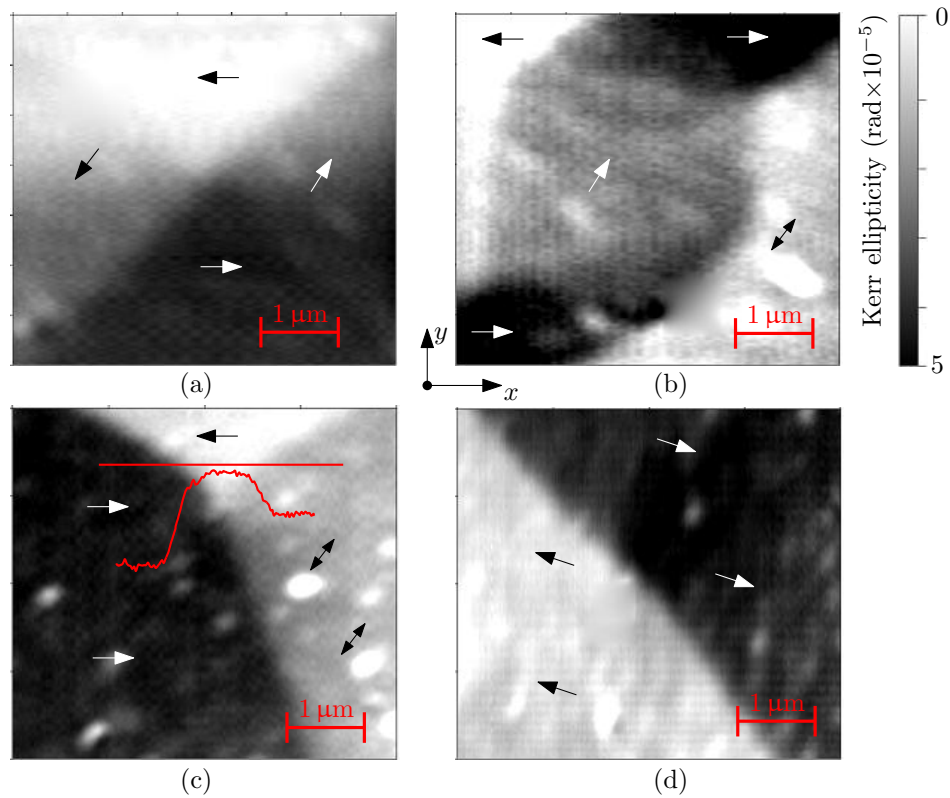


Fig. 5.11: Figure showing a four domain patterns observed in a single $5\ \mu\text{m}$ Permalloy element (thickness $30\ \text{nm}$) after demagnetization. Images were obtained when in the longitudinal mode (measuring M_x). The arrows shows the estimated direction of magnetization where the estimation was based on the signal amplitude. The pattern (a) resembles the Landau patten [107] but the domains in the right and left part are not equal in intensity. It forms the pattern as shown in [10, p. 439]. In (b) the magnetization gradually tilts from x direction through xy direction again the x . The magnetization around the darker part oriented in the $-xy$ direction except for the top left corner where the magnetization is in the $-x$ direction. In (c) we clearly see a three domain structure. The line-profile shows the signal-noise ratio we achieve with microscope. In (d) a two domain state is observed with diagonal domain wall.

magnetization. Measuring the absolute value of the difference between the two saturated states allows to estimate the projection angle of the magnetization with a good accuracy. The y component might be calculated when supposing the magnetization to be constant and let only the direction of the magnetization change. But then we would have to decide whether the calculated component has a $+y$ or $-y$ direction. For Fig. 5.11 (a) and (d) the direction of the magnetization is estimated simply from the absolute value of the Kerr rotation. In (b) and (c) we cannot decide from the measured data the absolute value of the angle of magnetization. In (c) the right domain probably has $+y$ direction since the opposite state would lead to more energetically inefficient divergence in magnetization connected with the creation of the magnetic charges.

Another set of measurements has been performed for various external field values. The results in Fig. 5.12 were taken on $20\ \text{nm}$ thick $3 \times 3\ \mu\text{m}^2$ Co element. The experi-

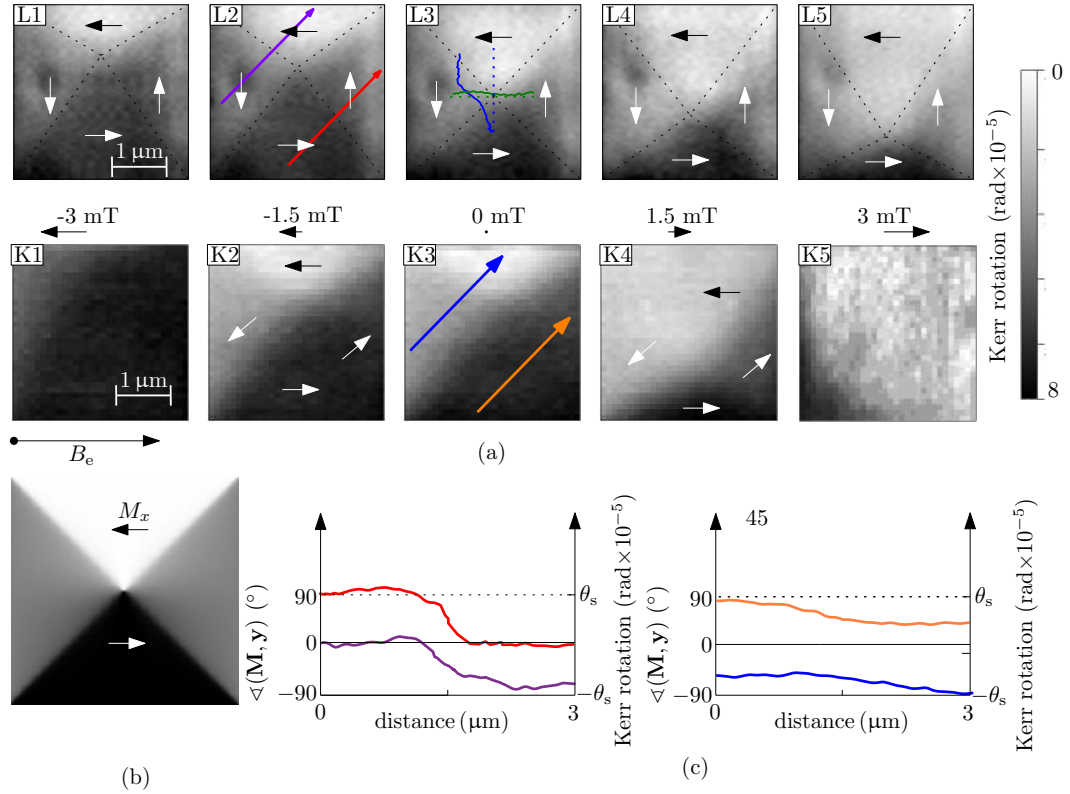


Fig. 5.12: (a) The evolution of the magnetization for the two different domain patterns in the same $3 \times 3 \mu\text{m}^2$ square. The probed magnetization lies along the external magnetic field direction. First row shows the measurement of the Landau patterns [107] and the second row gives the magnetization evolution in different domain structure. Arrows again shows the magnetization direction and the dotted lines helps the reader to see the effect of the magnetic field on the measured structure. For the picture L3 the line intensity profiles shows the change of the contrast between the top and bottom part and almost no difference for the left and right domain. The measured magnetization has a vortex-like structure that is in the rectangular structures called the Landau pattern. In (b) the simulated zero field magnetization pattern shows qualitatively the same contrast as picture L3. In (c) we plot a line intensity profiles for the Landau pattern and for the second domain structure. With the knowledge of the absolute values of the Kerr rotation in the two saturated states we can calculate the angle with respect to some principal axis (y axis in this case) as shown in the two graphs in (c). The dotted lines show the values of the Kerr rotation taken in saturation.

ments were done while measuring Kerr rotation instead of the Kerr ellipticity as in Fig. 5.11. At the time of measurement we did not have the possibility to switch between the Kerr rotation and the Kerr ellipticity measurement. The problematic part about measuring the Kerr rotation can be seen from the results of Appendix B 6. The Kerr rotation, contrary to the Kerr ellipticity, can be induced by any change of refractive index for LCP and RCP. The Kerr ellipticity arises only from different indices of absorption. In the beam path between the sample and the detector many optical elements can be found with a most problematic one; the microscope objective. The objective is together with the sample in the magnetic field which results in the Faraday rotation in the optics which affects the measured data. The ellipticity can be created only by the sample thus measuring the ellipticity reflects only the sample, not the used optics. Also for the Co and Permalloy (see theoretical curves 3.3) the measuring of the Kerr ellipticity is more efficient. Lower signal together with the signal being influenced by the optics is the reason why the contrast in Fig. 5.12 is much lower than the contrast in Fig. 5.11.

The Fig. 5.12 (a) suggest that the Landau pattern exhibits the linear magnetic susceptibility χ_m almost to the saturation. This resembles the behavior of the magnetic vortices shown in Fig. 5.7 and 5.8. Contrary to the Landau pattern the magnetization pattern given by the second row of Fig. 5.12 (a) shows the non-linear behavior. From the absolute values of Kerr rotation taken in saturation we are able to calculate the angle between the vector of magnetization and the x axis. In Fig. 5.12 (c) we compare the line Kerr rotation profiles for the two domain structures. For the Landau pattern we see sharp transition from one angle to another while for the domain structure in the second row we observe slowly varying changes in the Kerr rotation. We were able to estimate the angle of magnetization to approx. 50° . The experimentally observed signal-noise ratio clearly seen from the line profiles shows that the angle of the magnetization can be estimated with good accuracy. The Kerr microscopes has also been used to determine the in-plane angle but the achieved signal-noise ratio can not compete with the precision achieved with the presented scanning Kerr microscope [10].

The acquisition time for one picture was 1 minute, an acquisition time too long if we want to use the scanning Kerr microscope for the magnetometry purposes. Using a Kerr microscope or just the Kerr magnetometer with the spot large enough would be more viable. But resolving the in-plane domain pattern on $3\ \mu\text{m}$ big structure still posses some challenges, even for the Kerr microscopy.

Metastable iron on copper

Another system we studied was the metastable fcc iron on the Cu(100) substrate. This material undergoes the paramagnetic-magnetic transition when irradiated by Ga^+ ions of the right dose [133, 134]. The following text shortly presents scanning optical microscope and scanning Kerr microscope images of the focused ion beam irradiated structures.

The figure 5.13 (a) shows the spatial map of the reflectivity. In the microscope the structures are hardly visible where the smallest structure is a square with a side

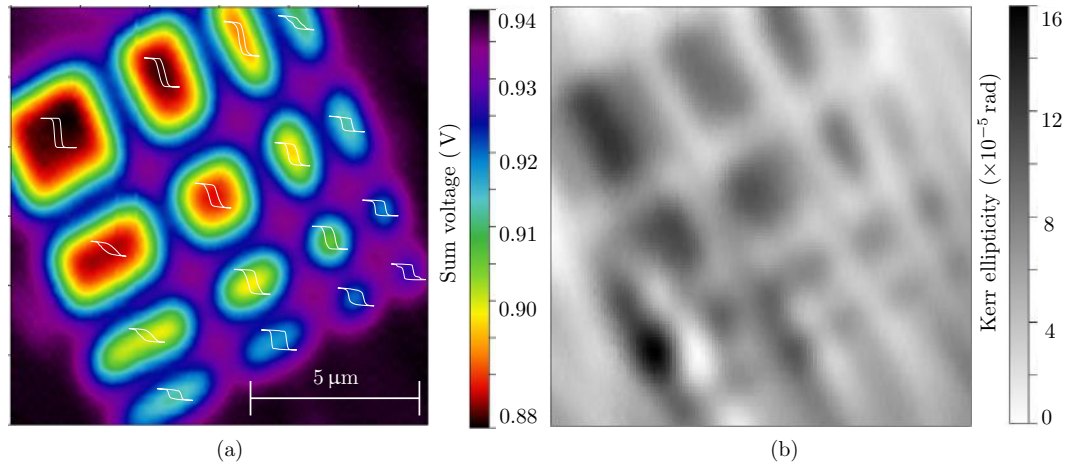


Fig. 5.13: (a) shows the reflectivity map of the patterned iron. The smallest feature has 500 nm. The transformed bcc iron has, probably due to the higher surface corrugation, slightly lower reflectivity. The smallest structure is 500 nm big and is located in the bottom right corner. For the individual areas we also measured the hysteresis loops also schematically shown in the picture. In (b) we show an Kerr ellipticity image that was obtained by subtracting the image taken in saturation.

length 500 nm. Figure 5.13 (a) also shows the hysteresis curves for the individual transformed areas. In Fig. 5.13 (b) we show the map of Kerr ellipticity. The image was obtained by subtracting the image taken in saturation. By doing so we neglect the topography signal and only the magnetic signal remains. To prevent the mis-alignment of the two scans it is a good manner to compare the reflectivity maps in between the two measurement - one in saturation and one in the remanent state. In some of the structures we can recognize more than one gray level. This is due to the existence of more complex magnetic states than single domain states. The same transformed area has been an object of the MFM study presented in Fig. 5.14 [115]. MFM with its higher resolution incomparable with the optical methods and shows complex magnetization states (e.g. Landau pattern) in the transformed areas.

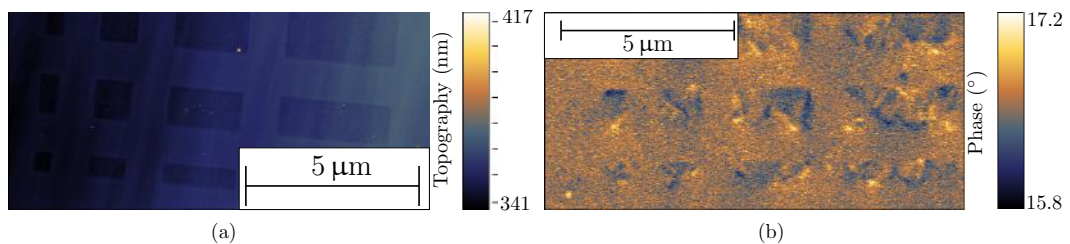


Fig. 5.14: Figure(a) shows the AFM topography of the lower part of Fig. 5.13. The individual structures are clearly visible even in the topography. In (b) we show a MFM study of the same area. It reveals complex magnetization states below the resolution of the scanning Kerr microscope.

YIG

So far we have not shown the vectorial capability in the Kerr microscopy mode. For this task we selected a material with high Kerr rotation and with the domain wall

wall width of approx. $1\mu\text{m}$. The sample is called YIG (Yttrium iron garnet) and two decades ago it was a prospective material for the recording industry [135, 136]. The Kerr microscope picture of its two remanence states is in Fig. 5.15. First one, called

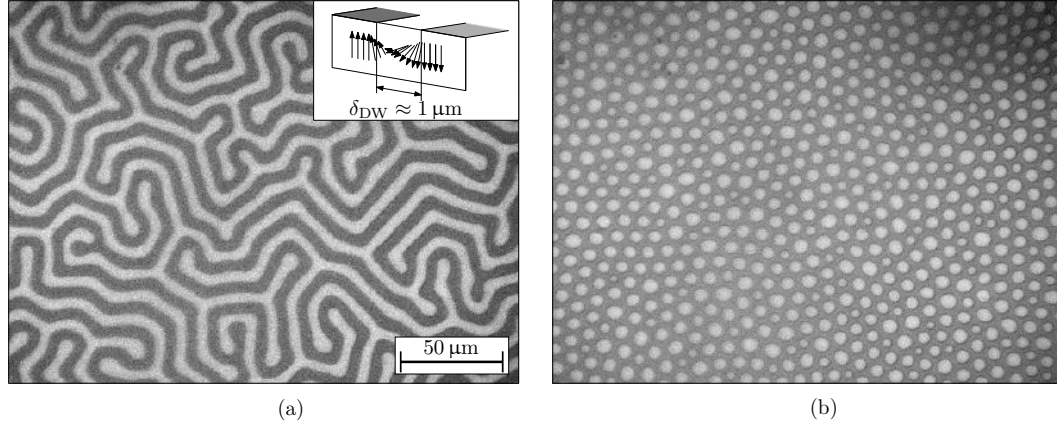


Fig. 5.15: (a) shows a wide-field Kerr microscope image with a maze-like out-of-plane domain structure that appears after saturating the sample out-of plane and releasing the field. The size of the domain is roughly $5\mu\text{m}$. The inset shows the domain wall tilting to in-plane direction and again to out-of-plane direction [136]. In (b) the magnetic bubbles are shown at the same position as in (a). The movie of the process of nucleation, bubble bursting and saturation with subsequent maze-pattern creation is in the supplementary materials (...Supplementary/ Movies/ YIGbubbles.avi).

magnetic stripes or magnetic maze pattern is in (a). The domains have width of approx. $5\mu\text{m}$. The in-plane domain wall width is estimated according to [136] to $1\mu\text{m}$ hence the domain walls should be above the resolution of our scanning Kerr microscope. Figure 5.15 (b) shows the magnetic bubbles lattice also magnetized out-of-plane. The bubbles are nucleated by saturating the sample in-plane close to its six in-plane directions of high symmetry. When releasing the in-plane field the bubble pattern is shown.

We first performed a scanning Kerr microscope imaging in the p objective position [according to Fig. 4.2 (c)]. The axially symmetric illumination probes only the out-of-plane magnetization. The scan size $20\mu\text{m}$ is relatively small compared to the size of the domains $5\mu\text{m}$ but still sufficient to reveal the domain structure. The polar Kerr magnetization map is shown in Fig. 5.17. Subsequently we moved the objective to get the angle of incidence to 45° hence allowing also the in-plane components to be detected while lowering the out-of-plane signal to 0.7 of its value for the fully out-of-plane configuration (from the dot product $\frac{\mathbf{k}}{|\mathbf{k}|} \cdot \mathbf{m}_{\text{OOP}}$). The dot product for the in-plane magnetization at the incidence angle 45° gives the same value $\frac{\mathbf{k}}{|\mathbf{k}|} \cdot \mathbf{m}_{\text{IP}} = 0.7$.

Another set of measurements was done in the $l1$ and $l2$ positions therefore from the symmetry we measure twice the same value of the polar Kerr rotation while the longitudinal contribution changes its sign. Using Eq. 3.85 and 3.84 we separate the two contributing elements to find the in-plane magnetization. The left picture was measured with the angle of incidence $+45^\circ$ and the right was measured with the angle of incidence of -45° . We fixed the darker area to 0 rad and we spatially matched the two

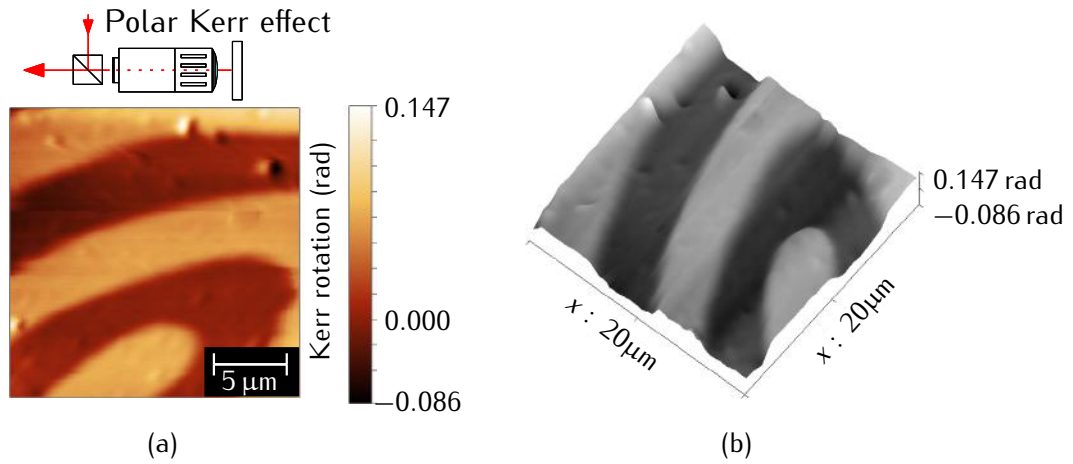


Fig. 5.16: (a) is the polar Kerr/magnetization map of the maze-like out-of-plane domain structure from Fig. 5.15 (a). Note the large values of the Kerr rotation. This comes from the combination of the Kerr and Faraday effect in the YIG sample [135, 136]. Figure (b) is a 3D view of the same domain pattern as in (a). It shows the immense signal-noise ratio given by the huge Kerr rotation.

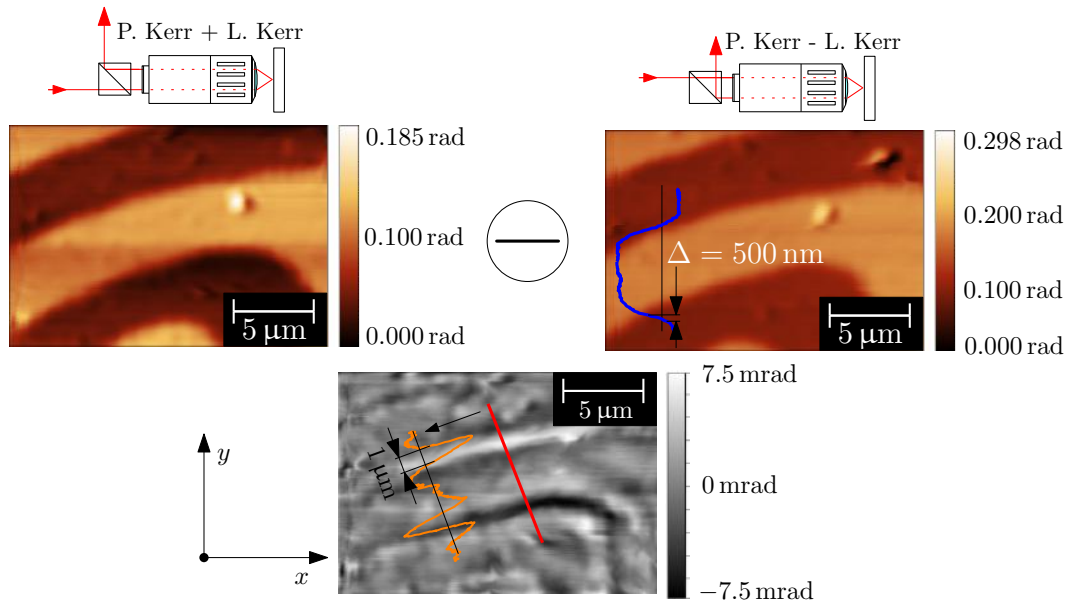


Fig. 5.17: Figure showing an obtained data for the scans with the incident angle $\pm 45^\circ$. In the right $+45^\circ$ image we plotted a schematic line-intensity profile with marked 500 nm to show that the gradual transition is not given by the resolution of the measuring device. In the bottom picture the difference of the two upper pictures is shown. The line profile shows the in-plane domain wall profile with marked 1 μm scale.

images using the well visible impurities to compensate the possible drift. Subsequently we numerically calculated the difference of the two images. The resulting image, despite the worse quality, shows the two well visible lines with the opposite sign of the Kerr rotation. This experimental finding agrees with the sketch of the domain pattern given in Fig. 5.15 (a). The magnetization transition from the out-of-plane+ to out-of-plane- direction is done through the 180° domain wall with in-plane orientation where the in-plane component lies along the domain boundary. The contrast of the domain wall for the domain direction perpendicular to x direction is expected to be zero. From the measured image we see that although the contrast is lower it is still non-zero. This could arise from the wrong alignment connected with a problem of subtracting two images with finite size of the pixels, or it may come from the slight misalignment of the optics originating in the 2D objective axis cross-talk that was not known at the time of the measurement of the presented data.

5.2.4 Scanning vectorial Kerr magnetometer

In the previous text we have shown the vectorial Kerr magnetometry and scanning Kerr microscopy techniques. The mode presented herein to some extent combines the best of the two techniques. It allows to scan the sample and at the same time the hysteresis loops are measured in a fully automatic manner. The post-processing of the measured data allows to determine the spatial distribution of coercive field B_c , anisotropy field B_A , reflectivity R , magnetization \mathbf{m} , initial magnetic susceptibility χ_m^0 . The disadvantage is, that the method is suitable only to non-stochastic magnetization processes. For the random behavior, measuring the single-loops would lead to chaotic data. When averaging the measured loops at one laser spot position, the average magnetization behavior is recorded. By combining the measurements of the individual orthogonal components of magnetization we can get the spatial evolution of the vector of magnetization, either in 2D or even in all three dimensions.

In Fig. 5.9 we show a measurement where we measured ten hysteresis loops and we can see a high spatial variation in the local magnetization response to the external magnetic field. We performed similar measurement on the $8\ \mu\text{m}$ Permalloy disk where we measured the hysteresis loops with a step of $500\ \text{nm}$ on the $10 \times 10\ \mu\text{m}^2$ area. We averaged 50 hysteresis loops for every position. The measurement itself, with averaging and piezo position settling, takes approx. 50 minutes for one direction of magnetization. Thus for both in-plane components the time is doubled. To assure the same magnitude for M_x and M_y we measured the orthogonal structures from Fig. 5.5 and we equaled the maximum Kerr rotation for both cases: when measuring the longitudinal Kerr rotation and when measuring the transversal magnetization in the longitudinal Kerr mode. Described in the objective entrance aperture coordinates from Fig. 4.2 (b) we used the $t1$ and $l1$ ports. The quantity that is measured is longitudinal Kerr rotation for x and y direction. In the following text, we will refer to the longitudinal Kerr rotation for x (y) direction as M_x (M_y). Then the vector field of magnetization

$\mathbf{M}(B_e, x, y) = (M_x, M_y)$ is created by the data post-processing. The post-processed data for three external magnetic field values are given in Fig. 5.18. Presented data

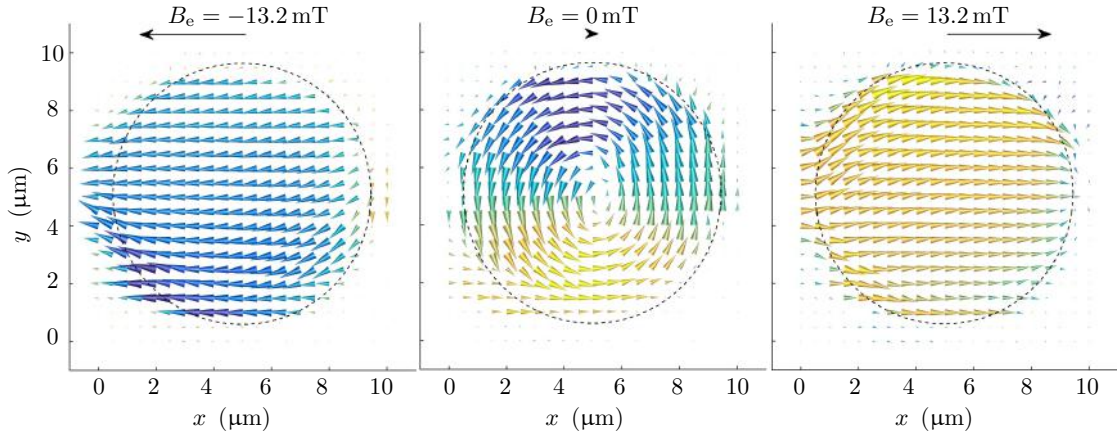


Fig. 5.18: Figures showing a spatial distribution of the measured \mathbf{M} vector for the $8\ \mu\text{m}$ disk (thickness $30\ \text{nm}$). Left and right pictures show the magnetization of the disk in the saturation while in the central picture we see the vortex state of magnetization with the circulation $c = 1$. Measurements are post-processed from the total number of 44100 loops. The position grid has a total number of 441 points with relative spacing $500\ \text{nm}$. The arrow color corresponds to M_x .

shows two states of a magnetic vortex. The zero-field state has well apparent vortex structure (see the simulation in Fig. 5.6) with the vortex core in the middle and the magnetization curling around the vortex core. When going to higher fields the core is annihilated and the disk goes to the saturation. The three presented states are selected from the 251 figures in total. The full movie of the magnetic vortex magnetization reversal is in the supplementary materials². From the movie one can recognize the three processes in the disk: vortex nucleation ($B_n = \pm 0.65\ \text{mT}$), vortex core displacement and the core annihilation ($B_{\text{an}}^+ = 5.38\ \text{mT}$, $B_{\text{an}}^- = 6.3\ \text{mT}$). In deeper analysis one can find, that before the actual nucleation of the vortex the transition magnetization state is formed. It was predicted by micromagnetic simulations in 2001 [122] and in the article they call it the “spin instability” mode. It was thought that this mode is found only in the micromagnetic simulations. We also performed a set of micro-magnetic simulations in OOMMF and Mumax3 [137] micro-magnetic solvers, where we found this mode in much smaller disks than $8\ \mu\text{m}$. To compare the numeric simulations with the measured data we plot the selected magnetization states side-by-side with the numeric simulations. The results of the comparison are in Fig. 5.19. In the analysis of the obtained pictures we start from the simplest case given by the saturated state of the disk. Both the micromagnetic simulation and the measurement show the majority of the spins to be aligned with the external magnetic field while at the boundary the charge avoidance principle lowers the energy by tilting the magnetization from the direction of the external magnetic field [138]. This is done at the expense of the Zeeman energy. From what we observed the magnetic charges at the boundary

² Supplementary\Movies\Disk-8um-Cones.avi

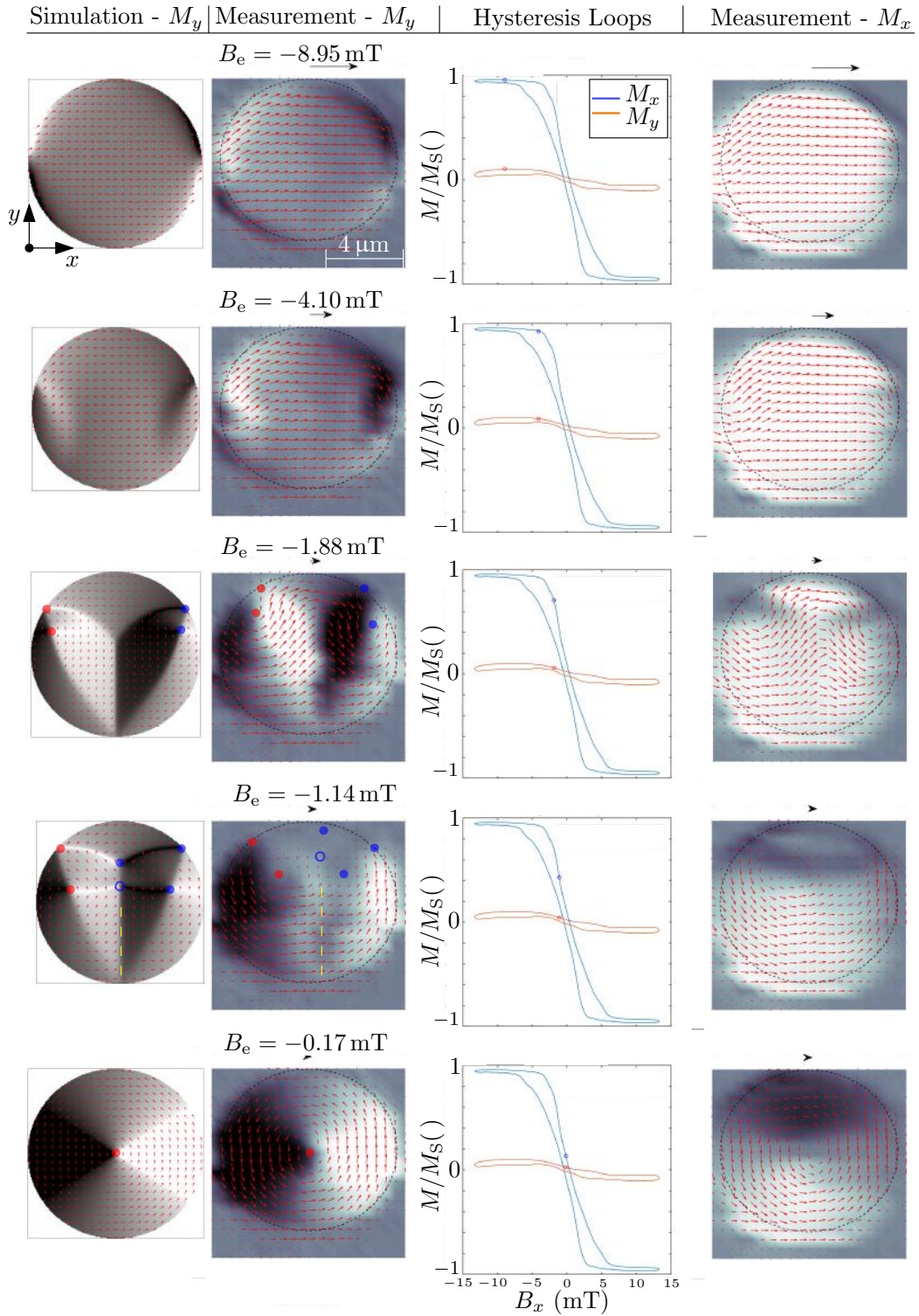


Fig. 5.19: From top to bottom we show the nucleation of the magnetic vortex in the external magnetic field. In the left panel Mumax3 simulation is shown. The background of the images gives the magnitude of M_y . Second row shows the post-processed data where the arrows show the measured vector of magnetization for every individual grid point. The background color again corresponds to M_y . The third row shows the hysteresis loops representing measured M_x and M_y obtained by making a spatial average of the Kerr rotation for every individual magnetic field step with the circles showing the actual position at the loop. For the right row the same as for the second row applies only that the background is given by M_x .

stabilizes the vortex nucleation. When going with the field above approx. 30 mT, the magnetic charges lose their asymmetric formation and the presented structure starts to behave in a different manner with the square-like hysteresis loop. It probably undergoes a transition to the single domain state. For the field of -4.10 mT the boundary charges almost disappear by moving the M_y magnetization inside the disk. Consequently in the field of approx. 2 mT the wing-like magnetization pattern is formed. From the micro-magnetic simulations we see that four places with out-of-plane magnetization are formed where the two lower OOP components are given by newly created vortex cores. From the measurement it is not directly apparent but in a closer look the curling of the magnetization around the two spots suggests that the results of the micromagnetic simulations are correct. In M_x the nucleation of the two cores is more apparent because of the spots with lower contrast. The blue and red dots mark the areas of the out-of-plane magnetization. We placed the same marks to the estimated spots found in the measurement where the polarity of the out-of-plane component is unknown in the measurement. At the field of -1.14 mT we observe a drop in the magnitude of the magnetization in the upper part of the image. Originally we considered this state as a discrepancy between the simulated magnetization structure and the measured data. But the similarities start to show up in the deeper analysis of the two images. The simulation pattern shows a total of six out-of-plane areas marked by blue and red dots. In the analysis of the simulated magnetization pattern we found out that one of the originally thought vortex cores is actually an anti-vortex. We marked it by a blue circle. Looking at the measured image we clearly see the dark and bright areas on both sides of the disk. Another similar feature is marked by the dashed yellow line. In the measurement we see the drop in the horizontal magnetization. This originates in the anti-parallel spins in the close proximity below the resolution of our instrumentation. This leads to a measured zero total Kerr rotation. The upper part is more problematic. The abrupt changes in the magnetization seen in the simulation cause the signal averaging hence it effectively lowers the signal almost to the detection limit. In the process of the data analysis we again marked the possible positions of the vortex/anti-vortex in the measured map, despite the fact that finding the position of the top vortex and the anti-vortex is difficult. In the measurement we were not able to get the intermediate step between the vortex shown in the last picture and the previous state. From the simulation we conclude that the two bottom vortex cores propagate together with the anti-vortex to the bottom part of the disk, while the core at the top is annihilated at the edge. The anti-vortex annihilates with the vortex of the same polarity leaving only the “red” out-of-plane magnetization. To help to understand the vortex formation presented by Fig. 5.19 we show in Fig. 5.20 the images of the vortex nucleation process obtained from the micromagnetic simulations. Some of the pictures are the same as in Fig. 5.19.

Once the vortex is nucleated it moves perpendicular to the magnetic field towards the disk edge. The vortex displacement with subsequent annihilation does not show any unusual behavior but it still gives some information e.g. annihilation radius, pinning.

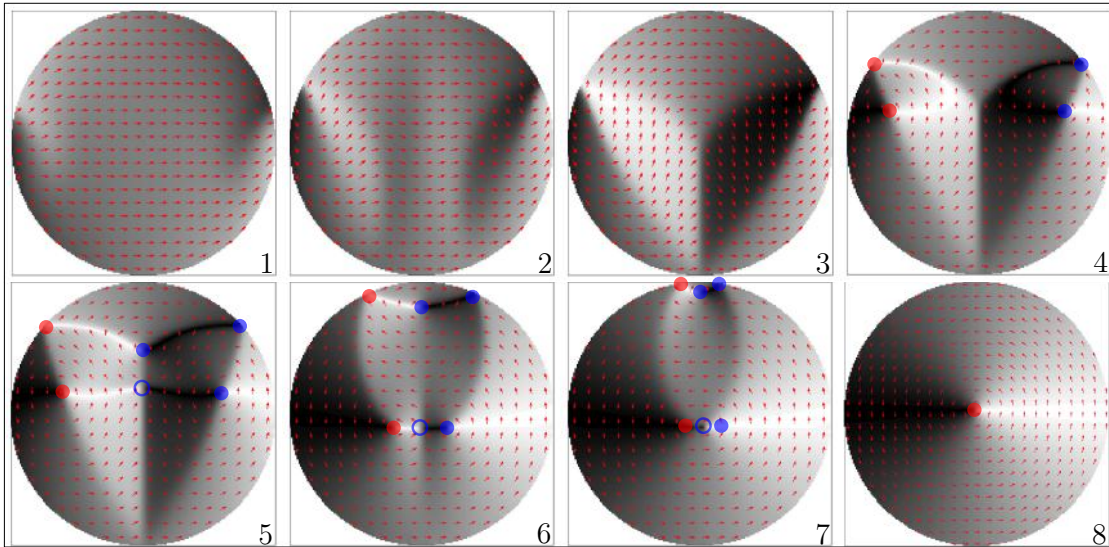


Fig. 5.20: Figure providing the supplementary data to Fig. 5.19. Arrow shows the magnetization direction and the color corresponds to M_y . The dots shows the out-of-plane magnetization direction where the red color stands for the negative direction.

The annihilation is not connected with any abrupt changes in the magnetization vector hence the obtained pictures does not show any vanishing magnitude of magnetization vector as we saw previously. The image sequence with the vortex core approaching the boundary, again compared with the micro-magnetic simulations, is shown in figure 5.21.

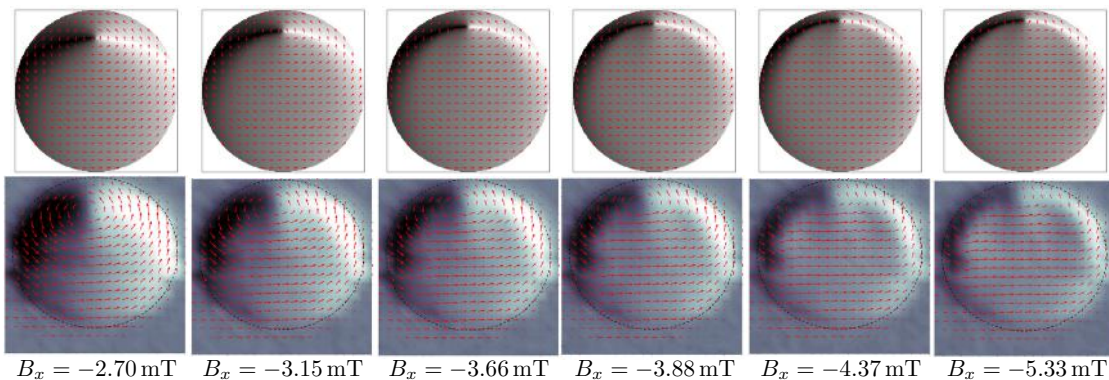


Fig. 5.21: Image sequence of the vortex core being pushed towards the disk boundary. The first row are the micromagnetic simulation images. The bottom row shows the measured data.

From the external magnetic field values and the pictures shown above we see the non-linear displacement near the disk boundary. Such a measurement might in the future serve for measuring the annihilation probability as a function of the temperature and the distance from the edge of the disk.

The presented pictures have been selected to show the interesting behavior of the measured disk. However, the majority of acquired pictures is not shown in the thesis. Complete post-processed movies are in the supplementary materials. The movies show

the field evolution of the M_x and M_y components. We also added a video showing the evolution of same disk where the maximum magnetic field was chosen so that the disk does not undergo an annihilation process³.

So far we have discussed only the spatial distribution of the in-plane vector of magnetization where the hysteresis loops also shown in Fig. 5.19 were left without any comment. Starting with the M_y loop we see the typical vortex loop with all the features mentioned many times in the preceding text. Despite the fact that the disk is $8\ \mu\text{m}$ we clearly see the vortex annihilation at $B_{\text{an}}^+ = 5.38\ \text{mT}$ and $B_{\text{an}}^- = 6.3\ \text{mT}$. The difference in the annihilation fields probably comes from the existence of the defect, what would also explain the different core nucleation processes for the nucleation from the positive and negative field (see supplementary video). The defect would also explain the non-stochastic behavior we observed in this particular disk and did not see in many others. The M_y curve is slightly different from what we would expect. With the magnetic field in the x direction the magnetization has a clear symmetry plane given by the plane perpendicular to the magnetic field vector and going through the center of the disk. The M_y curve is expected to be zero for every magnetic field step. The non zero values of the M_y curve can not originate from the optics mis-alignment since the x and y signals has been matched to give the same Kerr ellipticity in saturation. They most probably result from the non-centered scan area, as can be seen from the pictures.

Summarizing the work done with the scanning vectorial Kerr magnetometer we have, among many other structures, characterized the disk with the highly reproducible magnetization process. The analysis of the obtained data have, with help of the micromagnetic simulations, proved the existence of the “spin-instability” state in the real disk. The measurement of the complex magnetization state well corresponds with the findings of my colleague M. Vaňatka [116]. In his work he used AMR (anisotropic magneto-resistance) measurement to probe the circulation of the Permalloy disks where in the preliminary measurements done on the $4\ \mu\text{m}$ disks he observed strange behavior resulting in the drop in the resistance below the expected values. In the article [139] the authors claim that the peaks are connected with the nucleation of the vortex core in between the AMR contacts. In our findings the sudden drop in resistance is caused by the formation of the wing-like magnetization structure and its further development to more complex magnetization states.

5.2.5 Coercive field mapping mode - CFM

The previous section has shown the results obtained with the analysis done by the scanning vectorial Kerr magnetometer mode. This mode, despite its great universality, has a high time-demands and the measurements tend to be rather long. The mode presented herein combines the scanning Kerr microscopy mode and the scanning Kerr magnetometry mode. The sample is scanned at approx 1 Hz and at the same time the magnetic field is oscillating at the frequency approx. 100 Hz. The field is set

³ The videos with self-explanatory file names are in the ...Supplementary/Movies folder.

to the value where it can certainly saturate the sample. The data we collect is the spatial distribution of the coercive field, sum voltage and AC Kerr ellipticity. The AC Kerr ellipticity gives the information on the magnetization of the sample, sum voltage again corresponds to the reflectivity and the coercive field map can reveal the domain nucleation centers or the spatial distribution of the anisotropy axes. The sample we present in the short section devoted to the coercive field mapping is again the ion beam transformed fcc Fe on Cu(100) substrate. We have already treated the sample in the scanning Kerr microscope section 5.2.3. The previous results proved the magnetic origin of the differential signal from the transformed areas. The areas has been subsequently measured by the Kerr magnetometry which showed the square-like hysteresis loops for almost all transformed areas. More importantly the largest area shows square loop will with high signal-noise ratio and well recognizable coercive field. The very good signal to noise ratio allows the CFM mode to be applied without any restrictions.

At room temperature the fcc lattice Fe is stable and does not undergo spontaneous recrystallization. When irradiated with the ion beam the energy supplied to the system is high enough to locally transform the iron to the bcc state which is ferromagnetic, in contrast to the paramagnetic fcc phase. The question arises, what would be the crystallographic orientation of the transformed area. From the scanning electron microscope (SEM) images in Fig. 5.22 we see a varying contrast depending on the relative angle of the sample with respect to the electron gun. We attribute the contrast variation to the electron channeling process. The channeling arises when the incident particle trajectory is aligned to a suitable lattice axis that when viewed from the incident particle point of view forms a channel of sort. The collision crosssection is then effectively lowered and the typical SEM signals - backscattered electrons (BSE) and secondary electrons (ES) are lower.

We performed a CFM measurement on the transformed area with dimensions $10 \times 10 \mu\text{m}^2$ with a fine resolution 500 nm. The obtained map of the coercive fields is given by Fig. 5.23. In the picture three areas can be clearly recognized. In the left part we observe the coercive field to be approx. 5.6 mT. Then in the darker spike seen in Fig. 5.23(b) we observe a sudden drop in the coercivity in (a) as well as a drop in the SEM contrast. The right part has a highest coercive field of approx. 6.3 mT. In the lower right corner the coercive field again starts to fall. From the channeling contrast in Fig. 5.22, from the CFM measurement given by Fig. 5.23 (a) and also from the reflectivity map in the inset of Fig. 5.23 (b) we conclude that the whole area is fully transformed. In the SEM image and in the coercive field map we see that a needle has a different magnetic and electron emission properties. On the basis of the article [133] we therefore conclude that the needle is a single crystal while the areas with the different SEM contrast and the coercive field are given by a finer mixture of different crystallographic axes. It would explain the lower coercive field since in the single crystalline material the pinning is lower. We have not observed any changes in the magnetization magnitude or the optical reflection in between the needle and the

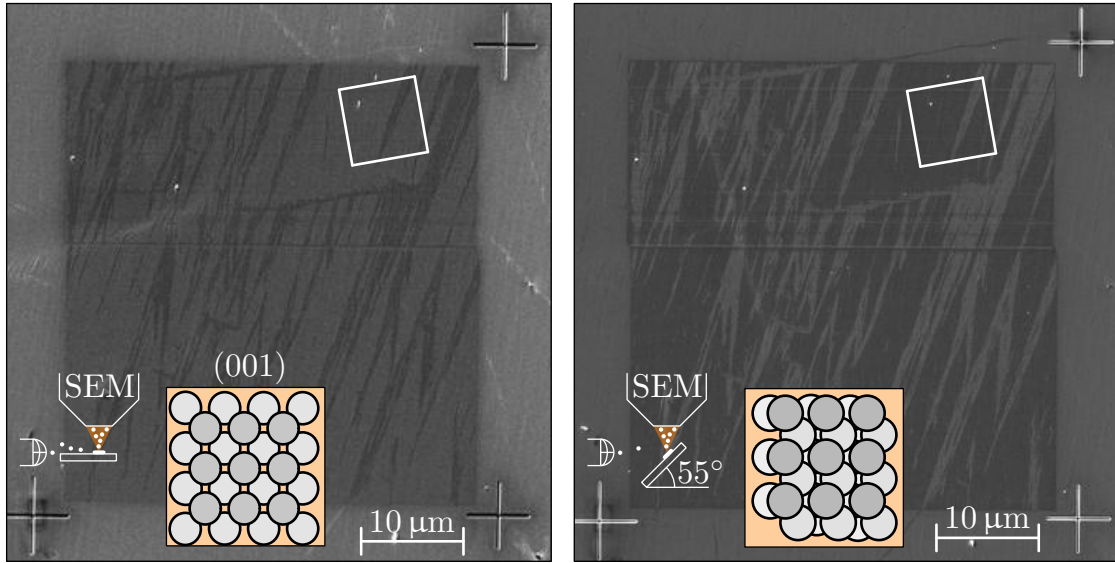


Fig. 5.22: The SEM images of the transformed area. In the recrystallization process we see from the SEM image and the SOM image 5.13 change in the contrast for the transformed areas. The optical reflectivity as well as electron emission coefficient is altered together with the magnetic properties of the layer. The tilted white square marks the $10 \times 10 \mu\text{m}^2$ area where we performed the CFM measurement. At the bottom we schematically show the e-beam and the relative orientation of the sample-SEM column. The different view from (100) and 55° direction is again shown giving an idea about the channeling probability in different crystallographic orientations that are thought to be present in the needle in the highlighted area.

rest of the transformed area.

Summarizing the CFM section we can spatially resolved the changes in the coercive field with the spatial precision 500 nm. The accuracy of the coercive field measurement is limited by the teslameter we use to approx. 0.1 mT. The obtained data are in an agreement with the SEM images and with the theory about the different crystallographic orientation of the darker/brighter areas. Mastering the process of accurate and repeatable recrystallization of the metastable iron will require further research but the preliminary results suggest that this system is a promising candidate for high density recording apart from the fact that it is a great model system for probing the effect of the artificially induced crystalline structures on the magnetic properties.

5.3 Experimental results - summary

The chapter presenting selected experimental results started with the characterization of the laser spot where we focused in more detail to the distortion of the spot when using a non-axial illumination configuration. We proved experimentally that we have a diffraction limited resolution $\Delta = 500 \text{ nm}$. Subsequently we targeted the stability of the setup, since in the presented work we perform measurements with time-demands ranging from tenths of second to couple of hours. The actual experimental part starts with the data from the old system, where we used the basic symmetry to separate

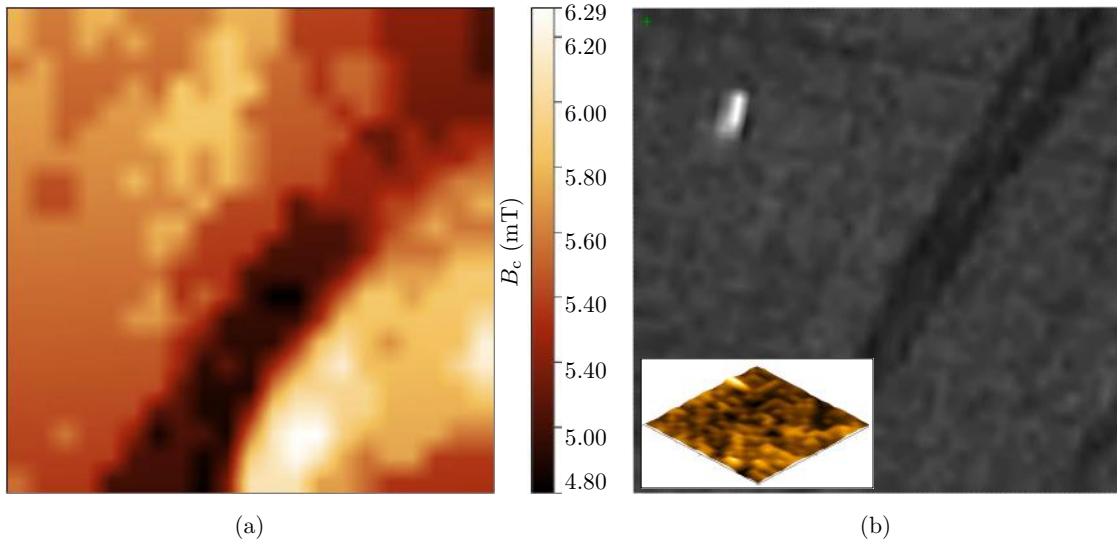


Fig. 5.23: Image (a) is the coercive field map measured on the area given by Fig. 5.22. We also cutted the large image 5.22 only to show the measured area in figure (b) in more detail. The inset in the right picture shows the reflectivity map from the CFM measurement that does not show any reflectivity variation in the transformed area.

the weak out-of-plane signal from the large in-plane signal. The experimental results obtained with the designed MIRANDA vectorial Kerr magnetometer starts with the characterization of the analytic structures.

The performance of the vectorial Kerr magnetometer is verified on the structures with known magnetization processes. Another set of measurements was done in the vector Kerr microscope mode. We show high signal-to-noise ratio we achieved for the in-plane structures both with and without external magnetic field. Another measurement in the vectorial Kerr microscopy mode was done on the YIG sample. The zero-field magnetic state is known and was shown by both the wide field Kerr microscopy and by the scanning Kerr microscopy. With the help of the basic symmetries of the longitudinal and polar Kerr effect we separated the in-plane domain wall contribution from the large out-of-plane signal. Extending the scanning Kerr microscope with the measurement of the hysteresis curves we have shown a magnetic vortex and its behavior in the external magnetic field. We have successfully confirmed the existence of the “spin-instability” state that was previously though to be present only as a consequence of the micromagnetic simulation with the finite mesh. In the end of experimental chapter we focused on the metastable fcc iron on Cu(100) substrate. Together with SEM measurements we conclude that the needles in the SEM and CFM images are single crystalline, while the rest of the layer is a mixture of the differently oriented fcc Fe grains.

6. CONCLUSION - CONTRIBUTION OF THE THESIS

The presented work describes theoretical foundation, as well as applications of magneto-optical Kerr effect with respect to various tasks connected with the sample characterization. The work introduces the reader to the field of magneto-optics from the basics to more complex topics. It starts with a brief introduction of possibilities and limits of the magneto-optical methods and subsequently continues towards the basic theory leading to a simple description of the polarization changes in the optical setup. The magneto-optical Kerr effect exhibits itself as magnetization induced polarization modulation of the incident light wave. We were able to observe polarization changes as small as 2×10^{-6} rad which is two orders of magnitude lower than the regular level (approx. 10^{-4} rad). We also show how the sample can be modeled in the 2×2 matrix framework. This is particularly useful when quantitative information about the sample is required.

In the theoretical chapter we derived the different refractive indices for the left and the right circularly polarized waves, where the difference of the two refractive indices is directly proportional to the dot product of the light propagation vector \mathbf{k} and the vector of magnetization \mathbf{M} . The theoretical dependencies, obtained by the 4×4 matrix formalism, clearly show the effect of the dot product on the magneto-optical response of a single magnetic layer. The polar magnetization gives rise to an even dependence of the magneto-optical observables as a function of the angle of incidence and the longitudinal magnetization induces an odd response to the angle of incidence. We are exploiting this symmetry in order to separate the polar and the longitudinal Kerr effects. This allows us to quantitatively evaluate the individual components of the magnetization vector. For a general \mathbf{M} orientation we propose a method where in the four consecutive steps we are able to get the whole vector of magnetization. In case of a sample where the magnetization is in-plane only, just two measurements are needed.

The ability to probe all the components of the magnetization brings new possibilities to the sample characterization process not seen in many other methods and instruments. In our approach, we have exploited the off-axis light illumination in the microscope objective by mounting the objective to the 2D translation stage. This solution provides us with great flexibility while retaining the stability of the setup.

We had to deal not only with the design of the MIRANDA scanning Kerr magnetometer but also with the software development, testing and more importantly by actually using the setup for the sample characterization. We have developed various modes of operation to exploit the possibilities of the designed system.

We proved the capabilities of the designed system in the experimental section where

we studied, apart from the apparatus testing, also the unknown processes in the samples our magnetism group currently deals with. We were able to measure the single magnetic nano-disks with the disk diameters down to 500 nm and to separate the relatively small in-plane signal from much larger out-of-plane signal. In the case of a larger disk we show for the first time how the measured local hysteresis loop shape highly varies with the position of the laser spot on the structure and how this can be exploited in order to measure a circulation probability in the nucleated magnetic vortex. The most exciting measurement in the experimental part extends the previous study of a magnetic vortex by acquiring a total of 882 spatially separated hysteresis loops within a single disk. The results show how evolution of the magnetization vector field in the external magnetic field proceeds through an existence of the magnetization state originally thought to be only the artifact of the micromagnetic simulations.

The last system we have analyzed was the metastable form of iron on the copper substrate. By the combination of SEM imaging and the coercive field mapping technique we have analyzed the areas transformed from the nonmagnetic fcc to the magnetic bcc phase by the focused ion beam. The results we have found shed more light on the crystallization processes potentially used in the magnetic direct writing.

To summarize, we showed the functionality of the developed device by studying the known magnetization processes, as well as the samples with behavior that had not been resolved yet. In future we plan to implement the pump-probe technique to capture time-resolved behavior of the magnetization vector and to use it to characterize the FIB prepared magnetic meta-materials with functional properties. Additionally we are working on the solution leading to the possibility to measure all components of the magnetization in one single step, thus opening new possibilities in the sample characterization.

BIBLIOGRAPHY

- [1] COEY, J. M. D.: *Magnetism and Magnetic Materials*. Cambridge University Press, **2010**. ISBN 9781139486927.
- [2] BLUNDEL, S.: *Magnetism in Condensed Matter*. Oxford University Press, **2001**. ISBN 0198505914.
- [3] STÖHR, J., SIEGMANN, H. C.: *Magnetism: From fundamentals to nanoscale dynamics*, vol. 152. Springer Berlin Heidelberg, **2006**. ISBN 9783540302834.
- [4] FARADAY, M.: *Faraday's Diary of Experimental Investigation - 2nd edition*, vol. 4. HR Direct, **2008**. ISBN 9780981908335.
- [5] ZVEZDIN, A., KOTOV, V.: *Modern Magneto-optics and magneto-optical materials*. CRC Press, **1997**. ISBN 9781420050844.
- [6] KERR, J.: XLIII. on rotation of the plane of polarization by reflection from the pole of a magnet. *Philosophical Magazine Series 5 3*, **1877**, vol. 19, p. 321–343.
- [7] KERR, J.: XXIV. on reflection of polarized light from the equatorial surface of a magnet. *Philosophical Magazine Series 5 5*, **1878**, vol. 30, p. 161–177.
- [8] HALL, E.: XVIII. on the *rotational coefficient* in nickel and cobalt. *Philosophical Magazine Series 5 12*, **1881**. vol. 74, p. 157–172.
- [9] SISSINGH, R.: XXXIV. on Kerr's magneto-optic phenomenon in the case of equatorial magnetization of iron. *Philosophical Magazine Series 5 31*, **1891**, vol. 191, p. 293–317.
- [10] HUBERT, A., SCHÄFER, R.: *Magnetic Domains: The Analysis of Magnetic Microstructures*. Springer Science & Business Media, **1998**. ISBN 9783540641087.
- [11] FERRÉ, J.: Linear and non-linear magneto-optical effects: Magnetism of thin film structures. In *Magnetism and Synchrotron Radiation*, BEAUREPAIRE, E., KAPPLER, J., KRILL, G., SCHEURER, F., Eds., vol. 565 of *Lecture Notes in Physics*. Springer Berlin Heidelberg, **2001**, p. 316–335. ISBN 9783642044984.
- [12] BLAND, J. A. C.: Magneto-optic kerr effect studies of ultrathin magnetic structures. In *Polarized Electron/Polarized Photon Physics*, KLEINPOPPEN, H., NEWELL, W., Eds., Physics of Atoms and Molecules. Springer US, **1995**, p. 269–294. ISBN 9781489914187

- [13] HIEBERT, W. K.; STANKIEWICZ, A.; FREEMAN, M. R.: Direct Observation of Magnetic Relaxation in a Small Permalloy Disk by Time-Resolved Scanning Kerr Microscopy. *Phys. Rev. Lett.*, **1997**, vol. 79.
- [14] ACREMANN, Y., BACK, C. H., BUESS, M., PORTMANN, O., VATERLAUS, A., PESCIA, D., MELCHIOR, H.: Imaging precessional motion of the magnetization vector. *Science*, **2000**, vol. 290. p. 492–495.
- [15] KOOPMANS, B., VAN KAMPEN, M., KOHLHEPP, J. T., DE JONGE, W. J. M.: Ultrafast magneto-optics in nickel: magnetism or optics?. *Phys. Rev. Lett.*, **2000**, vol. 85, p. 844–847.
- [16] FASSBENDER, J.: Magnetization dynamics investigated by time-resolved Kerr effect magnetometry. In *Spin Dynamics in Confined Magnetic Structures II*. Springer Berlin Heidelberg, **2003**, p. 59-92.
- [17] BARMAN, A., KIMURA, T., OTANI, Y., FUKUMA, Y., AKAHANE, K., MEGURO, S.: Benchtop time-resolved magneto-optical Kerr magnetometer. *Review of Scientific Instruments*, **2008**, vol. 79, p. 1–6.
- [18] LEE, K. D., KIM, J. W., JEONG, J. W., KIM, D. H., SHIN, S. C., HONG, K. H., LEE, Y. S., NAM, C. H., SON, M. H., HWANG, S. W.: Femtosecond pump-probe MOKE microscopy for an ultrafast spin dynamics study. *J. Korean Phys. Soc.*, **2006**, vol. 6, p. 2402–2407.
- [19] RIZO, P. J., PUGZLYS, A., LIU, J., REUTER, D., WIECK, A. D., VAN DER WAL, C. H., VAN LOOSDRECHT, P. H. M.: Compact cryogenic Kerr microscope for time-resolved studies of electron spin transport in microstructures. *The Review of scientific instruments*, **2008**, vol. 79, 123904.
- [20] FERRÉ, J., MEYER, P., NYVLT, M., VIŠŇOVSKÝ, V., RENARD, D.: Magneto-optic depth sensitivity in a simple ultrathin film structure. *J. Magn. Magn. Mater.*, **1997**. vol. 165, p. 92–95.
- [21] CORMIER, M., FERRÉ, J., MOUGIN, A., CROMÍRES, J. P., KLEIN, V.: High resolution polar Kerr magnetometer for nanomagnetism and nanospintronics. *Review of Scientific Instruments*, **2008**, vol. 79, 033706.
- [22] SAVOINI, M., CICCACCI, F., DOÒ, L., FINAZZI, M.: Apparatus for vectorial Kerr confocal microscopy. *Review of Scientific Instruments*, **2011**, vol. 82, 023709.
- [23] LODEWIJKS, K., MACCAFERRI, N. N. N., PAKIZEH, T., DUMAS, R. K., ZUBRITSKAYA, I., AKERMAN, J., VAVASSORI, P., DMITRIEV, A.: Magnetoplasmonic design rules for active magneto-optics. *Nano letters*, **2014**, vol. 14, 7207–14.

- [24] RUDGE, J., XU, H., KOLTHAMMER, J., HONG, Y. K., CHOI, B. C.: Sub-nanosecond time-resolved near-field scanning magneto-optical microscope. *Review of Scientific Instruments*, **2015**, vol. 86, 023703.
- [25] MOOG, E., BADER, S. D.: Smoke signals from ferromagnetic monolayers: Fe/Au(100). *Superlattices and Microstructures*, **1985**, vol. 6, p. 543–552.
- [26] BADER, S. D., MOOG, E., GRÜNBERG, P.: Magnetic hysteresis of epitaxially-deposited iron in the monolayer range: A Kerr effect experiment in surface magnetism. *J. Magn. Magn. Mater.*, **1986**, vol. 53, L295–L298.
- [27] AHARONI, A.: *Introduction to the Theory of Ferromagnetism*. Clarendon Press, **2000**. ISBN 9780198508090.
- [28] QIU, Z. Q., BADER, S. D.: Surface magneto-optic Kerr effect. *Review of Scientific Instruments*, **2000**, vol. 71, 1243.
- [29] KASIRAJ, P., SHELBY, R., BEST, J., HORNE, D.: Magnetic domain imaging with a scanning kerr effect microscope. *IEEE Transactions on Magnetics M*, **1986**, p. 5–7.
- [30] VATERLAUS, A., MAIER, U., RAMSPERGER, U., HENSCH, A., PESCIA, D.: An ultrahigh vacuum scanning Kerr microscope. *Review of Scientific Instruments*, **1997**, vol. 68, 2800.
- [31] EGELKAMP, S., REIMER, L.: Imaging of magnetic domains by the Kerr effect using a scanning optical microscope. *Measurement Science and Technology*, **1999**, p. 79–83.
- [32] PROTOPOPOV, V. V., LEE, S., KWON, Y., CHO, S., KIM, H., CHAE, J.: Scanning heterodyne Kerr-effect microscope for imaging of magnetic tracks. *Review of Scientific Instruments*, **2006**, vol. 77, p. 1–6.
- [33] PING, G., SOMEKH, M., SUDDENDORF, M.: A Fast-Scanning Optical Microscope for Imaging Magnetic Domain Structures. *Scanning*, **1996**, vol. 18, p. 8–12.
- [34] BITTER, F.: On inhomogeneities in the magnetization of ferromagnetic materials. *Physical review*, **1931**, vol. 38, p. 1903.
- [35] BITTER, F.: Experiments on the nature of ferromagnetism. *Physical Review*, **1932**, vol. 41, p. 507.
- [36] RAVE, W., SCHÄFER, R., HUBERT, A.: Quantitative observation of magnetic domains with the magneto-optical Kerr effect. *J. Magn. Magn. Mater.*, **1987**, vol. 65, p. 7–14.

- [37] SCHÄFER, R.: Investigation of Domains and Dynamics of Domain Walls by the Magneto-optical Kerr effect. In *Handbook of magnetism and advanced magnetic materials*, **2007**, vol. 3, p. 2–29.
- [38] BERNAND-MANTEL, A., et al.: Electric-field control of domain wall nucleation and pinning in a metallic ferromagnet. *Applied Physics Letters*, **2013**, vol. 102, p. 122406.
- [39] BAUER, U., EMORI, S., D., BEACH, G. S. D.: Voltage-controlled domain wall traps in ferromagnetic nanowires. *Nature Nanotechnology*, **2013**, vol. 8, p. 411–416.
- [40] HRABEC, A., NAM, N. T., PIZZINI, S., RANNO, L.: Magnetization reversal in composition-controlled Gd_{1-x}Co_x ferrimagnetic films close to compensation composition. *Appl. Phys. Lett.*, **2011**, vol. 99, 052507.
- [41] OSTEN, J., LENZ, K., HENSCHKE, A., LINDER, J., FASSBENDER, J.: Simultaneous measurement of anisotropic magnetoresistance and observation of magnetic domains by Kerr microscopy. *Review of Scientific Instruments*, **2014**, vol. 85, 123701.
- [42] CHUMAKOV, D., MCCORD, J., SCHÄFER, R., SCHULTZ, L., VINZELBERG, H., KALTOFEN, R., MÖNCH, I.: Nanosecond time-scale switching of permalloy thin film elements studied by wide-field time-resolved Kerr microscopy. *Phys. Rev. B*, **2005**, vol. 71, 014410.
- [43] FLOHRER, S., SCHÄFER, R., MCCORD, J., ROTH, S., SCHULTZ, L., HERZER, G.: Magnetization loss and domain refinement in nanocrystalline tape wound cores. *Acta Materialia*, **2006**, vol. 51, p. 3253–3259.
- [44] THIDÉ, B.: *Electromagnetic Field Theory second edition*. **2012**. ISBN 978048647732.
- [45] NAYFEH, M. H.: *Electricity and magnetism*. Courier Dover Publications, **1985**. ISBN 9780486789712.
- [46] GRIFFITHS, D. J.: *Introduction to Electrodynamics*. Pearson Education, **2014**. ISBN 9780321972101. 1999.
- [47] JACKSON, J. D.: *Classical electrodynamics*. Wiley, **1999**. ISBN 9780471309321.
- [48] NÝVLT, M.: *Optical interactions in ultrathin magnetic film structures*. [Doctoral Thesis], Prague: Institute of Physics, Faculty of mathematics and Physics, Charles University **1996**.
- [49] FOWLES, G. R.: *Introduction to Modern Optics*. Courier Corporation, **1989**. ISBN 9780486134925.

- [50] FUJIWARA, H.: *Spectroscopic Ellipsometry Principles and Applications*. John Wiley & Sons, Ltd, **2007**. ISBN 9780470060186.
- [51] JONES, R. C.: A new calculus for the treatment of optical systems i. description and discussion of the calculus. *Journal of the Optical Society of America*, **1941**, vol. 31, p. 488–493.
- [52] HECHT, E.: *Optics (4th Edition)*. Addison-Wesley, **2002**. ISBN 9780133977226.
- [53] MCMASTER, W. H.: Polarization and the Stokes Parameters. *American Journal of Physics*, **1954**, vol. 22, p. 351.
- [54] MCMASTER, W. H.: Matrix representation of polarization. *Reviews of Modern Physics*, **1961**, vol. 33, p. 8–28.
- [55] VIŠŇOVSKÝ, V.: *Optics of magnetic multilayers*. CRC Press, **2006**. ISBN 9781420019193.
- [56] ONSANGER, L.: Reciprocal relations in irreversible processes. *Phys. Rev.*, **1931**, vol. 31.
- [57] HAMRLE, J.: *Magneto-optical determination of the in-depth magnetization profile in magnetic multilayers*. [Doctoral Thesis], Prague: Institute of Physics, Faculty of mathematics and Physics, Charles University **2003**.
- [58] HUNT, R. P.: Magneto-optic scattering from thin solid films. *J. Appl. Phys.*, **1967**, vol. 38, p. 1652–1671.
- [59] ZAK, J., MOOG, E. R., LIU, C., BADER, S. D.: Fundamental magneto-optics. *J. Appl. Phys.*, **1990**, vol. 68, 4203.
- [60] ZAK, J., MOOG, E., LIU, C., BADER, S. D.: Universal approach to magneto-optics. *J. Magn. Magn. Mater.*, **1990**, vol. 89, p. 107–123.
- [61] ZAK, J., MOOG, E. R., LIU, C., BADER, S. D.: Elementary formula for the magneto-optic Kerr effect from model superlattices. *Appl. Phys. Lett.*, **1991**, vol. 58, p. 1214–1216.
- [62] ZAK, J., MOOG, E. R., LIU, C., BADER, S. D.: Magneto-optics of multilayers with arbitrary magnetization directions. *Phys. Rev. B*, **1991**, vol. 43, p. 6423–6429.
- [63] VIŠŇOVSKÝ, Š.: Magneto-optical ellipsometry. *Czechoslovak Journal of Physics B*, **1986**, vol. 36, p. 625–650.
- [64] VIŠŇOVSKÝ, Š., et al.: Magneto-optic ellipsometry in multilayers at arbitrary magnetization. *Optics express*, **2001**, vol. 3, p. 121–135.

- [65] VIŠŇOVSKÝ, Š., et al.: Polar and longitudinal magneto-optical Kerr effects in magnetic film/spacer/magnetic substrate system. *Czechoslovak Journal of Physics B*, **2001**, vol. 11, p. 1215–1228.
- [66] YOU, CH. Y., SHIN, S. C. et al.: Derivation of simplified analytic formulae for magneto-optical Kerr effects. *Applied physics letters*, **1996**, vol. 69, p. 1315–1317.
- [67] YEH, P.: Derivation of simplified analytic formulae for magneto-optical Kerr effects. *Surface Science*, **1980**, p. 41–53.
- [68] MANSURIPUR, M.: *The physical principles of magneto-optical recording*. Springer Cambridge University Press, **1995**. ISBN 0521634180.
- [69] BENNETT, H. S.: Faraday effect in solids. *Physical Review*, **1965**, vol. 69.
- [70] LANDAU, L. D.: *Electrodynamics of Continuous Media*. Elsevier, **1984**. ISBN 0750626348.
- [71] SCHOLLWOCK, U., RICHTER, J., FARNELL, D.: *Quantum magnetics*. Lecture Notes in Physics, **2004**.
- [72] ASHCROFT, N. W.: *Solid state physics*. Brooks Cole, **1976**. ISBN 0030839939.
- [73] OSGOOD III, R. M.: Second-order magneto-optic effects in anisotropic thin films. *Journal of magnetism and magnetic materials*, **1998**, vol. 182(3), p. 297–323.
- [74] SEPULVEDA, B., et al.: Linear and quadratic magneto-optical Kerr effects in continuous and granular ultrathin monocrystalline Fe films. *Physical Review B*, **2003**, vol. 68(6), p. 1–11.
- [75] VOIGT, W.: *Magneto-Und Elektrooptik*. BG Teubner, **1908**.
- [76] BADER, S. D.: Smoke. *Journal of magnetism and magnetic materials*, **1991**, vol. 100(1), p. 440–454.
- [77] VIŠŇOVSKÝ, Š.: Matrix representations for vector differential operators in general orthogonal coordinates. *Czechoslovak journal of physics*, **2004**, vol. 8, p. 793–819.
- [78] ELMORE, W.: The magnetic structure of Cobalt. *Physical Review*, **1938**, vol. 53, p. 757.
- [79] WILLIAMS, H., BOZORTH, R., and Shockley, W.: Magnetic domain patterns on single crystals of silicon iron. *Physical Review*, **1949**, vol. 1, p. 155.
- [80] FLORCZAK, J. M., and DAHLBERG, E. D.: Detecting two magnetization components by the magneto-optical Kerr effect. *Journal of Applied Physics*, **1990**, vol. 67, p. 7520–7525.

- [81] OSSGOOD, R. M., WHITE, R. L., and CLEMENS, B. M.: Asymmetric magneto-optic response in epitaxial Fe(110)/Mo(110) thin films. *IEEE Transactions on Magnetics*, **1995**, vol. 6, p. 3331–3333.
- [82] BERGER, A., and PUFALL, M. R.: Generalized magneto-optical ellipsometry. *Applied Physics Letters*, **1997**, vol. 7, p. 965.
- [83] BERGER, A., and PUFALL, M. R.: Quantitative vector magnetometry using generalized magneto-optical ellipsometry. *Journal of Applied Physics*, **1999**, vol. 7, p. 4583.
- [84] KABOS, P., KOS, A., and SILVA, T.: Vectorial second-harmonic magneto-optic Kerr effect measurements. *Journal of Applied Physics*, **2000**, vol. 9, p. 2–5.
- [85] VAVASSORI, P.: Polarization modulation technique for magneto-optical quantitative vector magnetometry. *Applied Physics Letters*, **2000**, vol. 11, p. 1605.
- [86] DING, H., PÜTTER, S., OEPEN, H., and KIRSCHNER, J.: Experimental method for separating longitudinal and polar Kerr signals. *Journal of magnetism and magnetic materials*, **2000**, vol. 212, p. 5–11.
- [87] DING, H., PÜTTER, S., OEPEN, H., and KIRSCHNER, J.: Spin-reorientation transition in thin films studied by the component-resolved Kerr effect. *Physical Review B*, **2001**, vol. 13, p. 134425.
- [88] OHLDAQ, H., WEBER, N. B., HILLEBRECHT, F. U., and KISKER, E.: Observation of in plane magnetization reversal using polarization dependent magneto-optic Kerr effect. *Journal of Applied Physics*, **2002**, vol. 4, p. 2228.
- [89] LEE, J. W., et al.: Full vectorial spin-reorientation transition and magnetization reversal study in ultrathin ferromagnetic films using magneto-optical Kerr effects. *Physical Review B*, **2002**, vol. 14, p. 144437.
- [90] MORALES, L., et al.: Magnetization reversal measurements in mesoscopic amorphous magnets by magneto-optical Kerr effect. *European Physical Journal B*, **2004**, vol. 40, p. 463–470.
- [91] COWBURN, R. P., et al.: A new technique for measuring magnetic anisotropies in thin and ultrathin films by magneto-optics. *Journal of Applied Physics*, **1997**, vol. 81, p. 6879.
- [92] JIMÉNEZ, E., et al.: Vectorial Kerr magnetometer for simultaneous and quantitative measurements of the in-plane magnetization components. *The Review of scientific instruments*, **2014**, vol. 5, p. 053904.

- [93] DABOO, C., et al.: Vectorial magnetometry with the magneto-optic Kerr effect applied to Co/Cu/Co trilayer structures. *Physical Review B*, **1993**, vol. 18, p. 11852–11859.
- [94] FLAJSŤMAN, L.: *Konstrukce zařizení pro měření magneto-optických vlastností mikro a nanostruktur*. [Bachelor's thesis], Brno: Brno: University of Technology, Faculty of mechanical engineering, Institute of physical engineering, **2013**.
- [95] UHLÍŘ, V.: *Studium tenkých vrstev a povrchů pomocí magneto-optických jevů*. [Master's thesis], Brno: University of Technology, Faculty of mechanical engineering, Institute of physical engineering, **2006**.
- [96] INC., T. That1510 product datasheet, 2015.
- [97] POLISETTY, S., et al.: Optimization of magneto-optical Kerr setup: analyzing experimental assemblies using Jones matrix formalism. *The Review of scientific instruments*, **2008**, vol. 5, p. 55107.
- [98] BERTOTTI, G., MAYERGOYZ, I., and SERPICO, C.: *Non Linear Magnetization Dynamics in Nanosystems*. Elsevier, **2009**.
- [99] MAGNES, J., et al.: Quantitative and qualitative study of gaussian beam visualization techniques. *arXiv preprint physics*, **2006**.
- [100] SHINJO, T.: *Nanomagnetism and spintronics*. Elsevier, **2013**. ISBN 0444632794.
- [101] GUIMARÃES, A. A.: *Principles of nanomagnetism*. Springer Science & Business Media, **2009**.
- [102] STONER, E. C., and WOHLFARTH, E. P.: A Mechanism of Magnetic Hysteresis in Heterogeneous Alloys. *Philosophical Transactions of the Royal Society of London A: Mathematical, Physical and Engineering Sciences*, **1948**, vol. 826, p. 599–642.
- [103] SKOMSKI, R.: *Simple models of magnetism*. Oxford: Oxford University Press, **2008**. ISBN 0199655391.
- [104] LI, J., et al.: Design of a vector magnet for the measurements of anisotropic magnetoresistance and rotational magneto-optic Kerr effect. *The Review of scientific instruments*, **2012**, vol. 3, p. 33906.
- [105] BALLENTINE, G. E.: *Comparison of Time-Resolved Micromagnetic Dynamics Experiments on Ni80Fe20 and Landau-Lifshitz-Gilbert Micromagnetic Simulation*. [Doctoral Thesis], Alberta: Department of physics, University of Alberta **2002**.

- [106] WESTPHALEN, A., et al.: Invited article: Vector and Bragg Magneto-optical Kerr effect for the analysis of nanostructured magnetic arrays. *The Review of scientific instruments*, **2007**, vol. 12, p. 121301.
- [107] RAVE, W., HUBERT, A.: Magnetic ground state of a thin-film element. *IEEE Transactions on Magnetics*, **2000**, vol. 6, p. 3886–3899.
- [108] CHIEN, C. L., HUBERT, A.: Patterned nanomagnets. *Physics Today*, **2007**, vol. 6, p. 40–45.
- [109] BOHLENS, S., et al.: Current controlled random-access memory based on magnetic vortex handedness. *Applied Physics Letters*, **2008**, vol. 14, p. 142508.
- [110] KUMAR, D., BARMAN, S., and BARMAN, A.: Magnetic vortex based transistor operations. *Scientific reports*, **2014**, vol. 4, p. 4108.
- [111] KIM, D. H., et al.: Biofunctionalized magnetic-vortex microdiscs for targeted cancer-cell destruction. *Nature materials*, **2010**, vol. 2, p. 165–171.
- [112] GUSLIENKO, K. Y.: Magnetic vortex state stability, reversal and dynamics in restricted geometries. *Journal of nanoscience and nanotechnology*, **2008**, vol. 6, p. 2745–2760.
- [113] DONAHUE, M., AND PORTER, D. Oommf user’s guide, version 1.0. *Interagency Report NISTIR 6376*.
- [114] STAŇO, M.: *Characterization of magnetic nanostructures by magnetic force microscopy*. [Master’s thesis], Brno: University of Technology, Faculty of mechanical engineering, Institute of physical engineering, **2012**.
- [115] TURČAN, I.: *Variable field magnetic force microscopy*. [Bachelor’s thesis], Brno: University of Technology, Faculty of mechanical engineering, Institute of physical engineering, **2015**.
- [116] VAŇATKA, M.: *Spin vortex states in magnetostatically coupled magnetic nanodisks*. [Master’s thesis], Brno: University of Technology, Faculty of mechanical engineering, Institute of physical engineering, **2015**.
- [117] UHLÍŘ, V.: Dynamic switching of the spin circulation in tapered magnetic nanodisks. *Nature nanotechnology*, **2013**, vol. 5, p. 341–346.
- [118] URBÁNEK, M.: Dynamics and efficiency of magnetic vortex circulation reversal. *Nature nanotechnology*, **2013**, issue. 9, p. 094415.
- [119] USOV, N., and PESCHANY, S.: Magnetization curling in a fine cylindrical particle. *Journal of Magnetism and Magnetic Materials*, **1993**, issue. 3, p. L290–L294.

- [120] GUSLIENKO, K. Y., and METLOV, K. L.: Evolution and stability of a magnetic vortex in small cylindrical ferromagnetic particle under applied field. *Physical Review B*, **2001**, vol. 63, p. 100403.
- [121] GUSLIENKO, K. Y. et al.: Field evolution of magnetic vortex state in ferromagnetic disk. *Applied Physics Letters*, **2001**, vol. 24, p. 3848–3850.
- [122] GUSLIENKO, K. Y. et al.: Magnetization reversal due to vortex nucleation, displacement, and annihilation in submicron ferromagnetic dot arrays. *Physical Review B*, **2001**, vol. 2, p. 1–10.
- [123] BALAJKA, J.: *Switching vortex chirality in magnetostatically coupled Permalloy nanodisks*. [Master's thesis], Brno: University of Technology, Faculty of mechanical engineering, Institute of physical engineering, **2012**.
- [124] WU, K. M., et al.: Influence of asymmetry on vortex nucleation and annihilation in submicroscaled permalloy disk array. *Applied Physics Letters*, **2008**, vol. 26, p. 2–4.
- [125] RAHM, M., et al.: Vortex nucleation in submicrometer ferromagnetic disks. *Applied Physics Letters*, **2003**, vol. 23, p. 4110–4112.
- [126] HENGSTMANN, T. M., et al.: Stray-field investigation on permalloy nanodisks. *Journal of Applied Physics*, **2001**, vol. 12, p. 6542–6544.
- [127] KITTEL, C.: Physical theory of ferromagnetic domains. *Reviews of Modern Physics*, **1949**, p. 51.
- [128] SUKHOSTAVETS, O. V., et al.: Probing the anharmonicity of the potential well for a magnetic vortex core in a nanodot. *Physical Review Letters*, **2013**, vol. 24, p. 1–5.
- [129] NOVOSAD, V., et al.: Magnetic vortex resonance in patterned ferromagnetic dots. *Physical Review B - Condensed Matter and Materials Physics*, **2005**, vol. 2, p. 1–5.
- [130] HERTEL, R.: Magnetic nanostructures: vortex states à la carte. *Nature nanotechnology*, **2013**, vol. 5, p. 318–320.
- [131] ZHU, F. Q., et al.: Magnetic bistability and controllable reversal of asymmetric ferromagnetic nanorings. *Physical Review Letters*, **2006**, vol. 2, p. 1–4.
- [132] KIMURA, T., et al.: Vortex motion in chirality-controlled pair of magnetic disks. *Physical Review Letters*, **2007**, vol. 13, p. 2–4.
- [133] GLOSS, J., et al.: Ion-beam-induced magnetic and structural phase transformation of Ni-stabilized face-centered-cubic Fe films on Cu(100). *Applied Physics Letters*, **2013**, vol. 26, p. 262405.

-
- [134] GLOSS, J.: *Magnetic transformation of metastable fcc Fe/Cu(100) films by focused ion beam*. [Master's thesis], Brno: University of Technology, Faculty of mechanical engineering, Institute of physical engineering, **2014**.
- [135] ESCHENFELDER, A.: *Magnetic bubble technology*. Berlin: Springer-Verlag, **1982**.
- [136] MALOZEMOFF, A. P., and SLONCZEWSKI, J. C.: *Magnetic Domain Walls in Bubble Materials*. Academic press., **1979**.
- [137] VANSTEENKISTE, A., WIELE, B.: MuMax: a new high-performance micro-magnetic simulation tool. *Journal of Magnetism and Magnetic Materials*, **2011**, vol. 323, p. 2585-2591.
- [138] KRONMÜLLER, H.: *Handbook of Magnetism and Advanced Magnetic Materials*. Wiley Online Library., **2007**. ISBN 0470022175.
- [139] CUI, X., HU, S., and KIMURA, T.: Detection of a vortex nucleation position in a circular ferromagnet using asymmetrically configured electrodes. *Applied Physics Letters*, **2014**, vol. 105, p. 82403.

LIST OF ABBREVIATIONS

VSM	vibrating sample magnetometry
SQUID	super-conductive quantum interference device
MOKE	magneto-optical Kerr effect
SKEM	scanning Kerr effect magnetometer
OOP	out-of-plane
IP	in-plane
RCP	right handed circular polarization
LCP	left handed circular polarization
MO	magneto-optical
QWP	quarter-wave-plate
HWP	half-wave-plate
LUT	look up table
FFT	fast fourier transform
Py	Permalloy
AMR	anisotropic magneto resistance
RVM	rigid vortex model
OOMMF	Object Oriented Micromagnetic Framework
fcc	face-centered cubic
bcc	body-centered cubic
MFM	magnetic force microscopy
YIG	Yttrium iron garnet
CFM	coercive field mapping mode

APPENDIX

Appendix A - Permittivity tensor $\overleftrightarrow{\epsilon}_r$

$$\epsilon_{xx} = \frac{\frac{nq^2}{m} \left(L^2 - \left(\frac{\omega q}{m} \right)^2 B_x^2 \right)}{\epsilon_0 D_0} + 1 \quad (\text{A.1})$$

$$\epsilon_{xy} = \frac{\frac{nq^2}{m} \left(- \left(\frac{\omega q}{m} \right)^2 B_x B_y - \left(\frac{\omega q}{m} \right) i L B_z \right)}{\epsilon_0 D_0} \quad (\text{A.2})$$

$$\epsilon_{xz} = \frac{\frac{nq^2}{m} \left(- \left(\frac{\omega q}{m} \right)^2 B_x B_z + \left(\frac{\omega q}{m} \right) i L B_y \right)}{\epsilon_0 D_0} \quad (\text{A.3})$$

$$\epsilon_{yx} = \frac{\frac{nq^2}{m} \left(- \left(\frac{\omega q}{m} \right)^2 B_x B_y + \left(\frac{\omega q}{m} \right) i L B_z \right)}{\epsilon_0 D_0} \quad (\text{A.4})$$

$$\epsilon_{yy} = \frac{\frac{nq^2}{m} \left(L^2 - \left(\frac{\omega q}{m} \right)^2 B_y^2 \right)}{\epsilon_0 D_0} + 1 \quad (\text{A.5})$$

$$\epsilon_{yz} = \frac{\frac{nq^2}{m} \left(- \left(\frac{\omega q}{m} \right)^2 B_y B_z - \left(\frac{\omega q}{m} \right) i L B_x \right)}{\epsilon_0 D_0} \quad (\text{A.6})$$

$$\epsilon_{zx} = \frac{\frac{nq^2}{m} \left(- \left(\frac{\omega q}{m} \right)^2 B_x B_z - \left(\frac{\omega q}{m} \right) i L B_y \right)}{\epsilon_0 D_0} \quad (\text{A.7})$$

$$\epsilon_{zy} = \frac{\frac{nq^2}{m} \left(- \left(\frac{\omega q}{m} \right)^2 B_y B_z + \left(\frac{\omega q}{m} \right) i L B_x \right)}{\epsilon_0 D_0} \quad (\text{A.8})$$

$$\epsilon_{zz} = \frac{\frac{nq^2}{m} \left(L^2 - \left(\frac{\omega q}{m} \right)^2 B_z^2 \right)}{\epsilon_0 D_0} + 1 \quad (\text{A.9})$$

$$(\text{A.10})$$

Appendix B - On the Rotation and the Ellipticity

This section serves only to phenomenologically present the reader with some basic concepts giving a rise to the magneto-optical observables. It has been discovered very early, that magneto-optical effects can be expressed as a phase and amplitude difference of two circular polarizations. Kerr rotation θ describing the rotation of the ellipse (Fig. 2.5 (d)) is given by the difference in the index of refraction for the right handed (RCP) and left handed (LCP) circularly polarized wave, while the Kerr ellipticity ϵ is described solely by changes in the amplitudes of the RCP and LCP waves.

It follows directly from the Lorentz force that electron in a matter will, in presence of a circularly polarized wave, follow the sense of rotation given by the wave itself [? 55]. In some special cases the left hand circular path is not equivalent to the right hand circular path. We show in a very simple way, that rotation of the ellipse is caused by the difference of indices of refraction. We will start with the description of the two circularly polarized waves(RCP, LCP) propagating in the z direction in the Cartesian basis

$$\begin{aligned} E_x^+ &= E \cos\left(\frac{\omega}{c}(n^+z - ct)\right), & E_x^- &= E \cos\left(\frac{\omega}{c}(n^-z - ct)\right) \\ E_y^+ &= -E \sin\left(\frac{\omega}{c}(n^+z - ct)\right), & E_y^- &= E \sin\left(\frac{\omega}{c}(n^-z - ct)\right). \end{aligned} \quad (\text{A.11})$$

Lets define the index of refraction as a $n = (n^+ + n^-)/2$ and rewrite the equations Eq. (A.11)

$$\begin{aligned} E_x^+ &= E \cos\left(\frac{\omega}{c}(nz - ct) - \frac{\omega}{2c}(n^+ - n^-)z\right), & E_x^- &= E \cos\left(\frac{\omega}{c}(nz - ct) + \frac{\omega}{2c}(n^+ - n^-)z\right) \\ E_y^+ &= -E \sin\left(\frac{\omega}{c}(nz - ct) - \frac{\omega}{2c}(n^+ - n^-)z\right), & E_y^- &= E \sin\left(\frac{\omega}{c}(nz - ct) + \frac{\omega}{2c}(n^+ - n^-)z\right). \end{aligned} \quad (\text{A.12})$$

Now we can use goniometric identities for the sum and difference of sine and cosine functions. In the following step we sum the x and y components of the two waves and we look for the relative angle between the two orthogonal components. We obtain

$$\tan(\theta) = \frac{E_y}{E_x} = \frac{2E \cos\left[\frac{\omega}{c}(nz - ct)\right] \sin\left[\frac{\omega}{2c}(n^+ - n^-)z\right]}{2E \cos\left[\frac{\omega}{c}(nz - ct)\right] \cos\left[\frac{\omega}{2c}(n^+ - n^-)z\right]} = \tan\left[\frac{\omega}{2c}(n^+ - n^-)z\right]. \quad (\text{A.13})$$

From this we see

$$\theta = \frac{\omega}{2c}(n^+ - n^-)z = \frac{\pi}{\lambda}(n^+ - n^-)z. \quad (\text{A.14})$$

The resulting form shows, that the rotation of the polarization is given solely by the effect of different refractive indices.

In order to see the origin of the ellipticity we define the complex index of refraction as $n = n' + in''$. The imaginary part of the complex index of refraction stands for the losses of the propagating electromagnetic wave [46, 49? ?]. Letd write the wave traveling in the isotropic absorbing medium in the z direction. For the convenience we will use the complex notation following the Eq. (2.1)

$$E_x = E e^{-i\frac{\omega}{c}(ct - nz)} = E e^{-i\frac{\omega}{c}(ct - (n' + in'')z)} = E e^{-i\frac{\omega}{c}(ct - n'z)} e^{-\frac{\omega}{c}(n''z)}. \quad (\text{A.15})$$

It is apparent, that the original wave will be attenuated with increasing z . Following this result lets assume the different degree of attenuation for the left and right circularly polarized waves:

$$\begin{aligned} E_x^+ &= E \cos\left(\frac{\omega}{c}(nz - ct)\right) e^{-\frac{\omega}{c}(n''_1 z)}, & E_x^- &= E \cos\left(\frac{\omega}{c}(nz - ct)\right) e^{-\frac{\omega}{c}(n''_2 z)} \\ E_y^+ &= -E \sin\left(\frac{\omega}{c}(nz - ct)\right) e^{-\frac{\omega}{c}(n''_1 z)}, & E_y^- &= E \sin\left(\frac{\omega}{c}(nz - ct)\right) e^{-\frac{\omega}{c}(n''_2 z)}. \end{aligned} \quad (\text{A.16})$$

Combining the x and y components gives

$$\begin{aligned} E_x &= E(e^{-\frac{\omega}{c}(n_1''z)} + e^{-\frac{\omega}{c}(n_2''z)}) \cos\left(\frac{\omega}{c}(nz - ct)\right) \\ E_y &= E(e^{-\frac{\omega}{c}(n_2''z)} - e^{-\frac{\omega}{c}(n_1''z)}) \sin\left(\frac{\omega}{c}(nz - ct)\right), \end{aligned} \quad (\text{A.17})$$

yielding the expression for the ellipse. As was already pointed out, magneto-optic observables are very small so let's suppose that also the effect inducing them is very small. We express n_2'' in terms of n_1'' with small perturbation $\Delta n''$. Then we can express the exponential including the $n_1'' + \Delta n''$ in the second order Maclaurin series. Then the elliptical polarization is given by

$$\begin{aligned} E_x &= Ee^{-\frac{\omega}{c}(n_1''z)}(2 - \Delta n'') \cos\left(\frac{\omega}{c}(nz - ct)\right) \\ E_y &= Ee^{-\frac{\omega}{c}(n_1''z)}(\Delta n'') \sin\left(\frac{\omega}{c}(nz - ct)\right). \end{aligned} \quad (\text{A.18})$$

Dividing the E_x component by the E_y component will result in (Confer Eq. (2.5) and (2.6) for $\delta_{x,y} = \pi/2$)

$$\tan(\Theta) = \frac{E_y}{E_x} = \sin(\epsilon) \approx \epsilon = \frac{\Delta n''}{2 - \Delta n''} \approx \frac{\Delta n''}{2}. \quad (\text{A.19})$$

This result attributes the ellipticity to the difference in the absorption coefficients of the LCP and RCP waves.

Magneto-optical treatment in general deals with combination of the two described effects. The resulting ellipse will have non-zero ellipticity as well as rotation.

So in summary, this section, despite the lack of rigorousness, has given us some insight how both magneto-optical observables (θ and ϵ) are induced.

Appendix C - Heating induced nucleation

Measured hysteresis loops for a 20 nm layer of Permalloy for various incident power of the laser are given in Fig. B.1

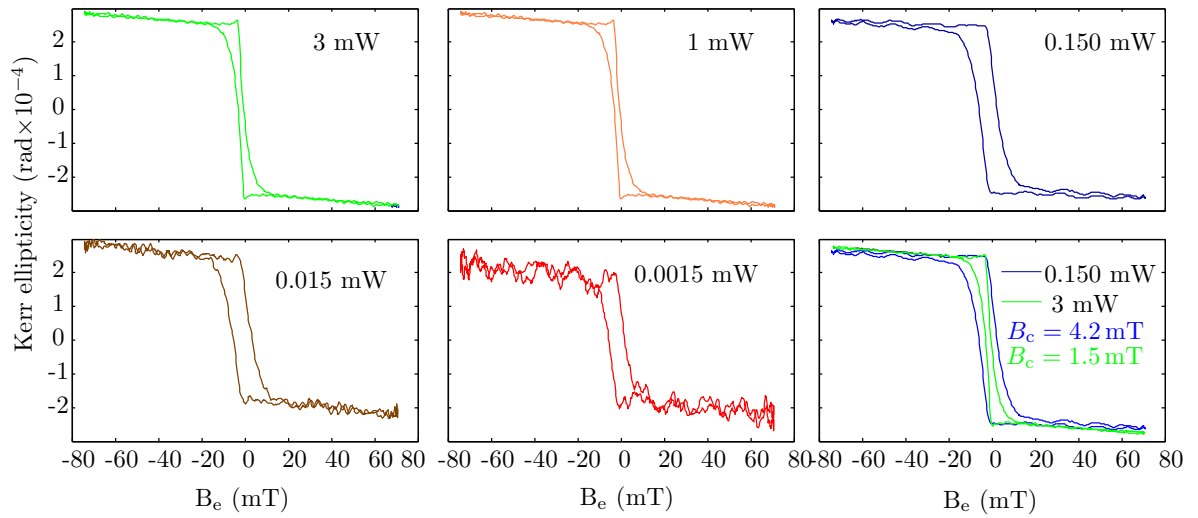


Fig. B.1: Hysteresis loop measurements showing an effect of a heating on the coercive field of the Permalloy layer. Individual loops are averaged from 20 measurements.